NASA CONTRACTOR REPORT

NASA CR-1603

DEVELOPMENT OF A GAS SAMPLING SYSTEM

by J. E. Hueser and F. J. Brock

Prepared by
NORTON RESEARCH CORPORATION
Cambridge, Mass. 02142
for Langley Research Center

NATIONAL AERONAUTICS AND SPACE ADMINISTRATION • WASHINGTON, D. C. • JULY 1970

NASA CR-1603

DEVELOPMENT OF A GAS SAMPLING SYSTEM

By J. E. Hueser and F. J. Brock

Prepared under Contract No. NAS 1-5347-15 by
NORTON RESEARCH CORPORATION
Cambridge, Mass. 02142

for Langley Research Center

NATIONAL AERONAUTICS AND SPACE ADMINISTRATION

TABLE OF CONTENTS

LIST OF FIGURES

DEVELOPMENT OF A GAS SAMPLING SYSTEM

By J. E. Hueser & F. J. Brock
Norton Research Corporation

SUMMARY

The results of a theoretical analysis and a computed performance evaluation of a gas sampling system for use aboard a high speed entrycraft are presented. The system furnishes a sample of the atmosphere as a molecular beam, consisting of both an unscattered and a scattered gas component, to the instrument region of the probe. The mathematical analysis presented, establishes: 1) the fraction of the flux, incident on the entrance of the gas inlet system, which is transmitted without suffering either a gas-gas or gas-wall collision 2) the ratio of the unscattered to scattered exit flux per unit solid angle (signal-to-noise ratio) 3) the scattered gas density distribution inside the gas inlet tubes 4) the temperature of the gas inlet as a result of the high enthalpy incident flux 5) the functional dependence of each of these parameters on the atmospheric density, entrycraft velocity, and inlet tube dimensions. Data are presented for these parameters to establish the limit of operation (highest atmospheric density) of the sampling system for an analysis of the Martian atmosphere.

These data are used as the basis for designing a gas inlet system, including limiting apertures and pumping ducts, for operation down to approximately 30 km in the Martian atmos-

phere. Design drawings, material requirements, and fabrication techniques are presented for a multiple tube inlet system, with an individual inlet tube "diameter" of 5×10^{-3} cm.

A gas sampling system was also designed and fabricated for operation in the Earth atmosphere. The sampler design was chosen to confirm the theoretical performance predictions that the gas-gas scattering attenuation of the primary transmitted flux represents a limiting parameter and applies over a relatively wide range of density. The dimensions were chosen so that the gas-gas scattering attenuation limitation would occur prior to excessive gas enthalpy heating. Data are presented for the performance evaluation of this sampler together with photographs of the completed sampler.

INTRODUCTION

The conclusion of Task 12, "Feasibility Study of an Atmospheric Analysis Experiment", was that a gas sampling system consisting of a bundle of small diameter tubes had a high probability of obtaining an exact sample of a planetary atmosphere and maintaining it unaltered and uncontaminated until it was analyzed in the instrument region of a high speed entry probe. During that investigation, the concepts and mathematical foundations of the molecular beam sampling system were formed.

The reasoning behind this approach is that if a serious attempt is made at establishing the physical properties of the atmosphere in terms of the properties of the molecular

flux which has passed through the sampling system and is incident on some detector, intermediate scattering events which tend to confuse the interpretation of the detector signal are to be avoided. It is desireable, therefore, to base the analysis of the atmosphere on the measurement of the properties of the flux in the form of a molecular beam which has passed through the sampling system unscattered.

To establish the properties of this molecular beam in terms of the variable parameters of undisturbed gas density, entrycraft velocity and sampler dimensions; theoretical expressions for the following were established: 1) the total flux which enters the sampler 2) the flux which is scattered off the walls of the sampler 3) the diffuse gas density distribution inside the sampler tubes 4) the flux which suffers a gas-gas collision with this internal tube diffuse gas 5) the unscattered flux which passes through the sampler (considering both gas-gas and gas-wall collisions) 6) the sampler temperature based on the scattered flux density 7) the internal tube mean free path based on the diffuse gas density 8) the angular distribution of the scattered and unscattered exit flux and 9) the signal-to-noise ratio per unit solid angle (the ratio of unscattered-to-scattered flux). Those expressions which could not be solved analytically were evaluated numerically by a computer program developed during these investigations.

The purpose of this phase of the investigation was to continue the theoretical analysis, to evaluate the performance of the gas sampling system based on computer produced numerical solutions of the theoretical equations, to investigate suitable

materials and fabrication techniques, and to design a gas sampling system for a deep penetration into the atmosphere of Mars.

At the present time, the experimental evaluation of the sampler under simulated entry conditions of high speed and high density is impractical. Therefore, the testing of the sampler in an actual flight in the Earth atmsophere was reviewed and found feasible. Such a flight provides sampler performance data and confirmation of the theory while obtaining significant scientific information.

THEORETICAL SOLUTION

A. Mathematical Analysis

This section outlines in detail the analytical approach and presents the necessary functional relationships which make up the mathematical model describing the operational characteristics of the gas sampler. These equations, with the appropriate simplifying approximations for this particular application (the deep Martian atmosphere probe), are the basis of a computer program. This program provides the numerical calculations and produces the solution for the relationships between the exit properties of the flux and the properties of the undisturbed atmosphere in front of the probe.

The derived equations, without approximations, are presented first; after which a discussion of the appropriate approximations together with the equations which were used in the numerical calculations is presented.

1. Concept And Inputs From Task 12 Results.- The feasibility of providing an undisturbed sample of the atmosphere utilizing a high speed sampling probe was explored under task 12 and the foundation of the mathematical model used in task 15 was formed at that time. During that investigation, the properties of the unscattered component of the total exit flux were established and it was shown that the attenuation of the primary beam as a result of gas-gas scattering by the diffuse gas internal to the tube, which arises as a result of gas-wall collisions in the primary beam, is a non-negligible quantity in the determination of the transmitted primary flux.

It is necessary to establish the angular distribution of both the primary and the scattered flux before calculating the ratio of the primary to scattered flux (signal-to-noise ratio) in terms of the atmospheric density.

Since the functional relationships between the primary exit flux and the atmosphere appear in the derivation of the scattered exit flux, it is necessary to review them before continuing the derivation of the equations describing the properties of the scattered flux.

1.1 Geometrical transmission function.- Each molecule with its associated velocity vector, once having entered the tube, will travel a certain distance down the tube without colliding with the wall (neglecting gas-gas interactions for the moment). If that distance is greater than the length of the tube, it will leave the tube exit without suffering a wall collision. The probability that a molecule is transmitted down the tube a distance x is a function of the length-to-diameter ratio of the tube and other factors such as the distribution of molecular velocities in the atmosphere and the velocity of the probe with respect to the gas.

The expression which was derived for the flux density incident on the tube entrance from an angle ϕ with the tube axis within $d\phi$, is:

$$\psi_1(S,\phi)d\phi = \frac{n_o v_m}{\sqrt{\pi}} \sin\phi\cos\phi \left\{ (1+S^2\cos^2\phi)e^{-S^2} + \sqrt{\pi}S\cos\phi\left(\frac{3}{2}+S^2\cos^2\phi\right) \right.$$

$$\left. \left[1+\mathrm{erf}(S\cos\phi)\right] e^{-S^2\sin^2\phi} \right\} d\phi \,. \qquad (1.1.1)$$

This expression indicates those properties of atmosphere-probe system which influence the number of molecules per unit area per unit time which enter the sampler tube, namely 1) the atmospheric density n_o 2) the velocity distribution of the gas through v_m, the most probable thermal velocity 3) the angle ϕ and 4) the speed ratio S, which is the ratio of the probe velocity U and v_m.

The fraction of flux incident from ϕ which is transmitted a distance X along the tube axis before colliding with the wall was shown to be:

$$\psi_2(X,\phi) = \frac{2}{\pi}\left\{\cos^{-1}(X\tan\phi) - X\tan\phi\,(1-X^2\tan^2\phi)^{\frac{1}{2}}\right\} \qquad (1.1.2)$$

where X is the dimensionless distance-to-diameter ratio and $X=X_M$ is the tube length-to-diameter ratio.

These two relationships are sufficient to define the geometrical transmission function which is the ratio of the primary flux which is transmitted through the tube (at least as far as X) to the flux which entered:

$$T_g(S,X) = \frac{F_p(S,X)}{F_p(S,O)} \qquad (1.1.3)$$

where
$$F_p(S,X) = \pi r^2 \int_0^{\tan^{-1}X^{-1}} \psi_1(S,\phi)\psi_2(X,\phi)d\phi \qquad (1.1.4)$$

and
$$F_p(S,O) = \pi r^2 \int_0^{\pi/2} \psi_1(S,\phi)\psi_2(X,\phi)d\phi \ . \qquad (1.1.5)$$

The expression for $F_p(S,O)$ can be integrated directly, the result being:

$$F_p(S,O) = \frac{\pi r^2 n_o v_m}{2\sqrt{\pi}} \left\{ e^{-S^2} + \sqrt{\pi} S \left[1 + \mathrm{erf}(S) \right] \right\} \ . \qquad (1.1.6)$$

Evaluating the integral in $T(S,X)$ up to $X = X_M$ gives the geometrical transmission function $T(S,X_M)$.

1.2 Total transmission function.- In the previous section, the transmission function was derived considering only the effects of gas-wall interactions. When gas-gas collisions are also considered the expression for the probability of a particle incident at an angle ϕ with the tube axis travelling a distance X along the tube axis without suffering a gas-gas collision is:

$$\psi_3(X,\phi) = e^{-2r\sigma(1+\tan^2\phi)^{\frac{1}{2}} \int_0^X n(X')dX'} \qquad (1.2.1)$$

where σ is the gas-gas collision cross-section and $n(X)$ is the diffuse gas density distribution inside the tube. The expression for the flux which has survived a distance X along the tube without suffering either a gas or a wall collision now becomes:

$$F_p(S,X) = \pi r^2 \int_0^{\tan^{-1}X^{-1}} \psi_1(S,\phi)\psi_2(X,\phi)\psi_3(X,\phi)d\phi \ . \qquad (1.2.2)$$

As before, the transmission function is defined as:

$$T(S,X) = \frac{F_p(S,X)}{F_p(S,O)} \qquad (1.2.3)$$

but $F_p(S,X)$ is as given in Eq. (1.2.2). This transmission function is defined as the total transmission function and represents that fraction of the flux incident on the tube entrance which is transmitted a distance X without suffering a gas-wall or a gas-gas collision.

1.3 Internal tube diffuse gas density distribution.- As can be seen by examining Eq. (1.2.1), the solution of $\psi_3(X,\phi)$

depends on an integration over the diffuse gas density distribution up to X. It is therefore necessary to establish the functional dependence of n(X) on the system parameters. Since the source of diffuse gas is proportional to the rate at which primary flux is lost due to gas-gas and gas-wall collisions and since the diffuse gas is at rest with respect to probe, the mechanism by which the diffuse gas is dissipated from the tube is through diffusion towards both ends. The diffusion equation which describes the diffuse gas density distribution is:

$$\frac{\pi^2 r^3 \bar{v}}{4} \frac{d^2 n(x)}{dx^2} = \frac{d}{dx} F_p(S,x) \qquad (1.3.1)$$

where $\bar{v}$ is the average thermal velocity of the diffuse gas molecules. Those high velocity gas molecules which collide with the tube or a diffuse gas molecule are assumed to be completely accomodated at the surface and re-emitted as diffuse gas molecules with a temperature characteristic of the tube temperature. Integrating Eq. (1.3.1) twice and inserting the boundary conditions that the diffuse gas density goes to zero at both ends of the tube, gives:

$$n(X) = \frac{8}{\pi^2 r^2 \bar{v}} \left\{ \int_0^X F_p(S,X')dX' - \frac{X}{X_M} \int_0^{X_M} F_p(S,X)dX \right\} . \qquad (1.3.2)$$

The application of the above boundary conditions corresponds to the assertion that the diffuse gas density outside the tube is sufficiently low that back diffusion may be neglected. The validity of this assertion will become more evident when the angular distribution of the scattered flux is presented later.

1.4 Angular distribution of unscattered exit flux.- For a given X_M, the total primary flux transmitted through the tube is contained in the solid angle corresponding to a half angle ϕ_M which is equal to $\tan^{-1} X^{-1}$. To establish the angular distribution of this transmitted flux it is necessary to calculate the value of the incremental flux (dF_p) contained in an element of solid angle ($d\omega$) such as the one represented by the hollow conical volume (cross-hatched annular base) shown in Fig. 1. The angular distribution is then characterized by the values of $dF_p/d\omega$ for half angles ϕ from zero out to ϕ_M. The incremental flux contained in the element of solid angle with a differential half angle $d\phi$ at ϕ can be expressed in terms of the total primary flux transmitted through imaginary tubes with length-to-diameter ratios of X_E and X_E'. In the above illustration, the differential flux is:

$$\Delta F_p = F_p(S,X_E) - F_p(S,X_E') \quad . \qquad (1.4.1)$$

The increment of solid angle is equal to the element of surface area (dS) (the cross-hatched annulus) divided by the radial distance (R) out to the surface element squared.

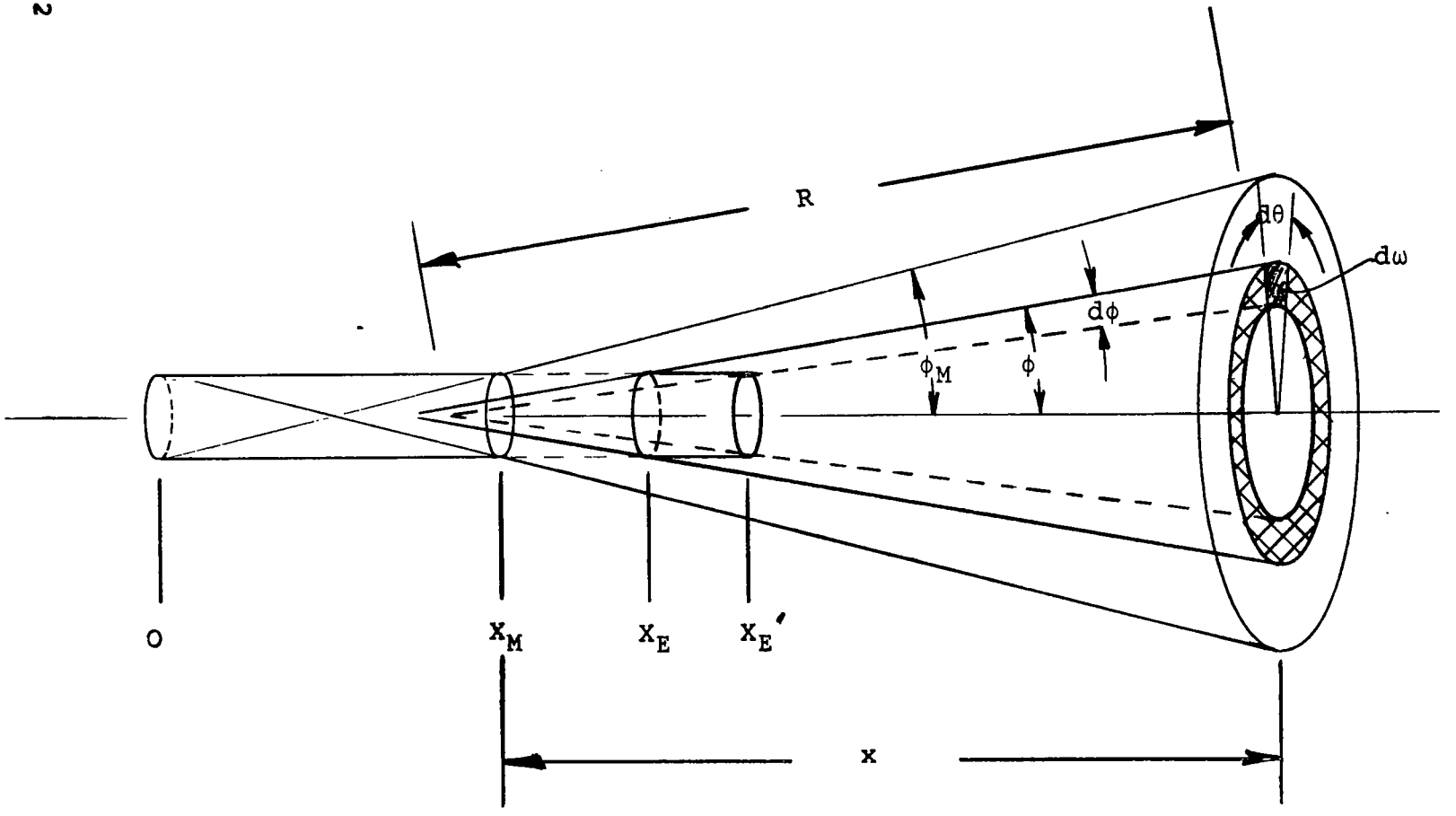

Fig. 1

Diagram representing angular distribution $dF_p/d\omega$.

If x represents the distance from the tube exit to some point where the angular distribution is of concern, say for example the entrance of the ion source, and $x >> L$, the tube exit can be considered a point source (this is a good approximation in the present case since $L \approx .02$ cm and $x \approx 10$ cm). For $X_M \geq 4$, the small angle approximation for $\sin\phi$ can be used and $\sin\phi \approx \tan\phi \approx \phi$ (the maximum error occurrs for $\phi=\phi_M$ and is $\approx 3\%$). Under these conditions we have for the element of solid angle:

$$d\omega = \frac{R\sin\phi d\theta \; Rd\phi}{R^2} = \sin\phi d\phi d\theta \qquad (1.4.2)$$

but since $\sin\phi \approx \phi$

$$d\omega = \phi d\phi d\theta \qquad (1.4.3)$$

$$\Delta\omega = \int_{\phi}^{\phi+d\phi} \phi' d\phi' \int_{0}^{2\pi} d\theta \qquad (1.4.4)$$

$$\Delta\omega = \pi\left\{(\phi+d\phi)^2-\phi^2\right\} . \qquad (1.4.5)$$

The angular distribution of the transmitted flux is then expressed as:

$$\frac{\Delta F_p}{\Delta\omega} = \frac{F_p(S,X_E)-F_p(S,X_E')}{\pi[(\phi+d\phi)^2-\phi^2]} \quad . \tag{1.4.6}$$

In performing the actual numerical calculations, the elemental solid angle increments were made equal. Since

$$\frac{dF_p}{d\phi} = \frac{dF_p}{d\omega}\frac{d\omega}{d\phi} \tag{1.4.7}$$

and since $d\omega/d\phi$ = const.

$$\frac{dF_p}{d\phi} = c\,\frac{dF_p}{d\omega} \quad . \tag{1.4.8}$$

This was done for convenience in interpreting the results; the slopes of plots of F_p vs. ϕ differ only by a numerical constant from $dF_p/d\omega$.

2. Collision Frequency Within The Tube.- Consider now the angular distribution of the scattered exit flux. To specify the angular distribution, the following must be known: 1) the portion of the tube surface from which the flux originates 2) the magnitude of the flux and 3) the direction in which the flux leaves the tube surface. These properties of the flux can

be established by evaluating the molecular incidence rate at all elements of area along the surface of the tube. Considering the following diagram and using a particle conservation argument, the total collision frequency on element of area dS at some point x along the tube within an element of length dx is made up of collisions by particles which have suffered no gas or wall collisions up to x and also collisions by particles which have been scattered from all other elements of surface towards dS.

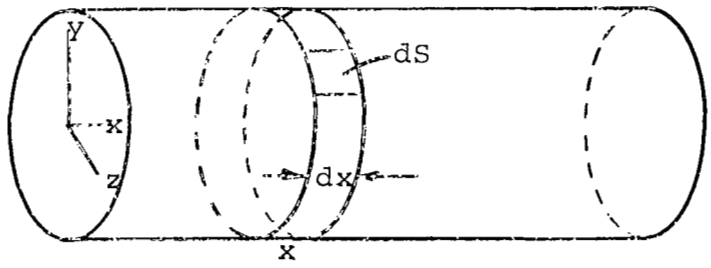

Let ν_p (x) stand for the number of unscattered molecules per unit area per unit time which collide with the tube at x within dx. We define the following expression:

$$\int_0^X \nu_p(X')dX' = \frac{C}{\pi r^2}\left[F_p(S,0) - F_p(S,X)\right] . \qquad (2.1)$$

This equation states that the total number of unscattered molecules which have suffered a gas or wall collision in travelling a distance X down the tube is proportional to the difference

between the flux density entering the tube and that which survived up to X. Differentiating with respect to X gives:

$$\nu_p(X) = -\frac{C}{\pi r^2}\frac{d}{dX}F_p(S,X) \; . \tag{2.2}$$

Using the boundary conditions that $\nu_p(o) = \frac{n\bar{v}}{4}$ and $n(o) = 0$ gives (see Appendix A):

$$\nu_p(X) = -\frac{1}{4\pi r^2}\frac{d}{dX}F_p(S,X) \tag{2.3}$$

or:

$$\nu_p(X) = -\frac{1}{4}\frac{d}{dX}\int_o^{\tan^{-1}X^{-1}} \psi_1(S,\phi)\psi_2(X,\phi)\psi_3(X,\phi)d\phi \; . \tag{2.4}$$

The derivation of $\nu_s(X)$, the collision frequency of scattered molecules incident on X within dX from all other elements of surface X´ within dX´, is quite lengthy and is given in Appendix B; the result is:

$$\nu_s(X) = \int_o^{X_M} \nu_s(X')\psi_5(X,X')dX' \tag{2.5}$$

where:

$$\psi_5(X,X') = \left\{1 - \frac{|X - X'|(|X - X'|^2 + 3/2)}{(|X - X'|^2 + 1)^{3/2}}\right\} \quad . \tag{2.6}$$

Therefore, the total number of molecules per unit area per unit time incident on X within dX is

$$\nu(X) = -\frac{1}{4}\frac{d}{dX}\int_0^{\tan^{-1}X'} \psi_1(S,\phi)\psi_2(X,\phi)\psi_3(X,\phi)d\phi + \int_0^{X_M} \nu_s(X')\psi_5(X,X')dX' \tag{2.7}$$

where:

$$\psi_1(S,\phi) = \frac{n_o v_m}{\sqrt{\pi}}\sin\phi\cos\phi\left\{(1+S^2\cos^2\phi)\Theta^{-S^2} + \sqrt{\pi}S\cos\phi\left[\frac{3}{2} + S^2\cos^2\phi\right]\left[1+\mathrm{erf}(S\cos\phi)\right]\Theta^{-S^2\sin^2\phi}\right\} \tag{2.8}$$

$$\psi_2(X,\phi) = \frac{2}{\pi}\left\{\cos^{-1}(X\tan\phi) - X\tan\phi\left[1-X^2\tan^2\phi\right]^{1/2}\right\} \tag{2.9}$$

$$\psi_3(X,\phi) = e^{-2r\sigma(1+\tan^2\phi)^{1/2}} \int_0^X n(X')dX' . \qquad (2.10)$$

3. Angular Distribution Of Scattered Exit Flux.- Having established the magnitude of the scattered flux per unit area per unit solid angle from an element of area at X within dX, consider now what fraction of this total is emitted in a direction such that it passes through the exit of the tube.

Consider the diagram shown in Fig. 2. The incremental flux scattered from dS into a solid angle $d\omega$ in a direction θ is:

$$dF_s(\omega) = \frac{\nu(z)}{\pi} d\omega dS \cos\phi\sin\theta \qquad (3.1)$$

where, as in Appendix B, $\nu(z)/\pi$ represents the number of molecules per unit area per unit time per unit solid angle leaving dS. The scattered flux leaving the element of area at z within dz into solid angle $d\omega$ in the direction θ is:

$$dF_s(\omega) = \frac{\nu(z)}{\pi} d\omega dz 2\pi r \cos\phi\sin\theta \qquad (3.2)$$

and is represented by the cross-hatched annulus in Fig. 2.

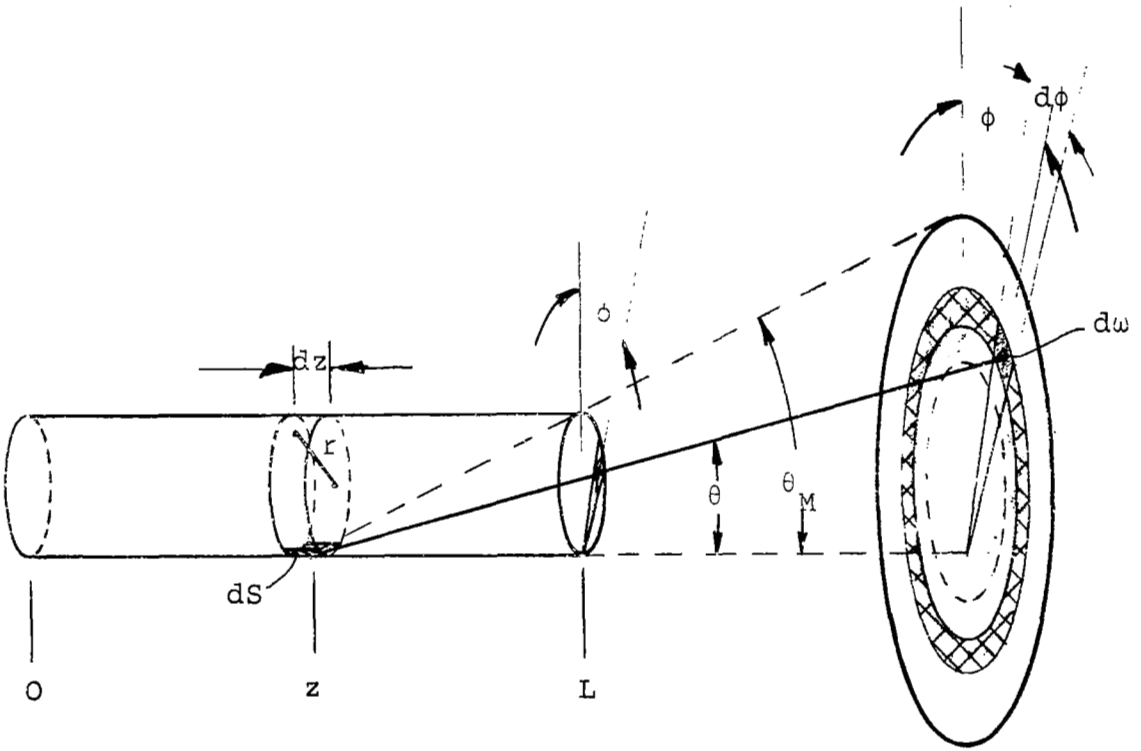

Fig. 2

Diagram representing angular distribution $dF_s/d\omega$.

$$dF_s(\omega) = 2\nu(z)d\omega rdz\ \cos\phi\sin\theta \tag{3.3}$$

$$d\omega = \sin\theta d\theta d\phi \tag{3.4}$$

$$\tan\theta = \frac{2r\ \cos\phi}{L-z}\ . \tag{3.5}$$

The total scattered flux which leaves the element of tube area at z within dz and is emitted through the tube exit in a direction θ within $d\theta$ is:

$$dF_s(z) = 4\int_0^{\cos^{-1}\left\{\left(\frac{L-z}{2r}\right)\tan\theta\right\}} \nu(z)rdz\ \sin^2\theta\ \cos\phi d\phi d\theta \tag{3.6}$$

and is represented by the shaded annulus in Fig. 2.

Now if $X = z/2r$:

$$dF_s(X) = 8r^2\nu(X)\sin^2\theta d\theta dX \int_0^{\cos^{-1}\left\{\left(X_M-X\right)\tan\theta\right\}} \cos\phi d\phi \tag{3.7}$$

or

$$dF_s(X) = 8r^2\nu(X)\ \sin^2\theta d\theta dX\left[1-(X_M-X)^2\tan^2\theta\right]^{1/2}\ . \qquad (3.8)$$

There is a minimum value of X, namely X_m, which can emit in a direction θ such that the molecules can just escape from the tube exit. Integrating over the applicable tube surface, the total scattered flux leaving the tube which is emitted in a direction θ within $d\theta$ and passes through the tube exit is:

$$dF_s = 8r^2\sin^2\theta d\theta \int_{X_m}^{X_M} \nu(X)\left[1-(X_M-X)^2\tan^2\theta\right]^{1/2} dX \qquad (3.9)$$

where $X_m \leq X \leq X_M - \cot\theta$ for a real integrand.

Integrating over θ, yields the total scattered flux which is emitted in a direction such that it passes through the tube exit:

$$F_s = 8r^2 \int_0^{\theta_M} \sin^2\theta \int_{X_m}^{X_M} \nu(X)\left[1-(X_M-X)^2\tan^2\theta\right]^{1/2} dX d\theta\ . \qquad (3.10)$$

This flux is represented by a conical volume whose half angle is θ_M ($\theta_M = \tan^{-1}(X_M-X)^{-1}$) for any given X and extends to $\pi/2$ for $X \to X_M$. Let θ_M be $\tan^{-1}X^{-1}$, then the total scattered flux enters a conical volume, the half angle of which is the same as the unscattered beam half angle. In this case, the total scattered flux is represented by:

$$F_s = 8r^2 \int_0^{\tan^{-1}X^{-1}} \sin^2\theta \int_0^{X_M} \nu(X) \left[1-(X_M-X)^2\tan^2\theta\right]^{1/2} dX d\theta \,. \quad (3.11)$$

Now using the same arguments as in the case of the primary flux, the scattered flux contained within the total solid angle may be divided into increments of scattered flux contained in equal increments of solid angle, which are the same increments as in the case of the primary flux. The ratio of the increments of primary and scattered flux per unit solid angle, gives the flux signal-to-noise ratio.

4. Solution For The Martian Probe.- Some simplifying approximations, resulting from the "boundary conditions" for the Martian probe, can be applied to the expressions describing the properties of the scattered and unscattered flux. The approximations are not necessary to obtain a solution. They do however, decrease the computer program size and run time and therefore, were used when a negligible error was introduced in the solution. Since these expressions were used in the actual computer computations, they will be presented together with the data generated for those functions of interest.

4.1 Total transmission function. - Contained within the mathematical expression for the total transmission function (see Eq. 1.2.2), are the functions $\psi_1(S,\phi)$, $\psi_2(X,\phi)$, $\psi_3(X,\phi)$, and $F(S,O)$. The function $\psi_1(S,\phi)$ was presented as Eq. 1.1.1 and is:

$$\psi_1(S,\phi) = \frac{n_o v_m}{\sqrt{\pi}} \sin\phi\cos\phi \left\{ (1+S^2\cos^2\phi)e^{-S^2} + \sqrt{\pi} S\cos\phi \left(\frac{3}{2} + S^2\cos^2\phi\right) \right.$$

$$\left. \left[1 + \text{erf}\,(S\cos\phi)\right] e^{-S^2\sin^2\phi} \right\} . \qquad (4.1.1)$$

If we impose the condition that $S^2 > 10$, which is true of the Martian atmosphere for a probe speed in the vicinity of 4.0×10^5 cm/sec, the first term in the bracket can be neglected; producing an error of less than .05%. Under these conditions the expression for $\psi_1(S,\phi)$ becomes:

$$\psi_1(S,\phi) = n_o U \sin\phi\cos^2\phi \left\{ \left(\frac{3}{2} + S^2\cos^2\right) \left[1 + \text{erf}(S\cos\phi)\right] e^{-S^2\sin^2\phi} \right\} .$$

(4.1.2)

The expressions for $\psi_2(X,\phi)$ and $\psi_3(X,\phi)$ given in Eqs. 1.1.2 and 1.2.1 can be re-written as:

$$\psi_2(X,\phi) = \frac{2}{\pi}\left\{\tan^{-1}\left[\frac{1}{X^2\tan^2\phi} - 1\right]^{1/2} - X\tan\phi\left[1-X^2\tan^2\phi\right]^{1/2}\right\} \quad (4.1.3)$$

and

$$\psi_3(X,\phi) = e^{-\left[\frac{2r\sigma}{\cos\phi}\int_0^X n(X')dX'\right]} . \quad (4.1.4)$$

Using the above approximation ($S^2 > 10$), the expression for $F_p(S,O)$, given in Eq. 1.1.6, becomes:

$$F_p(S,O) = \pi r^2 n_o U . \quad (4.1.5)$$

Therefore, the approximated expression for the total transmission function becomes:

$$T(S,X) = \frac{2}{\pi}\left[\int_0^{\tan^{-1}X^{-1}}\left\{\sin\phi\cos^2\phi\left(\frac{3}{2} + S^2\cos^2\phi\right)\left[1+\mathrm{erf}(S\cos\phi)\right]e^{-S^2\sin^2\phi}\right\}\right.$$
$$\left\{\tan^{-1}\left[\frac{1}{X^2\tan^2\phi} - 1\right]^{1/2} - X\tan\phi\left[1-X^2\tan^2\phi\right]^{1/2}\right\}$$
$$\left.\left\{e^{-\frac{2r\sigma}{\cos\phi}\int_0^X n(X')dX'}\right\}d\phi\right] . \quad (4.1.6)$$

Presented in Fig. 3 are curves for this total transmission function vs atmospheric density and height above the Martian surface for various values of probe speed (U) and length-to-diameter ratio (X_M).

Having established the mathematical expression for the total transmission function, we can now calculate those properties of the sampler which have been written in terms of the total transmission function.

4.2 Internal tube diffuse gas density distribution.- The expression for the diffuse gas density distribution along the inlet tube was given in Eq. 1.3.2. In order to calculate the distribution as a function of X, a numerical integration of the total transmission function over X is required. Shown in Fig. 4 is a plot of n(X) as a function of X for a typical set of parameters (X_M = 4.0, $n_o = 5 \times 10^{15}$ cm^{-3}, $U = 4 \times 10^5$ cm/sec). These parameters were chosen as representative of the actual sampler geometry and represent the distribution near the maximum undisturbed density allowable for retaining free molecular flow conditions (the mean free path-to-tube diameter ratio for these parameters is 1.06). To show how the diffuse gas density changes as a function of undisturbed gas density, a plot of the maximum value of n(X) as a function of n_o is presented in Fig. 5. The increase of the maximum diffuse gas density for larger values of X_M and U was predictable; however, the decrease in the slope of the curve at higher values of the undisturbed gas density was not. The slope decreases at these higher densities because the tube temperature increases more rapidly

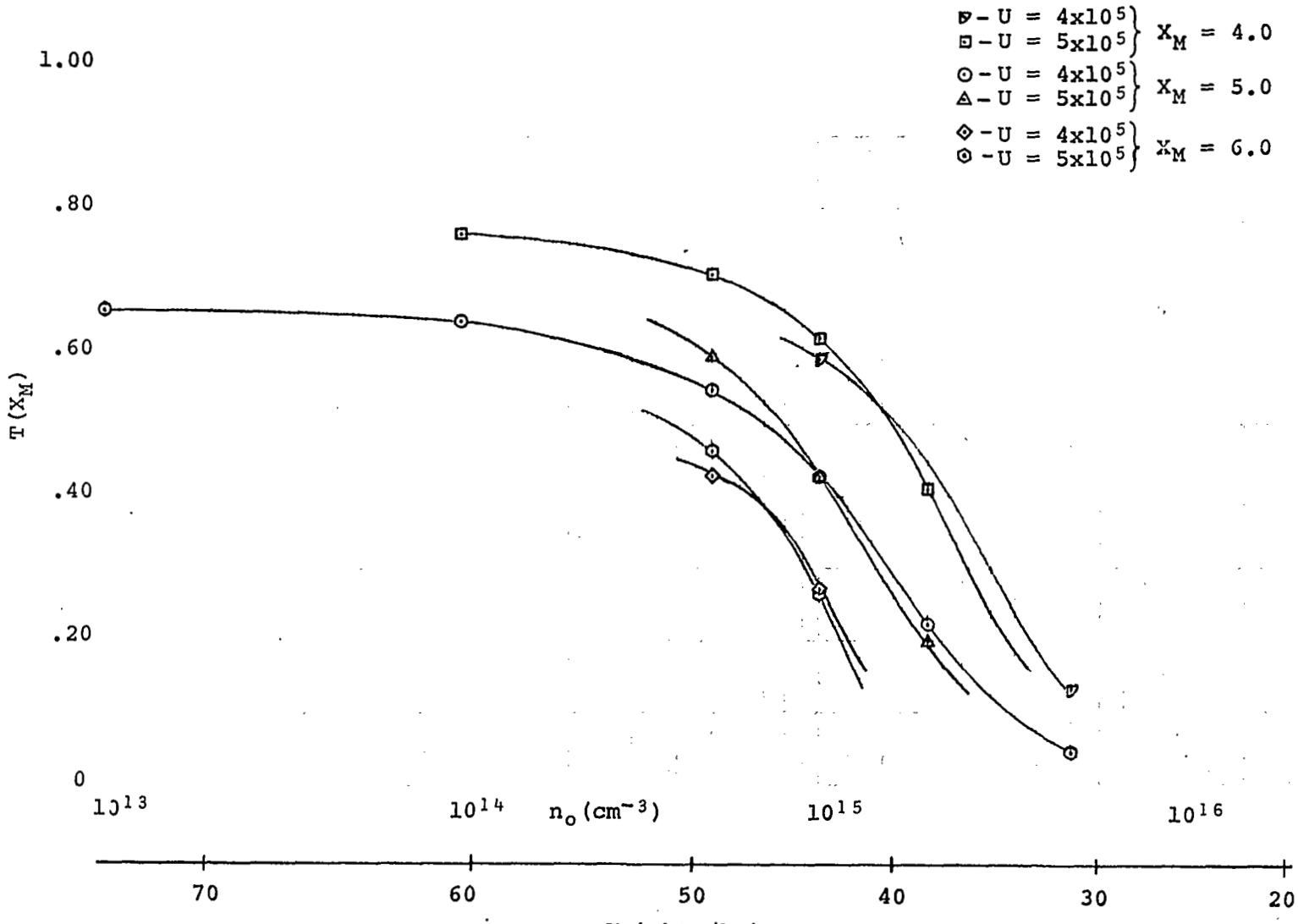

Fig. 3
Total transmission vs. number density

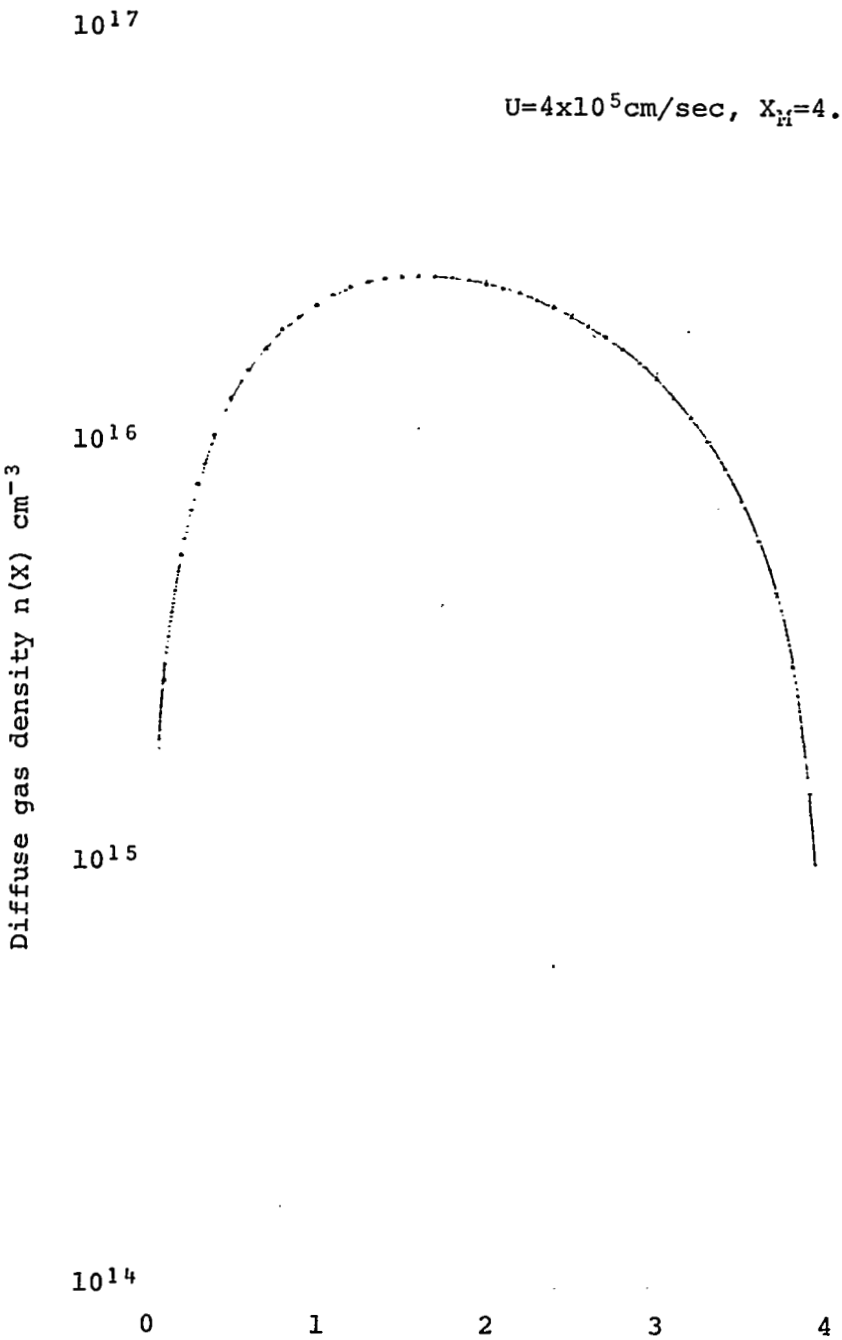

Fig. 4

Diffuse gas density distribution

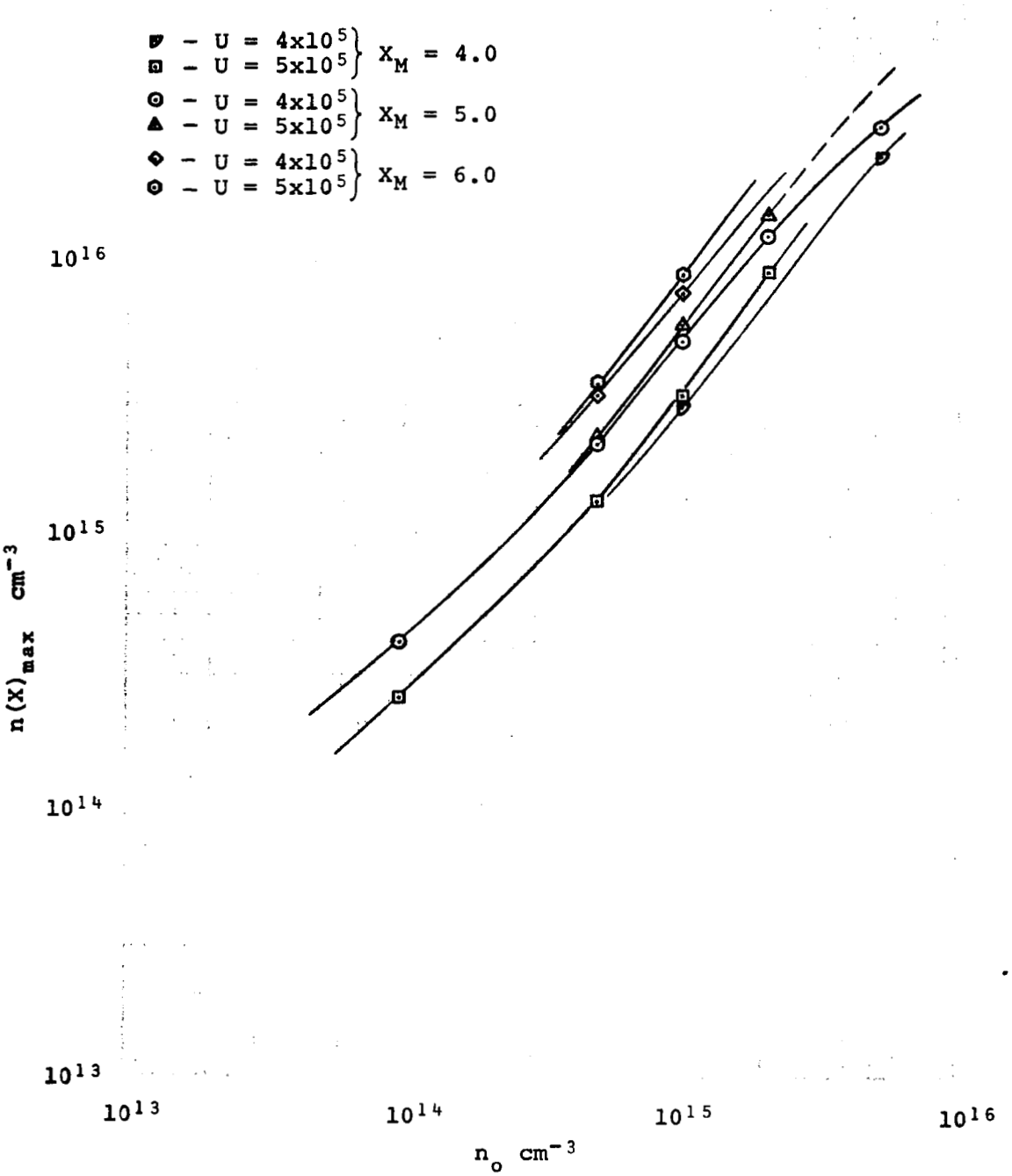

Fig. 5

Diffuse gas density maximum vs. undisturbed gas density

than the combined effects of gas-gas and gas-wall attenuation. The temperature controls the magnitude of the diffuse gas average velocity, which is inversely proportional to the diffuse gas density.

4.3 Tube temperature.-

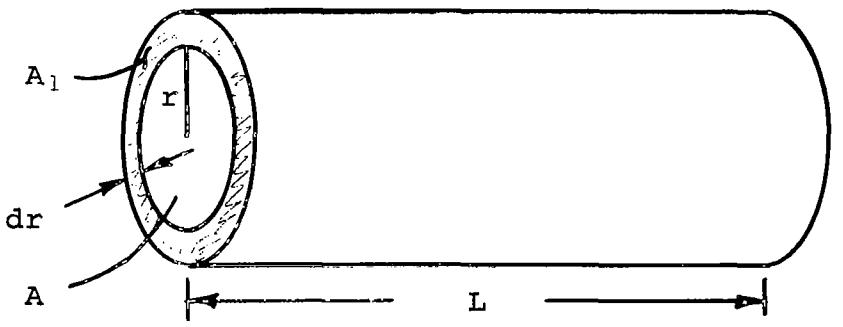

In deriving an expression for the tube temperature, the following points were considered: 1) Since the tube has a finite wall thickness, there is energy dissipated at the solid annular cross-section of the tube entrance (A_1 in the figure above) as well as along the tube interior surface. 2) There is no flux incident on the outer cylindrical surface, except for the case of a single tube sampler, since it is shielded by adjacent tubes in the bundle. 3) Since the molecular flux is incident normal to the annular cross-section and at near grazing incidence to the tube inner surface, the energy accomodation coefficient for the two surfaces will be substantially different. 4) The total gas enthalpy is considered to be com-

posed of kinetic energy; the PV term being neglegible in comparison. 5) The mechanism for energy dissipation is assumed to be radiation since the entrance tubes are thermally isolated from the probe.

The total power dissipated in a single tube is:

$$P_i = \frac{1}{2} mU^2 n_o U A_1 \alpha_1 + \frac{1}{2} mU^2 \left[F_p(S,O) - F_p(S,X_M)\right]\alpha_2 \qquad (4.3.1)$$

where: $1/2\ mU^2$ = Particle kinetic energy

$n_o U A_1$ = Total particle flux incident on the annular cross-section

α_1 = Energy accomodation coefficient for normal incidence

$\left[F_P(S,O) - F_P(S,X_M)\right]$ = Particle flux incident on the tube inner surface

α_2 = Energy accomodation coefficient for grazing incidence.

The total power radiated by a single tube is:

$$P_r = 2\varepsilon_1 A_1 \sigma_s T_T^4 + 2\varepsilon A \sigma_s T_T^4 \qquad (4.3.2)$$

where: ε_1 = Total normal emittance of the solid.

ε = Effective emittance of the tubular cavity.

A_1 = Tube cross-sectional area (solid).

A = Tube entrance area.

σ_s = Stefan-Boltzmann constant.

T_T = Tube temperature.

Writing an energy balance equation and solving for the tube temperature we get:

$$2\sigma_s T_T^4 \left[\varepsilon_1 A_1 + \varepsilon A\right] = \frac{1}{2} n_o m U^3 \left[A_1 \alpha_1 + A\alpha_2 \left\{1-T(S,X_M)\right\}\right]$$

$$2\sigma_s T_T^4 \left[\varepsilon_1 2\pi r dr + \varepsilon \pi r^2\right] = \frac{1}{2} n_o m U^3 \left[2\pi r dr \alpha_1 + \pi r^2 \alpha_2 \left\{1-T(S,X_M)\right\}\right]$$

$$T_T = \left[\frac{n_o m U^3}{4\sigma_s} \left\{\frac{\alpha_1 2\frac{dr}{r} + \left|1-T(S,X_M)\right| \alpha_2}{\varepsilon_1 \frac{2dr}{r} + \varepsilon}\right\}\right]^{1/4} \qquad (4.3.3)$$

Since the total normal emittance of platinum at its melting point is ≈ 0.2 and dr/r = 0.1, the term $2\varepsilon_1$ dr/r can be neglected; thus we get:

$$T_T = \left[\frac{n_o m U^3}{4\varepsilon\sigma_s}\left\{2\alpha_1 \frac{dr}{r} + \left[1-T(S,X_M)\right]\alpha_2\right\}\right]^{1/4}. \qquad (4.3.4)$$

In the computations, ε was taken to be 1.0 since $X_M \geq 4.0$, $\alpha_1 = 1.0$, and $\alpha_2 = 0.1$. Presented in Fig. 6 are curves for tube temperature vs undisturbed gas density and height above the Martian surface. As in previous figures, the values of X_M and U are varied and a family of curves are presented.

4.4 Mean free path within the tube.- One of the limiting conditions in the analysis of the performance of the sampler is the onset of viscous flow; either external or internal. As the mean free path in the undisturbed atmosphere approaches the dimensions of the probe, the conditions for the formation of an incipient shock wave exist. As this localized, high density front moves towards the sampler inlet, the conclusions based on the analytical model are no longer valid and these conditions represent one of the limits of predictable operation. However; before these conditions exist, a second limiting condition will have arisen, namely the transition from free molecular to viscous flow based on the diffuse gas density inside the sampler inlet tubes. Since the properties of the internal tube diffuse gas density, especially the angular

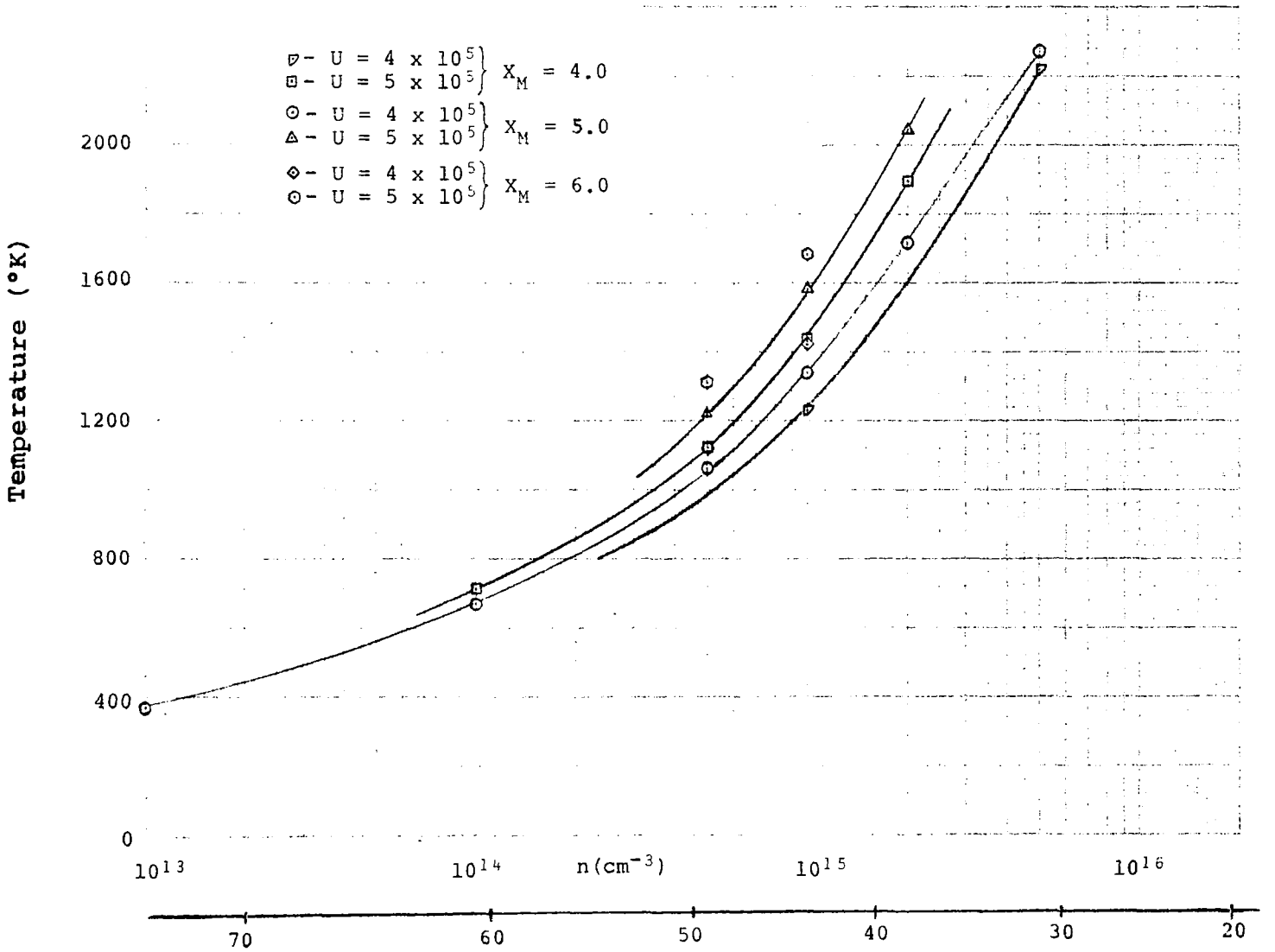

Height (km)

Fig. 6

Sampler temperature vs number density

distribution, are based on free molecular flow calculations; the mean free path based on the diffuse gas density must be greater than the dimensions of the inlet tubes. In order to establish the validity of the signal-to-noise calculations, the ratio of the mean free path to the inlet tube diameter ($\lambda/2r$) is also monitored as a function of the input parameters. The mean free path which is calculated is based on the maximum diffuse gas density in the tube and is expressed as:

$$\frac{\lambda}{2r} = \frac{1}{2r\sqrt{2}\sigma n(X)_M} \qquad (4.4.1)$$

where σ = collision cross-section for diffuse molecules. As was shown in Fig. 5, this density, $n(X)_M$, is a strong function of X so that the limiting conditions imposed by this parameter are conservative. Therefore, results obtained for conditions such that $\lambda/2r \geq 1$ are valid for the assumption that free molecular flow conditions exist. Presented in Fig. 7 are curves for $\lambda/2r$ vs undisturbed gas density.

4.5 Gas-gas scattering attenuation.- In section (1.4), the angular distribution of the unscattered exit flux was calculated on the basis of the transmission through imaginary tubes with length-to-diameter ratios of X_E. Since $X_E >> 1$, an additional approximation is valid in the calculation of these $T(S,X_E)$:

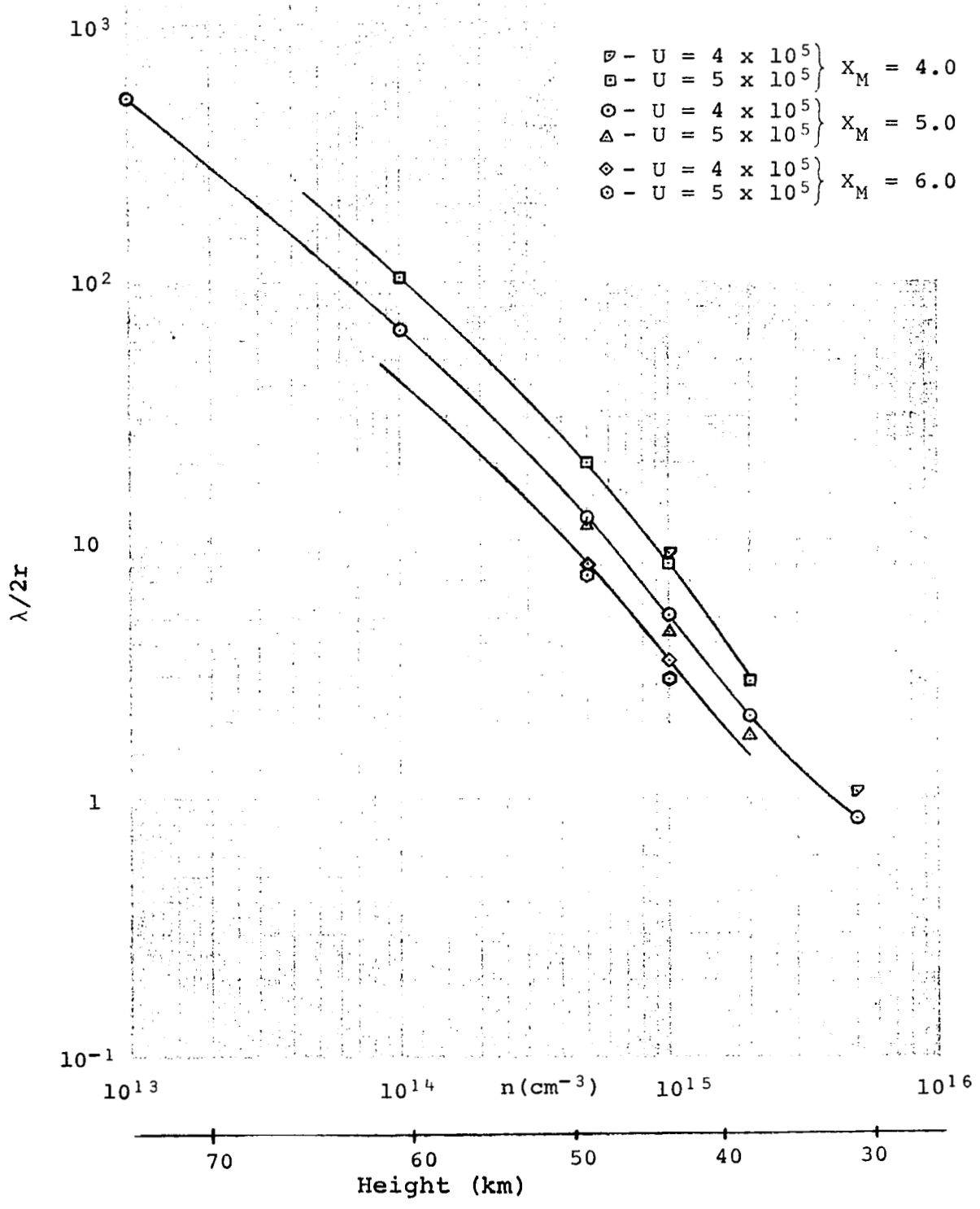

Fig. 7

Mean free path/tube diameter vs number density

$$\tan\phi \simeq \sin\phi \simeq \phi$$

$$\cos\phi \simeq 1$$

Using these approximations in Eq. (4.1.6) for T(S,X) we get:

$$T(S,X) = \frac{2}{\pi}\left[\int_0^{X^{-1}}\left\{\phi\left(\frac{3}{2}+S^2\right)\left[1+\mathrm{erf}(S)\right]e^{-S^2\phi^2}\right\}\right.$$

$$\left\{\cos^{-1}(X\phi) - X\phi\left[1-X^2\phi^2\right]^{1/2}\right\}$$

$$\left.\left\{e^{-2r\sigma\int_0^X n(X')dX'}\right\}d\phi\right] . \qquad (4.5.1)$$

Eq. (4.1.6) contained the assumption that $S^2 > 10$ so that 3/2 can be neglected with respect to S^2 and erf (S) $\simeq$ 1. Furthermore $\psi_3(X,\phi)$ is now independent of ϕ and can be taken out of the integral. Thus we have:

$$T(S,X_E) \sim \frac{4}{\pi}\gamma \int_0^{X_E^{-1}} S^2 e^{-S^2\phi^2}\left[\cos^{-1}(X\phi) - X\phi(1 - X^2\phi^2)^{1/2}\right]\phi d\phi \qquad (4.5.2)$$

where

$$\gamma = e^{-2r\sigma\int_0^{X_M} n(X')dX'}. \qquad (4.5.3)$$

The function $e^{-2r\sigma\int_0^{X_M} n(X')dX'}$ is defined as the gas-gas scattering attenuation coefficient and is a constant which when applied to the geometrical transmission function yields the total transmission function. Thus,

$$T_g(S,X_E) \approx \frac{4}{\pi} \int_0^{X_E^{-1}} S^2 e^{-S^2\phi^2}\left[\cos^{-1}(X\phi) - X\phi(1 - X^2\phi^2)^{1/2}\right]\phi d\phi \qquad (4.5.4)$$

is just the geometrical transmission function for X_E ($X_E > X_M$). Since the diffuse gas density goes to zero at $X = X_M$, the gas-gas scattering attenuation coefficient (GGSA) is evaluated only up to X_M; for X_E the value of GGSA at $X = X_M$ is applied. Presented in Fig. 8 are data for the dependence of GGSA on the undisturbed gas density.

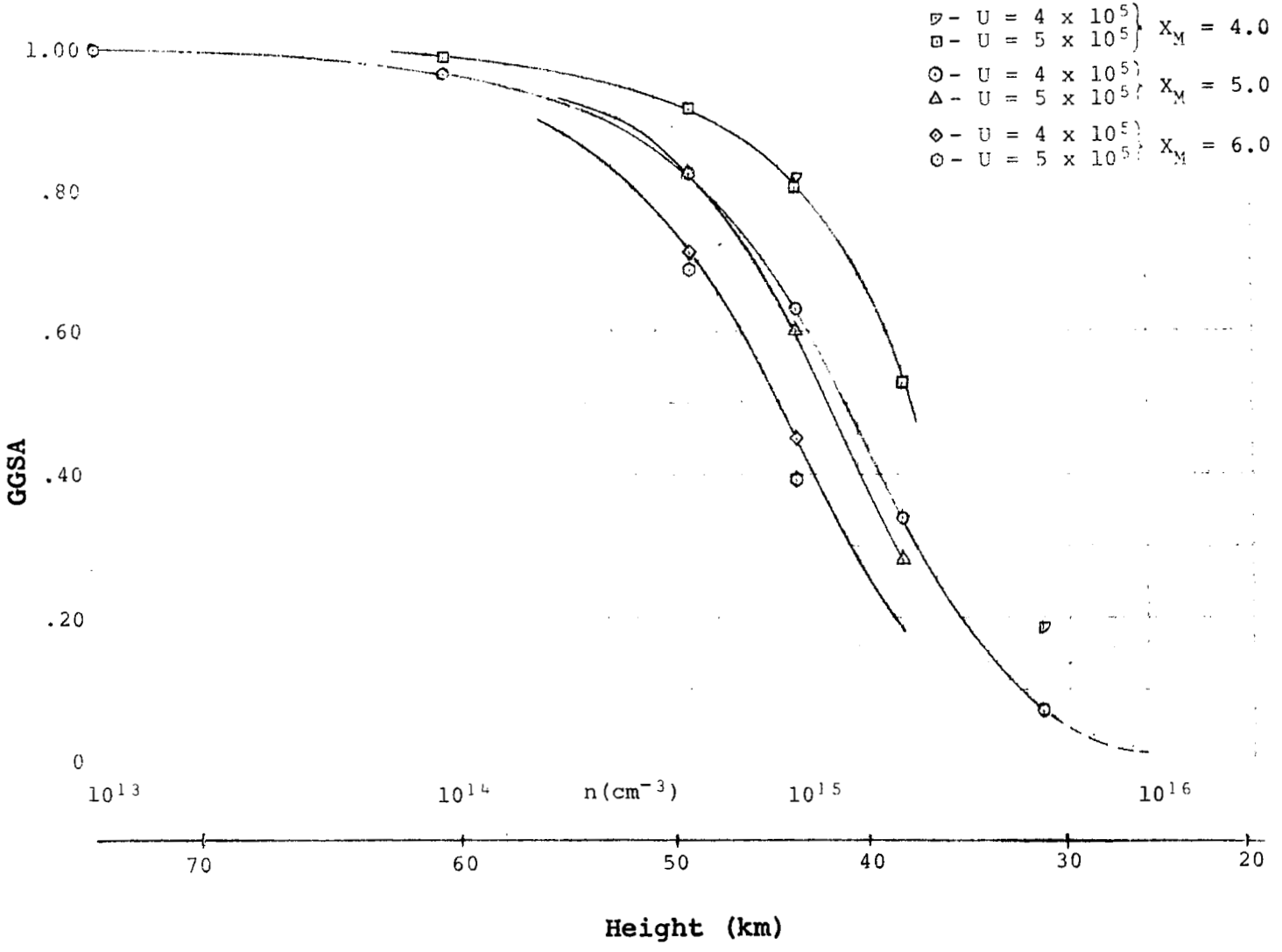

Fig. 8

Gas-gas scattering attenuation vs number density

4.6 Angular distribution of unscattered exit flux.- In order to calculate the transmission function for values of X_E corresponding to equal increments of solid angle we must integrate Eq. (4.5.2). Upon integrating by parts we get:

$$T(S,X_E) = \gamma \left\{ 1 - \frac{4}{\pi} \int_0^{X_E^{-1}} X e^{-S^2\phi^2} (1 - X^2\phi^2)^{1/2} d\phi \right\} . \qquad (4.6.1)$$

Therefore, the amount of primary flux which is transmitted through the imaginary tube with a length-to-diameter ratio of X_E is:

$$F_P(S,X_E) = F_P(S,O)\, T(S,X_E) \qquad (4.6.2)$$

or

$$F_P(S,X_E) = F_P(S,O) \cdot \gamma \cdot T_g(S,X_E) \qquad (4.6.3)$$

$$F_P(S,X_E) = \pi r^2 n_o U \gamma \left\{ 1 - \frac{4}{\pi} \int_0^{X_E^{-1}} X e^{-S^2\phi^2} (1 - X^2\phi^2)^{1/2} d\phi \right\} . \qquad (4.6.4)$$

Thus, we have an expression for the incremental primary flux contained in an element of solid angle, which is defined in terms of values of X_E as was shown in section (1.4). If $T_g(S,X_E)$ is printed out in the computer data we also have additional information on the behavior of both the geometrical transmission function and the total transmission function for large values of X.

Presented in Fig. 9 are data for the angular distribution of transmitted primary flux as a function of the plane half angle ϕ for a specific set of input parameters.

4.7 Angular distribution of scattered exit flux.- Equation (3.11) represents the total diffuse flux which is transmitted through the tube exit and contained in a solid angle whose plane half angle θ_M has been limited to $\tan^{-1}X_M^{-1}$, which is the maximum transmission angle for the primary flux. For the purpose of calculating the signal-to-noise ratio, this value of θ_M is sufficient even though the major fraction of the total diffuse flux is contained in solid angles with plane half angles greater than $\tan^{-1}X_M^{-1}$. To specify completely the angular distribution of the diffuse flux, this limitation on θ_M would have to be removed and the integration over θ_M allowed to increase to the value specified by X_m as indicated in Eq. (3.10). Since this represented additional computation which was not necessary for the present goal of the program, this task was deferred until a later time.

For the purpose of calculating signal-to-noise ratios for specific solid angles, θ_M was divided into increments, whose

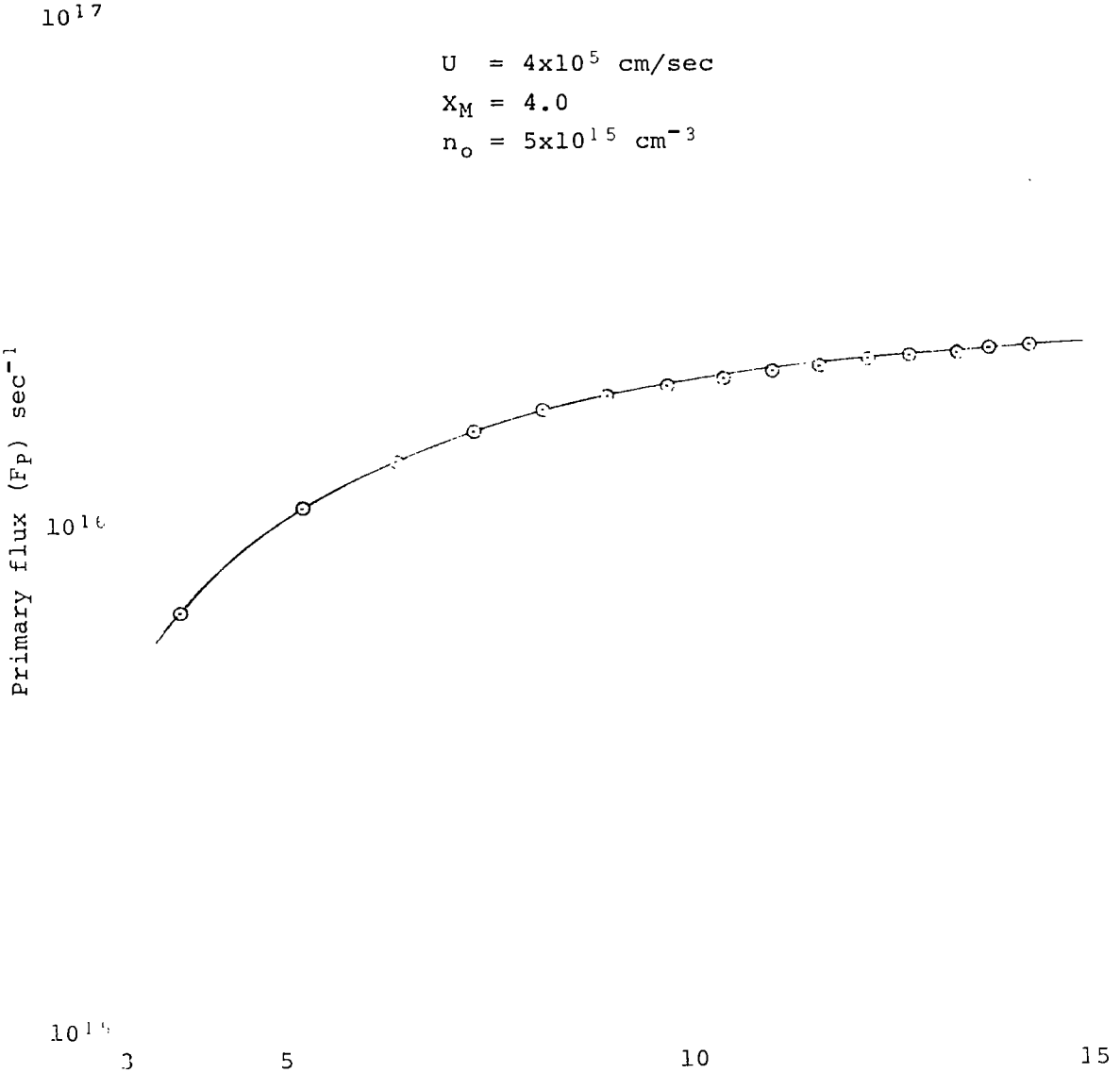

Fig. 9

Angular distribution of primary flux

values were the same as the ϕ_M increments of the primary flux, and were representative of identical solid angle increments as defined for the primary flux given in Eq. (1.4.5).

The computations yield angular distribution data for the scattered flux as a function of the plane half angle θ as presented in Fig. 10.

4.8 Signal-to-noise ratio.- The comparison of the total primary and scattered flux contained in an element of solid angle yields the flux signal-to-noise ratio. Figure 11 contains the angular distribution curves of the primary and scattered flux for a typical set of input parameters. It can be seen that the signal-to-noise ratio is a strong function of the plane half angle ϕ(or θ). Therefore, the proper design of the complete gas sampling system is strongly influenced by this data and the solid angle subtended by the limiting apertures (skimmer and collimator) is kept as small as possible consistent with the total beam flux required for adequate sensitivity over a significant range of densities.

Besides this dependence on beam half angle there is, of course, also a dependence on all the other parameters. Shown in Fig. 12 are curves for the dependence of signal-to-noise ratio on undisturbed gas density for various values of U and X_M. The beam half angle is .063 rad which was the value chosen in the actual gas sampling system design, which will be discussed in a later section. The final choice of a design geometry is influenced primarily by the signal-to-noise ratio and the total primary flux transmitted into the instrument region of the probe.

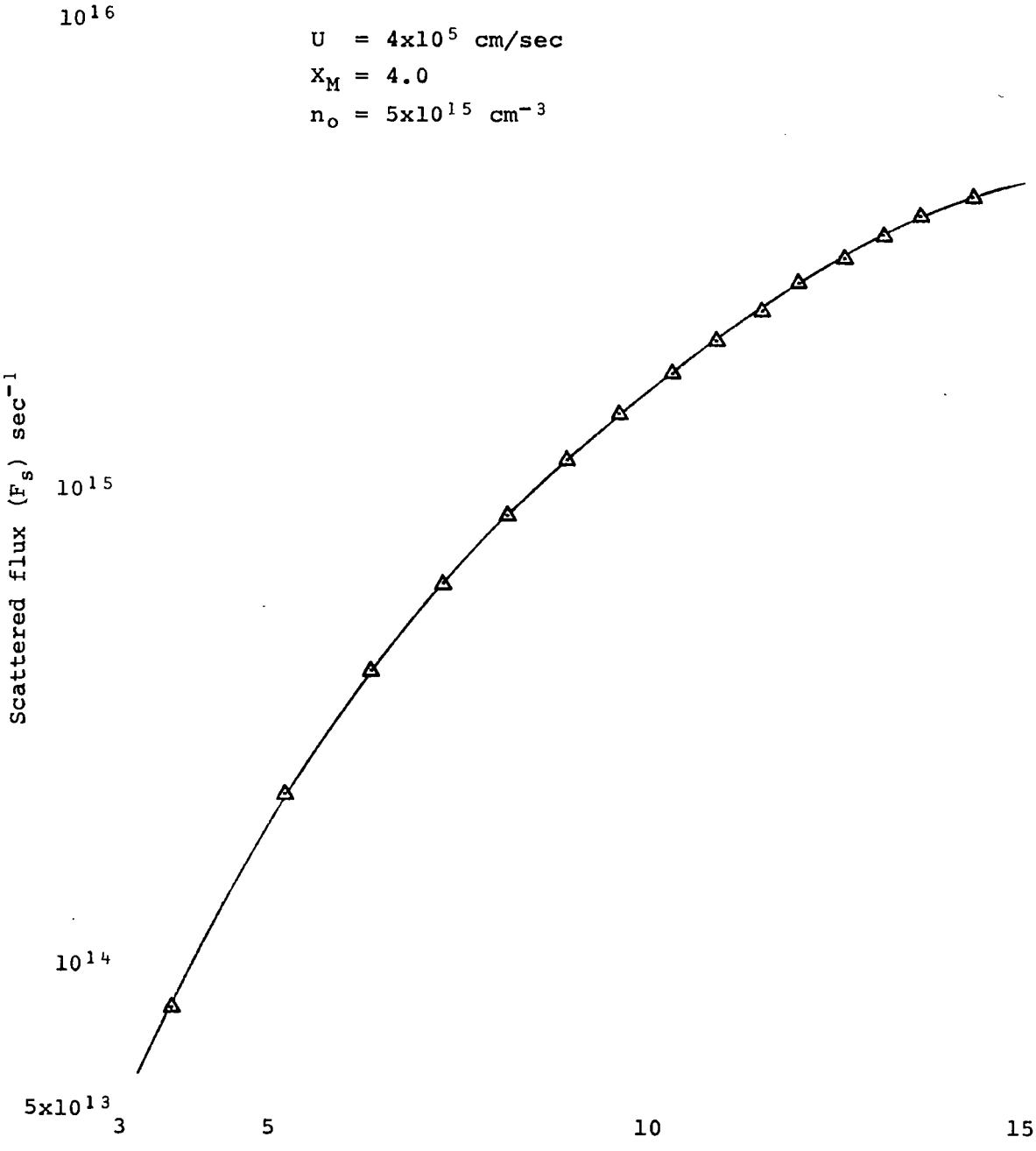

Fig. 10

Angular distribution of scattered flux

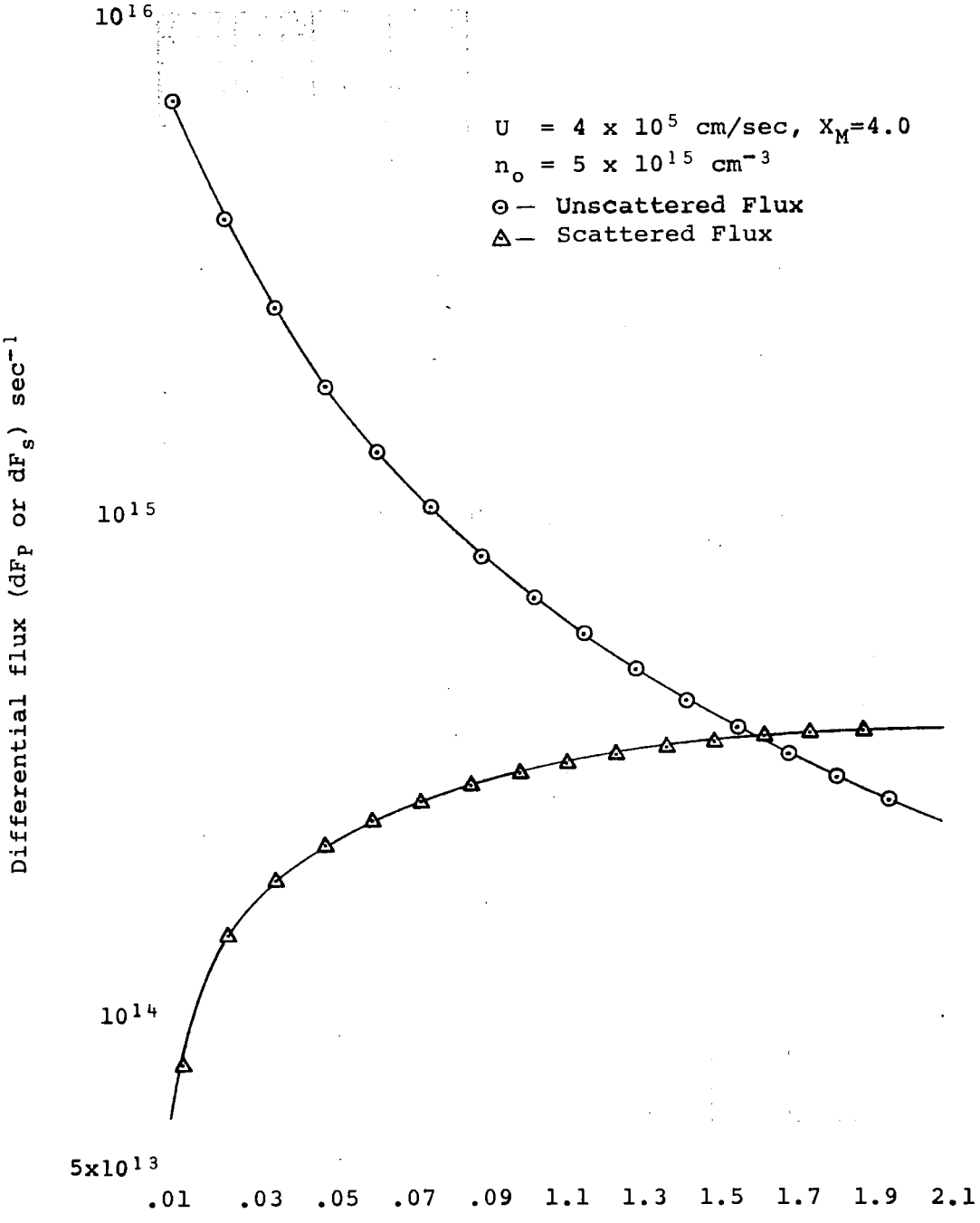

Fig. 11

Differential flux vs. solid angle

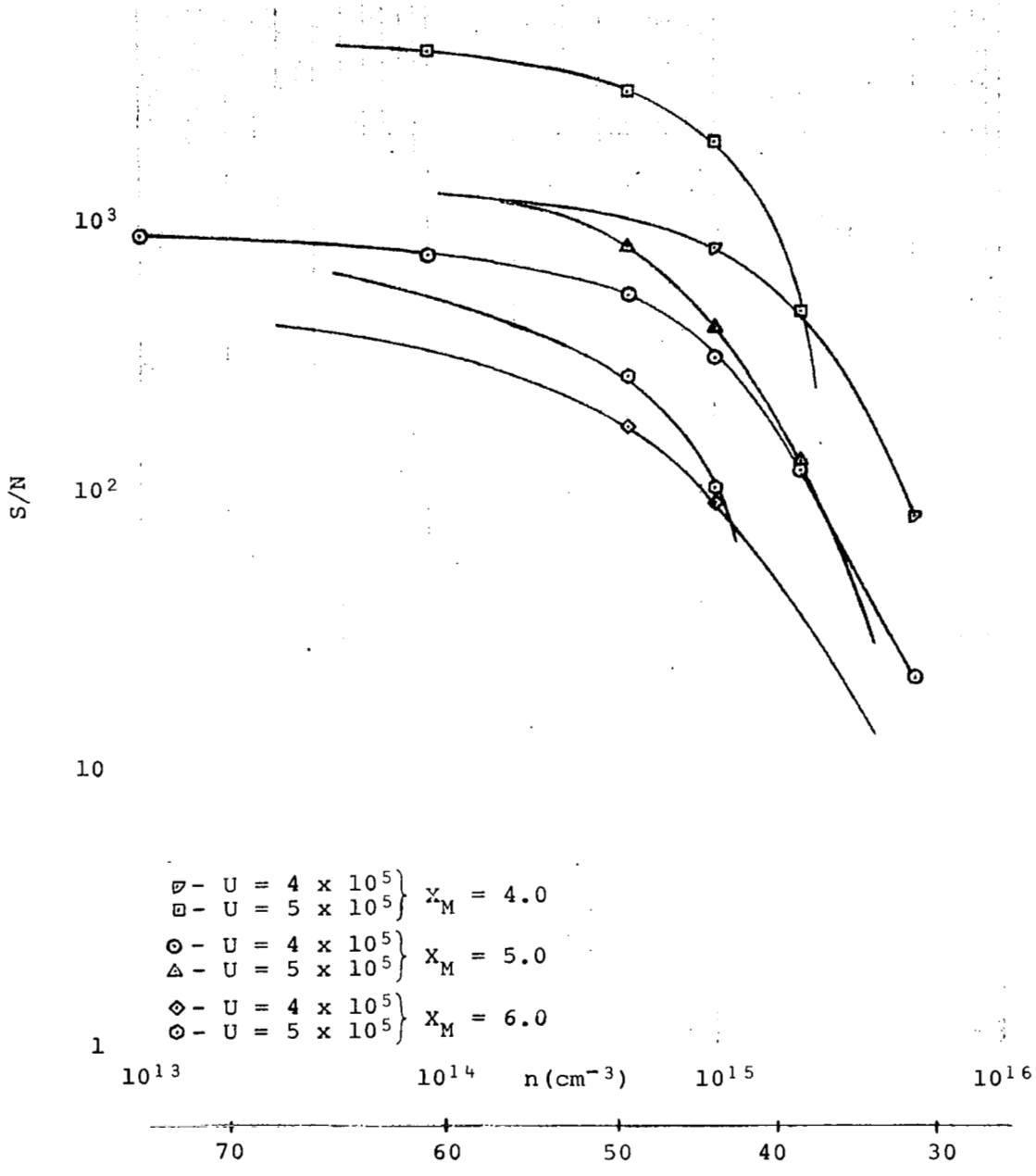

Fig. 12

Signal-to-noise ratio vs number density

Presented in Fig. 13 are the data for the variation of the total flux contained in a solid angle with a plane half angle of .063 rad with undisturbed gas density. Based on the data of Figs. 12 and 13 one can establish the dynamic range of the gas sampling system once the sensitivity of the instrumentation is established.

It should be pointed out, however; that the signal-to-noise ratio which has just been presented is based on the flux ratio. Since the instrumentation for the analysis of the properties of the transmitted flux measure the average density, the flux signal-to-noise ratio must be converted to the density equivalent. Since the unscattered flux is traveling at a velocity U with respect to the probe, its average velocity is U (assuming $U >> v_m$) and the scattered flux is traveling with an average velocity of $\bar{v}$, since it was emitted at the temperature of the entrance tube. Therefore, the average density equivalent signal-to-noise ratio is given approximately as:

$$\left(\frac{S}{N}\right)_n = \left(\frac{S}{N}\right)_F \cdot \frac{1}{S_1} \qquad (4.8.1)$$

where $S_1 = U/\bar{v}$; $\bar{v}$ being the average velocity of the diffuse flux based on the tube temperature. In cases where the beam half angle used is large, more attention to the average values of the functions $dF_p/d\omega$ and $dF_s/d\omega$ must be given than is implied in Eq. (4.8.1) which applies to small solid angle increments.

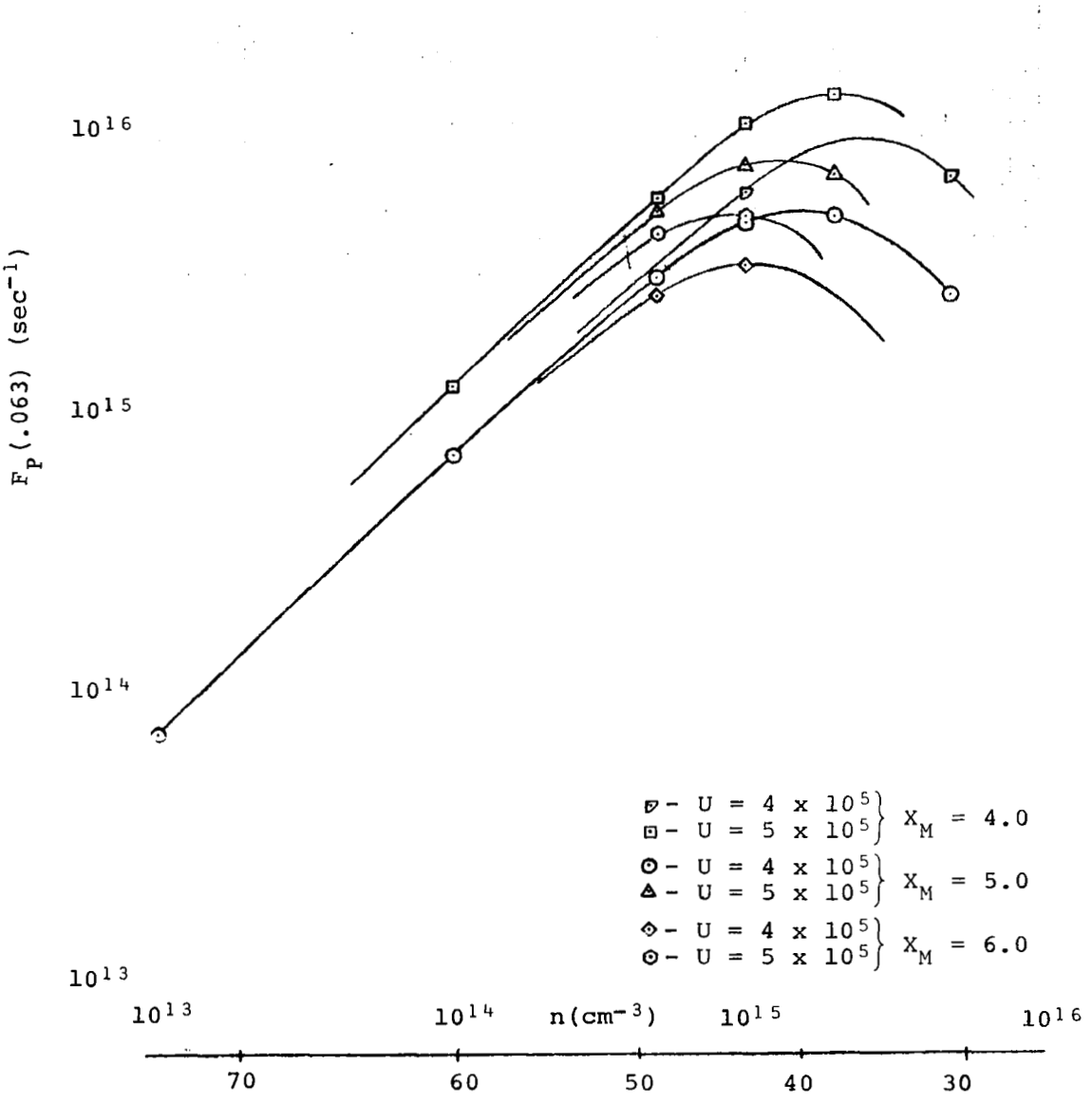

Fig. 13

Total primary flux included in a solid angle representative of the plane half angle of .063 radians on the tube axis vs number density

B. Computer Program

In the previous section (under the discussion of the solution for the Martian probe), the derivation of the mathematical relationships used in the computer program together with the numerical data were presented. These data were the result of a parameter survey of the mathematical functions with the probe speed (U), the length-to-diameter ratio (X_M), and the undisturbed gas density (n_o) used as variable input parameters. The following is a paginated copy of the final version of the computer program and a typical set of printed data from the program. There is a sufficient amount of verbal commentary throughout the program to define the nomenclature and to indicate the actual calculation occurring within a given loop. These numerical data were then collated to produce the dependence of the physical parameters with undisturbed gas density (or height above the Martian surface) for various values of U and X_M.

DRIVE1

```
110C    THIS PROGRAM USES A SELFCONSISTENT ITERATIVE METHOD TO CALCULATE:
120C    THE UNSCATTERED TRANSMISSION AS A FUNCTION OF X;
130C    THE DIFFUSE GAS DENSITY DISTRIBUTION AS A FUNCTION OF X;
140C    THE TUBE MEAN TEMPERATURE;
150C    THE MEAN FREE PATH/2R (IN THE TUBE);
160C    THE UNSCATTERED EXIT FLUX ANGULAR DISTRIBUTION;
170C    THE INNER SURFACE COLLISION FREQUENCY AS A FUNCTION OF X;
180C    THE DIFFUSE GAS EXIT FLUX ANGULAR DISTRIBUTION;
190C    THE SIGNAL-TO-NOISE RATIO.
200C    FOR: ANGLE OF ATTACK=0.0; S*S>=10.0
210C    ALL PHYSICAL PARAMETERS IN THE CGS SYSTEM.
220 $FILE XF,TF,AF,DFPF
230 DIMENSION XA(40),TS(40),SUMTS(40),DEN(40),SUMDEN(40),DFP(15),DU(15)
240 CONTINUE
250 $USE APX1
260 CONTINUE
270 $USE INPUTS
280 CONTINUE
290 $USE WORK1
300 CONTINUE
310 WRITE(1,208)(10+M,XA(M),M=1,MMAX)
320 WRITE(2,208)(10+M,TS(M),M=1,MMAX)
330 WRITE(3,217)11,KMAX,12,LMAX,13,MMAX,
340 WRITE(3,208)14,U,15,R,16,XMAX,17,DENO,18,PI,19,SPI,20,VM,
370 WRITE(4,208)(10+K,DFP(K),K=1,KMAX)
380 PRINT,1"TO CONTINUE:  CALL DRIVE2"
390 GOTO1000;999STOP"ERR";1000
400 $USE ERRFUN
410 $OPT TIME
420 $OPT SIZE
430 END
```

APX1

```
110 200FORMAT(E14.8)
120 201FORMAT(F7.3,2E14.8)
130 202FORMAT(E14.8,2X,E14.8)
140 203FORMAT(I1)
150 204FORMAT(I2)
160 205FORMAT(I3)
170 206FORMAT(//,4X,1HX,7X,4HT(X),9X,6HDEN(X),/)
180 207FORMAT(//,3X,2HXE,8X,5HT(XE),9X,6HPHIMAX,11X,1HW,14X,2HFP,/)
190 208FORMAT(I2,1X,E14.8)
200 209FORMAT(/,4X,1HX,8X,5HNU(X),/)
210 210FORMAT(F7.3,2X,E14.8)
220 211FORMAT(F7.3,4(1X,E14.8))
230 212FORMAT(//,6X,5HTHMAX,8X,6HDFD/DW,7X,7HFD(THM),7X,3HS/N,11X,
231 +3HDFD,/)
240 213FORMAT(4(1X,E14.8))
250 214FORMAT(//,1X,1HK,7X,5HDW(K),10X,6HDFP(K),10X,6HDFP/DW,/)
260 215FORMAT(I2,3(2X,E14.8))
270 216FORMAT(3X,E14.8)
280 217FORMAT(I2,1X,I2)
290 218FORMAT(3X,I2)
300 219FORMAT(5E14.8)
```

INPUTS

```
110 U=5.0E+5
120C    U=ENTRY VELOCITY
130 ALF1=1.0
131C    ALF1=ENERGY ACCOMMODATION COEFFICIENT FOR NORMAL INCIDENCE.
140 ALF2=0.1
141C    ALF2=ENERGY ACCOMMODATION COEFFICIENT FOR GRAZING INCIDENCE.
150 EPS1=0.0
151C    EPS1=TOTAL EMISSIVITY OF RADIATING TUBE SURFACE.
160 EPS2=1.0
161C    EPS2=EFFECTIVE EMISSIVITY OF TUBE APERTURE.
170 R=5.0E-3
180C    R=TUBE RADIUS
185 DR=0.1*R
186C    DR=TUBE WALL THICKNESS.
190 XMAX=4.0
200C    XMAX=L/2R (L=TUBE LENGTH)
210 TO=150.0
220C    TO=TEMPERATURE OF THE UNDISTURBED ATMOSPHERE
230 DENO=2.0E+15
```

INPUTS CONTINUED

```
240C    DENO=MOLECULAR NUMBER DENSITY OF THE UNDISTURBED ATMOSPHERE
250 ANO=44.0
260C    ANO=MOLECULAR MASS NUMBER
270 SIG=0.216E-14
280C    SIG=MOLECULAR COLLISION CROSS SECTION
290 TT=TO
300C    TT=TUBE TEMPERATURE
310 PMASS=1.67252E-24
320C    PMASS=PROTON MASS
330 SIGSB=5.6697E-5
340C    SIGSB=STEFAN-BOLTZMANN CONSTANT
350 BK=1.38054E-16
360C    BK=BOLTZMANN CONSTANT
370 PI=4.0*ATAN(1.0)
375 SPI=SQRT(PI)
380 KMAX=15
390C    KMAX=NUMBER OF SOLID ANGLE INCREMENTS
400 LMAX=6
410C    LMAX=NUMBER OF ITERATIONS
420 MMAX=40
430C    MMAX=NUMBER OF X INCREMENTS
440 VM=SQRT(2.0*BK*TO/(PMASS*ANO))
450C    VM=MOST PROBABLE MOLECULAR SPEED IN THE UNDISTURBED ATMOSPHERE
460 S=U/VM
470 IF(MMAX-15)1,2,2
480 1
490 PRINT,"SET MMAX>=15"
500 GOTO999
510 2
```

ERRFUN

```
110C    THIS SUBPROGRAM CALCULATES ERF(Y),Y>=0.0 .
120 FUNCTION FACT(N)
130 FACT=1.0
140 DO1I=1,N
150 FACT=FACT*I
160 1
170 RETURN
180 FUNCTION ERF(Y)
190 IF(Y-0.1)3,3,4
200 3
210 B=1E-16
```

ERRFUN CONTINUED

```
220 GOTO6
230 4
240 IF(Y-2.5)5,10,10
250 5
260 B=1E-9
270 6
280 A1=0.0
290 I=0
300 7
310 Z=FACT(I)
320 A0=((-1.0)↑I)*(Y↑(2*I+1))/((2*I+1)*Z)
330 A1=A0+A1
340 A5=ABS(A0/A1)
350 IF(A5-B)9,8,8
360 8
370 I=I+1
380 GOTO7
390 9
400 ERF=1.12837918*A1
410 GOTO13
420 10
430 IF(Y-4.15)11,12,12
440 11
450 G1=EXP(-Y*Y)
460 T=1.0/(1.0+Y*0.327591)
470 ERF=1.0-(0.254829592*T-0.284496736*T*T+1.421413741*T*T*T
480 +-1.453152027*T*T*T*T+1.061405429*T*T*T*T*T)*G1
490 GOTO13
500 12
510 ERF=1.0
520 13
530 RETURN
540 END
```

WORK1

```
110 PRINT,"U      =",;PRINT200,U
120 PRINT,"ALF1   =",;PRINT200,ALF1
125 PRINT,"ALF2   =",;PRINT200,ALF2
126 PRINT,"EPS1   =",;PRINT200,EPS1
127 PRINT,"EPS2   =",;PRINT200,EPS2
130 PRINT,"R      =",;PRINT200,R
135 PRINT,"DR     =",;PRINT200,DR
140 PRINT,"XMAX   =",;PRINT200,XMAX
150 PRINT,"ANO    =",;PRINT200,ANO
160 PRINT,"SIG    =",;PRINT200,SIG
170 PRINT,"DENO   =",;PRINT200,DENO
180 PRINT,"TO     =",;PRINT200,TO
190 PRINT,"VM     =",;PRINT200,VM
200 PRINT,"S      =",;PRINT200,S
210 PRINT,"KMAX   =",;PRINT203,KMAX
220 PRINT,"LMAX   =",;PRINT203,LMAX
230 PRINT,"MMAX   =",;PRINT204,MMAX
240 FKMAX=KMAX
250 FLMAX=LMAX
260 FMMAX=MMAX
270
280 DO50L=1,LMAX
290 PRINT,↑↑"IN ITERATION  ",;PRINT203,L,;PRINT,↑
300 VBAR=SQRT(8.0*BK*TT/(PI*PMASS*ANO))
310C    VBAR=TUBE DIFFUSE GAS MEAN MOLECULAR SPEED
320 S1=U/VBAR
330C    THE FOLLOWING LOOP CALCULATES THE TRANSMISSION FUNCTION T(S,X)
340 DO20M=1,MMAX
350 FM=M
360 X=XMAX*FM/FMMAX
370 XA(M)=X
380 PHIMAX=ATAN(1.0/X)
390 NMAX=PHIMAX*1.0E+2
400C    NMAX=NUMBER OF PHI INCREMENTS
410 FNMAX=NMAX
420 DPHI=PHIMAX/FNMAX
430 TSX=0.0
440 FO=0.0
450 AN1=2.0*R*SIG*SUMDEN(M)
460C    THE FOLLOWING LOOP INTEGRATES OVER PHI
470 DO10N=1,NMAX
480 FN=N
490 PHI=PHIMAX*FN/FNMAX
500 SI=SIN(PHI)
510 C=COS(PHI)
520 SS=S*SI
530 IF(SS-7.0)5,5,4
540 4
550 PSI1=0.0
560 GOTO9
```

WORK1 CONTINUED

```
570 5
580 SC=S*C
590 IF(SC-2.8)6,6,7
600 6
610 PSI1=SI*C*C*(1.5+SC*SC)*(1.0+ERF(SC))*EXP(-SS*SS)
620 GOTO8
630 7
640 PSI1=2.0*SI*C*C*(1.5+SC*SC)*EXP(-SS*SS)
650 8
660 TANPHI=SI/C
670 XT=X*TANPHI
680 PSI2=ATAN(SQRT(1.0/(XT*XT)-.999999))-XT*SQRT(1.000005-XT*XT)
690 PSI3=EXP(-AN1/C)
700 F=PSI1*PSI2*PSI3
710 TSX=TSX+(FO+F)*DPHI/PI
720 9
730 FO=F
740 10
750 TS(M)=TSX
760 IF(M-1)999,15,18
770 15
780 IF(L-1)999,16,17
790 16
800 PRINT,"NMAX   =",;PRINT205,NMAX
810 PRINT,!
820 17
830 SUMTSX=(1.0+TSX)*X/2.0
840 GOTO19
850 18
860 SUMTSX=SUMTSX+(TS(M)+TS(M-1))*(XA(M)-XA(M-1))/2.0
870 19
880 SUMTS(M)=SUMTSX
890 20
900 DELTA=DDNO=0.0
910 AM1=(8.0/PI)*DENO*S1
920 AM2=SUMTS(MMAX)/XA(MMAX)
930C    THE FOLLOWING LOOP CALCULATES THE DIFFUSE GAS DENSITY AS A
940C    FUNCTION OF X
950 DO30M=1,MMAX
960 DENOLD=DEN(M)
970 DEN(M)=AM1*(SUMTS(M)-AM2*XA(M))
980 IF(M-5)30,21,21
990 21
1000 IF(M+5-MMAX)22,22,30
1010 22
1020 DD=ABS(DEN(M))-ABS(DEN(M-1))
1030 IF(DD)24,24,23
1040 23
1050 DENMAX=DEN(M)
1060 MXDENM=M
```

```
1070 24
1080 IF(ABS(DEN(M)-DENOLD)-ABS(DDNO))30,30,25
1090 25
1100 DDNO=DEN(M)-DENOLD
1110 DELTA=2.0*DDNO/(DENOLD+DEN(M))
1120 MDELTA=M
1130 30
1140C    THE FOLLOWING LOOP CALCULATES THE INTEGRAL OF THE DIFFUS
1150C    GAS DENSITY OVER X
1160 DO40M=1,MMAX
1170 IF(M-1)999,31,32
1180 31
1190 SDENX=DEN(1)*XA(1)/2.0
1200 GOTO40
1210 32
1220 SDENX=SDENX+(DEN(M)+DEN(M-1))*(XA(M)-XA(M-1))/2.0
1230 SUMDEN(M)=SDENX
1240 40
1250 TT=SQRT(SQRT(ANO*PMASS*DENO*U*U*U/(4.0*EPS2*SIGSB)*(2.0*ALF1*DR/R
1251 ++(1.0-TS(MMAX))*ALF2)))
1260 FLO2R=1.0/(SQRT(8.0)*R*SIG*DENMAX)
1270 GGSA=EXP(-2.0*R*SIG*SUMDEN(MMAX))
1280 PRINT,"DELTA =",;PRINT200,DELTA
1290 PRINT,"MDELTA=",;PRINT204,MDELTA
1300 PRINT,"DENMAX=",;PRINT200,DENMAX
1310 PRINT,"MXDENM=",;PRINT204,MXDENM
1320 PRINT,"TT     =",;PRINT200,TT
1325 PRINT,"S1     =",;PRINT200,S1
1330 PRINT,"FLO2R  =",;PRINT200,FLO2R
1340 PRINT,"GGSA   =",;PRINT200,GGSA
1350 50
1360 PRINT,!"NUMAX =",;PRINT200,DENMAX*VBAR/4.0
1370 PRINT,!
1380 PRINT206;PRINT201,(XA(M),TS(M),DEN(M),M=1,MMAX)
1390C    THE FOLLOWING LOOP CALCULATES THE ANGULAR DISTRIBUTION OF THE
1400C    UNSCATTERED EXIT FLUX BY CALCULATING THE TRANSMISSION FUNCTION
1410C    FOR A SET OF X>=XMAX(X-EXTENDED) BUT APPLYING THE GAS-GAS
1420C    SCATTERING ATTENUATION FUNCTION APPLICABLE TO XMAX TO ALL T(XE).
1430C    THE TRANSMISSION FUNCTION IS CALCULATED USING THE APPROXIMATION:
1440C    T(XE)=GGSA*(1-(4/PI)*INTEGRAL[0,1/XE][F(XE,PHI)]*DPHI), WHERE
1450C    F(XE,PHI)=XE*SQRT(1-(XE*PHI)↑2)*EXP(-(S*PHI)↑2)
1460C    THE APPROXIMATION IS ACCURATE FOR 1<<X<<S.
1461C    T(XE) IS ACTUALLY PRINTED WITHOUT THE FACTOR GGSA BUT THE
1462C    PRIMARY FLUX IS PRINTED WITH THE FACTOR GGSA APPLIED.
1470 PRINT207
1480 PMO=0.0
1490 FPO=0.0
1500 DO70K=1,KMAX
1510 FK=K
1520 XE=XMAX*SQRT(FKMAX/FK)
```

WORK1 CONTINUED

```
1530 NMAX=200.0/XE
1540 FNMAX=NMAX
1550 PHIMAX=1.0/XE
1560 ADP=2.0/(PI*FNMAX)
1570 TXE=1.0
1580 FO=1.0
1590
1600 DO60N=1,NMAX
1610 FN=N
1620 PHI=PHIMAX*FN/FNMAX
1630 F=SQRT(1.0000005-(XE*PHI)↑2)*EXP(-(S*PHI)↑2)
1640 TXE=TXE-(FO+F)*ADP
1650 FO=F
1660 60
1670 FP=PI*R*R*U*DENO*TXE*GGSA
1680 DFP(K)=FP-FPO
1690 DW(K)=PI*(PHIMAX↑2-PMO↑2)
1700 DFPDW=DFP(K)/DW(K)
1710 W=PI*PHIMAX↑2
1720 PRINT211,XE,TXE,PHIMAX,W,FP
1730 FPO=FP
1740 PMO=PHIMAX
1750 70
1760 PRINT 205,NMAX
1770 PRINT214
1780 DO75K=1,KMAX
1790 PRINT215,K,DW(K),DFP(K),DFP(K)/DW(K)
1800 75
```

DRIVE2

```
110 $FILE XF,TF,AF,DFPF
120 DIMENSION XA(41),TS(41),DFP(15),FNU1(41),FNU(41),PSI5(41,41)
130 CONTINUE
140 $USE APX1
150 READ(3,218)KMAX,LMAX,MMAX,
155 FKMAX=KMAX
156 FMMAX=MMAX
160 READ(3,216)U,R,XMAX,DENO,PI,SPI,VM,
180 IMAX=MMAX+1
190 XA(1)=0.0
200 READ(1,216)(XA(I),I=2,IMAX)
210 TS(1)=1.0
```

DRIVE2 CONTINUED

```
220 READ(2,216)(TS(I),I=2,IMAX)
230 PRINT210,XA(2),TS(2);PRINT210,XA(41),TS(41)
240 READ(4,216)(DFP(K),K=1,KMAX)
250 CONTINUE
260 $USE WORK2
270 CONTINUE
280 GOTO1000;999STOP"ERR";1000
290 $OPT TIME
300 $OPT SIZE
310 END
```

WORK2

```
110 IPMAX=IMAX
120C    THE FOLLOWING LOOP LOADS THE MATRIX PSI5(I,I')
130 DO95I=1,IMAX
140
150 DO90IP=1,IPMAX
160 PSI5(I,IP)=1.0-ABS(XA(I)-XA(IP))*((XA(I)-XA(IP))↑2+1.5)
170 +*1.0/((SQRT((XA(I)-XA(IP))↑2+1.0))↑3)
180 90
190 95
200 LPMAX=10*LMAX
210 ANU1=-DENO*U/4.0
220 ANU2=DENO*VM/(2.0*SPI)
230C    THE FOLLOWING LOOP ITERATES THE SOLUTION FOR NU(X)
240 PRINT,
250 DO140LP=1,LPMAX
260 IF(LP-LPP)99,98,98
270 98
280 PRINT,"IN ITERATION  ",;PRINT204,LP
290 PRINT,
300 99
310 DNUMAX=0.0
320C    THE FOLLOWING LOOP CALCULATES NU(X)
330 DO120I=1,IMAX
340 SNUSX=0.0
350
360 DO100IP=1,IPMAX
370 F=FNU1(IP)*PSI5(I,IP)
380 IF(IP-1)999,102,101
390 101
400 SNUSX=SNUSX+(FO+F)*(XA(IP)-XA(IP-1))/2.0
```

WORK2 CONTINUED

```
410 102
420 FO=F
430 100
440 IF(I-1)999,103,104
450 103
460 FNU(1)=ANU2+SNUSX
470 GOTO120
480 104
490 IF(I-IMAX)106,105,999
500 105
510 FNU(IMAX)=ANU1*(TS(IMAX)-TS(IMAX-1))/(XA(IMAX)-XA(IMAX-1))+SNUSX
520 GOTO120
530 106
540 FNU(I)=ANU1*(TS(I+1)-TS(I-1))/(XA(I+1)-XA(I-1))+SNUSX
550 120
560C   THE FOLLOWING LOOP TEST FOR NU(X) CONVERGENCE
570 DO125I=1,IMAX
580 DNU=FNU(I)-FNU1(I)
590 IF(ABS(DNUMAX)-ABS(DNU))121,125,125
600 121
610 DNUMAX=DNU
620 IDNUMX=I
630 125
640 DELNU=2.0*DNUMAX/(FNU(IDNUMX)+FNU1(IDNUMX))
650C   THE FOLLOWING LOOP TRANSFURS THE NEW MATRIX ELEMENTS FNU(I)
660C   TO THE MATRIX FNU1(I).
670 DO130I=1,IMAX
680 FNU1(I)=FNU(I)
690 130
700 IF(LP-LPP)140,133,133
710 133
720 LPP=LPP+5
730 PRINT,"DELNU =",;PRINT200,DELNU
740 PRINT,"IDNUMX=",;PRINT205,IDNUMX
750 PRINT,"NU    =",;PRINT200,FNU(IDNUMX)
760 PRINT,
770 140
780 PRINT209;PRINT210,(XA(I),FNU(I),I=1,IMAX)
790 PRINT,
800
810C   THE FOLLOWING LOOP CALCULATES THE ANGULAR DISTRIBUTION OF THE
820C   SCATTERED EXIT FLUX AND THE SIGNAL-TO-NOISE RATIO.
830
840
850
860 PRINT212
870 DX=XMAX/FMMAX
880 SSFDO=0.0
890 THMO=0.0
900
```

WORK2 CONTINUED

```
910 DO170K=1,KMAX
920 FK=K
930 THM=SQRT(FK/FKMAX)*ATAN(1.0/XMAX)
940 JMAX=(500.0/PI)*SQRT(FK/FKMAX)*ATAN(1.0/XMAX)
950 FJMAX=JMAX
960 DTH=THM/FJMAX
970 SSFD=0.0
980
990 DO160J=1,JMAX
1000 FJ=J
1010 THJ=THM*(FJ/FJMAX)
1020 SJ=(SIN(THJ))↑2
1030 TJ=SJ*(1.0/COS(THJ))↑2
1040 AFD=8.0*R*R*DX*DTH*SJ
1050
1060 DO150I=1,IMAX
1070 FD=FNU(I)*SQRT(1.0000005-TJ*(XMAX-XA(I))↑2)
1080 IF(I-1)999,145,146
1090 145
1100 SFD=0.5*FD
1110 GOTO150
1120 146
1130 IF(I-IMAX)147,148,999
1140 147
1150 SFD=SFD+FD
1160 GOTO150
1170 148
1180 SFD=SFD+0.5*FD
1190 150
1200 IF(J-JMAX)155,156,999
1210 155
1220 SSFD=SSFD+AFD*SFD
1230 GOTO160
1240 156
1250 SSFD=SSFD+0.5*AFD*SFD
1260 160
1270
1280 DFD=SSFD-SSFDO
1290 SN=DFP(K)/DFD
1300 DFDDW=DFD/(PI*(THM↑2-THMO↑2))
1310 PRINT219,THM,DFDDW,SSFD,SN,DFD
1320
1330
1340 SSFDO=SSFD
1350 THMO=THM
1360 170
```

```
IN APX1
IN .FIRST
IN INPUTS
IN .FIRST
IN WORK1
IN .FIRST
IN ERRFUN
IN .FIRST
TIME AT LINE NO. 410, 150/6
SIZE AT LINE NO. 420, PROG 2601, DIM 461, COMM 0

U      = .40000000E+06
ALFBAR= .27000000E+00
R      = .50000000E-02
XMAX   = .40000000E+01
ANO    = .44000000E+02
SIG    = .27000000E-14
DENO   = .50000000E+16
TO     = .15000000E+03
VM     = .23723192E+05
S      = .16861137E+02
KMAX   =15
LMAX   =6
MMAX   =40


IN ITERATION  1

NMAX   =147


DELTA = .20000000E+01
MDELTA=20
DENMAX= .25177627E+17
MXDENM=20
TT     = .16568509E+04
FLO2R = .10401751E+01
GGSA   = .16334932E+00


IN ITERATION  2

DELTA = .24875214E+00
MDELTA=12
DENMAX= .29547446E+17
MXDENM=17
TT     = .22292446E+04
FLO2R = .88634191E+00
GGSA   = .13184927E+00
```

```
IN ITERATION  3

DELTA =-.17307175E+00
MDELTA=22
DENMAX= .25681703E+17
MXDENM=16
TT    = .22436573E+04
FLO2R = .10197587E+01
GGSA  = .17440105E+00


IN ITERATION  4

DELTA =-.44267836E-01
MDELTA=13
DENMAX= .24647248E+17
MXDENM=16
TT    = .22241200E+04
FLO2R = .10625584E+01
GGSA  = .18598337E+00


IN ITERATION  5

DELTA =-.98448613E-02
MDELTA= 8
DENMAX= .24582696E+17
MXDENM=16
TT    = .22187106E+04
FLO2R = .10653486E+01
GGSA  = .18641805E+00


IN ITERATION  6

DELTA = .35146648E-02
MDELTA=23
DENMAX= .24638411E+17
MXDENM=16
TT    = .22185068E+04
FLO2R = .10629395E+01
GGSA  = .18568000E+00

NUMAX = .63414065E+21
```

X	T(X)	DEN(X)
.100	.98852344E+00	.27682243E+16
.200	.96731347E+00	.54555994E+16
.300	.94329628E+00	.80311063E+16
.400	.91371719E+00	.10474044E+17
.500	.87926826E+00	.12758610E+17
.600	.84117857E+00	.14863754E+17
.700	.80030338E+00	.16773581E+17
.800	.75762187E+00	.18476732E+17
.900	.71413070E+00	.19966737E+17
1.000	.67064161E+00	.21241599E+17
1.100	.62775379E+00	.22302810E+17
1.200	.58612062E+00	.23154961E+17
1.300	.54608966E+00	.23805117E+17
1.400	.50807256E+00	.24262224E+17
1.500	.47211081E+00	.24536346E+17
1.600	.43851178E+00	.24638411E+17
1.700	.40732979E+00	.24580242E+17
1.800	.37839044E+00	.24373365E+17
1.900	.35181725E+00	.24029179E+17
2.000	.32744484E+00	.23558980E+17
2.100	.30517102E+00	.22973403E+17
2.200	.28487867E+00	.22282540E+17
2.300	.26651931E+00	.21496073E+17
2.400	.24981197E+00	.20622869E+17
2.500	.23478023E+00	.19671159E+17
2.600	.22115397E+00	.18648565E+17
2.700	.20896315E+00	.17562113E+17
2.800	.19802441E+00	.16418450E+17
2.900	.18823688E+00	.15223522E+17
3.000	.17950805E+00	.13982794E+17
3.100	.17175375E+00	.12701295E+17
3.200	.16489815E+00	.11383659E+17
3.300	.15887346E+00	.10034164E+17
3.400	.15361963E+00	.86567721E+16
3.500	.14908397E+00	.72551659E+16
3.600	.14529353E+00	.58329654E+16
3.700	.14206725E+00	.43934093E+16
3.800	.13944225E+00	.29393800E+16
3.900	.13746841E+00	.14739758E+16
4.000	.13597689E+00	.00000000E+01

XE	T(XE)	PHIMAX	W	FP
		-01		
15.492	.22908959E+00	.64549722E-01	.13089969E-01	.66817520E+16
10.954	.36264834E+00	.91287093E-01	.26179939E-01	.10577200E+17
8.944	.45069031E+00	.11180340E+00	.39269908E-01	.13145080E+17
7.746	.51222262E+00	.12909944E+00	.52359877E-01	.14939765E+17
6.928	.55762850E+00	.14433757E+00	.65449847E-01	.16264097E+17
6.325	.59264664E+00	.15811388E+00	.78539816E-01	.17285456E+17
5.855	.62061396E+00	.17078251E+00	.91629786E-01	.18101166E+17
5.477	.64357618E+00	.18257419E+00	.10471975E+00	.18770894E+17
5.164	.66284965E+00	.19364917E+00	.11780972E+00	.19333035E+17
4.899	.67931843E+00	.20412415E+00	.13089969E+00	.19813373E+17
4.671	.69359858E+00	.21408721E+00	.14398966E+00	.20229875E+17
4.472	.70613325E+00	.22360680E+00	.15707963E+00	.20595468E+17
4.297	.71725000E+00	.23273733E+00	.17016960E+00	.20919705E+17
4.140	.72719666E+00	.24152295E+00	.18325957E+00	.21209815E+17
4.000	.73616458E+00	.25002000E+00	.19634954E+00	.21471378E+17

50

K	DW(K)	DFP(K)	DFP/DW
1	.13089969E-01	.66817520E+16	.51044825E+18
2	.13089969E-01	.38954476E+16	.29759028E+18
3	.13089969E-01	.25678803E+16	.19617160E+18
4	.13089969E-01	.17946850E+16	.13710383E+18
5	.13089969E-01	.13243326E+16	.10117156E+18
6	.13089969E-01	.10213581E+16	.78026015E+17
7	.13089969E-01	.81571005E+15	.62315657E+17
8	.13089969E-01	.66972858E+15	.51163495E+17
9	.13089969E-01	.56214082E+15	.42944396E+17
10	.13089969E-01	.48033743E+15	.36695076E+17
11	.13089969E-01	.41650251E+15	.31818448E+17
12	.13089969E-01	.36559302E+15	.27929249E+17
13	.13089969E-01	.32423721E+15	.24769899E+17
14	.13089969E-01	.29010987E+15	.22162762E+17
15	.13089969E-01	.26156310E+15	.19981950E+17

TO CONTINUE: CALL DRIVE2

```
DRIVE2

IN APX1
IN .FIRST
IN WORK2
IN .FIRST
TIME AT LINE NO. 290, 69/6
SIZE AT LINE NO. 300, PROG 1417, DIM 3721, COMM 0

    .100    .98852344E+00
   4.000    .13597689E+00

IN ITERATION    1

DELNU = .20000000E+01
IDNUMX= 10
NU    = .21745065E+21

IN ITERATION    5

DELNU = .16233911E+00
IDNUMX= 15
NU    = .71469465E+21

IN ITERATION   10

DELNU = .63181812E-01
IDNUMX= 18
NU    = .10241905E+22

IN ITERATION   15

DELNU = .33547725E-01
IDNUMX= 20
NU    = .11939890E+22

IN ITERATION   20

DELNU = .19295246E-01
IDNUMX= 21
NU    = .13060923E+22

IN ITERATION   25

DELNU = .11359954E-01
IDNUMX= 21
NU    = .14018640E+22

IN ITERATION   30

DELNU = .68920751E-02
IDNUMX= 21
NU    = .14626219E+22

IN ITERATION   35

DELNU = .42544934E-02
IDNUMX= 21
NU    = .15011669E+22
```

```
IN ITERATION  40

DELNU = .26536736E-02
IDNUMX= 21
NU    = .15256200E+22

IN ITERATION  45

DELNU = .16657332E-02
IDNUMX= 21
NU    = .15411331E+22

IN ITERATION  50

DELNU = .10497159E-02
IDNUMX= 21
NU    = .15509747E+22

IN ITERATION  55

DELNU = .66314723E-03
IDNUMX= 21
NU    = .15572182E+22

IN ITERATION  60

DELNU = .41958279E-03
IDNUMX= 21
NU    = .15611792E+22
```

X	NU(X)
0.000	.57633026E+21
.100	.73831574E+21
.200	.88220889E+21
.300	.10119406E+22
.400	.11412631E+22
.500	.12585874E+22
.600	.13623155E+22
.700	.14522641E+22
.800	.15275760E+22
.900	.15864352E+22
1.000	.16358258E+22
1.100	.16703056E+22
1.200	.16928072E+22
1.300	.17043472E+22

1.400	.17061819E+22
1.500	.16991086E+22
1.600	.16836617E+22
1.700	.16616359E+22
1.800	.16334305E+22
1.900	.15995781E+22
2.000	.15611792E+22
2.100	.15186110E+22
2.200	.14722023E+22
2.300	.14227938E+22
2.400	.13705928E+22
2.500	.13159217E+22
2.600	.12590775E+22
2.700	.12001214E+22
2.800	.11396305E+22
2.900	.10775909E+22
3.000	.10141442E+22
3.100	.94940529E+21
3.200	.88346683E+21
3.300	.81640585E+21
3.400	.74829445E+21
3.500	.67903564E+21
3.600	.60911523E+21
3.700	.53874615E+21
3.800	.46771277E+21
3.900	.39708357E+21
4.000	.32895333E+21

THMAX	DFD/DW	FD(THM)	S/N	DFD
.63253209E-01	.64964475E+16	.81656532E+14	.81827526E+02	.81656532E+14
.89453547E-01	.11686389E+17	.22854758E+15	.26519299E+02	.14689105E+15
.10955777E+00	.14919917E+17	.41608218E+15	.13692835E+02	.18753460E+15
.12650642E+00	.17410330E+17	.63491980E+15	.82009891E+01	.21883763E+15
.14143848E+00	.19458577E+17	.87950270E+15	.54146575E+01	.24458289E+15
.15493809E+00	.21182275E+17	.11457515E+16	.38361046E+01	.26624876E+15
.16735226E+00	.22658860E+17	.14305600E+16	.28640643E+01	.28480856E+15
.17890709E+00	.23932255E+17	.17313744E+16	.22263847E+01	.30081440E+15
.18975963E+00	.25031129E+17	.20460010E+16	.17866920E+01	.31462660E+15
.20002421E+00	.25979235E+17	.23725448E+16	.14709743E+01	.32654373E+15
.20978716E+00	.26775248E+17	.27090939E+16	.12375682E+01	.33654914E+15
.21911554E+00	.27445172E+17	.30540636E+16	.10597830E+01	.34496970E+15
.22806269E+00	.27974314E+17	.34056843E+16	.92212203E+00	.35162072E+15
.23667184E+00	.28374932E+17	.37623406E+16	.81341593E+00	.35665624E+15
.24497863E+00	.28610064E+17	.41219523E+16	.72734865E+00	.35961172E+15

SAMPLER DEVELOPMENT

A. Materials Investigation

Of the classes of materials considered applicable for the fabrication of the gas sampler, pure metals and metallic alloys were preferred. Materials such as refractory oxides and glasses were not immediately ruled out since they possessed high strength and the ability to be fabricated into small diameter tubes with high geometrical transparency. However; because of their brittleness and the necessity of providing a transition to the metallic members, they were considered as secondary materials. Most of the metallic elements can be eliminated because of low melting points; of those remaining, a high fraction are unacceptable due to high chemical reactivity, for example the refractory metals and titanium, or because they are not ductile at room temperature. The latter property is one of the requirements necessary for most of the fabrication techniques considered applicable. One class of metals, the platinum family, seemed to possess the proper balance of desireable qualities. The platinum metals and alloys possess the proper physical and mechanical properties, are compatible with the fabrication techniques chosen, and are commerically available at a realistic cost.

Mechanical properties data for the platinum metals and alloys, are not available in large quantities and there is considerable scatter in the data from different sources. Some

of this discrepency comes from the different methods of measurement and instruments used, some from the non-uniformity of the material sample, impurities in the sample, differing previous histories, and some from the interpretation of the results. In comparing the relative merits of the materials, an attempt was made to be selective on the basis of data generated under similar conditions.

In selecting a material to be used for the sampler inlet, two aspects had to be considered: 1) the workability of the material would have to be consistent with the fabrication techniques; hence an evaluation of the cold working and annealing characteristics 2) the material would have to withstand the high temperature entry conditions while retaining sufficient strength for geometrical stability.

Although the inclusion of much of the graphical data on the mechanical properties of the platinum metals is not essential to the conclusions to be drawn in this section, it is included for information purposes. These data have been included in Appendix C and reference to these data will be made as they are discussed in the main text.

1. Chemical Reactivity.- Since the materials to be chosen for the sampler would have to be stable and inert to a variety of atmospheres at high temperatures, some of the platinum metals were eliminated on the basis of their relatively high oxidation rates. Presented in Fig. 14 are data for the rate of weight loss in an atmosphere of flowing air for the platinum family metals in the temperature range 1000 - 1400°C.

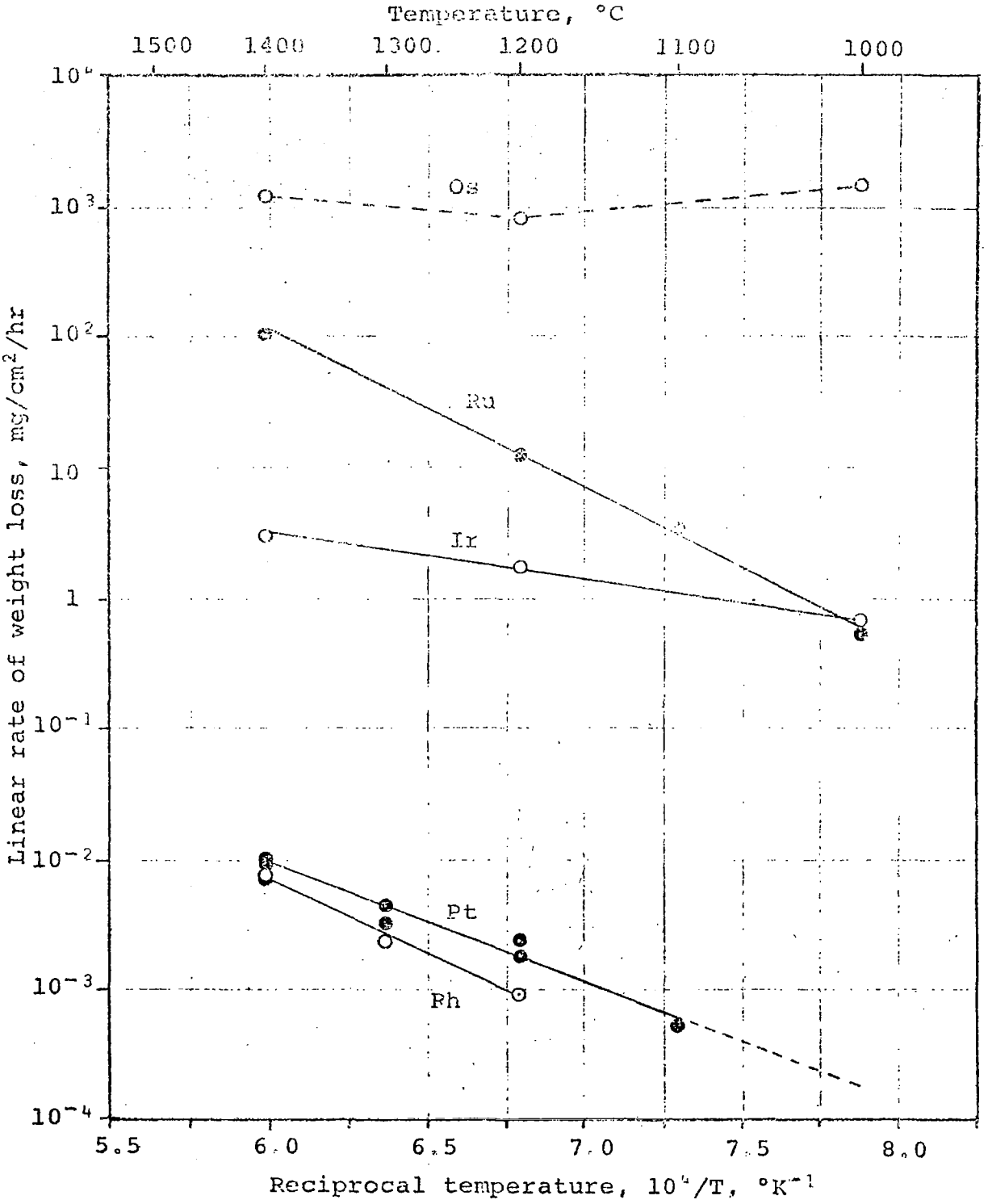

Fig. 14.- Variation with temperature of the rate of weight loss in air of the platinum-group metals. (ref. 1)

The mechanism of weight loss at these temperatures is through the formation of volatile oxides. Since these data were generated under flow conditions which might be considered "static" compared to the conditions which actually exist for the gas sampler, it is doubtful that a direct calculation of expected weight loss can be attempted using these data for as the authors point out the rate of formation of the oxide is a function of, among other variables, the oxygen partial pressure, the total pressure, and the flow rate of the gas stream in that it affects the rate at which free oxygen is able to reach the surface. Since the gas sampler operates under free molecular flow conditions, the oxidation rates will maintain their maximum values and depend only on the temperature and oxygen partial pressure. Based on these data, osmium and ruthenium were considered unacceptable materials.

2. Ductility.- Indications of the relative formability of the materials are provided by examining the results of bend tests. Although this type of data is not quantitative, it does show the gross differences between the platinum metals. Presented in Fig. 15 are data on the temperature variation of the bend ductility of the platinum family metals platinum, palladium, iridium, rhodium and ruthenium. As can be seen from these data iridium undergoes a ductile-brittle transition between 400 - 500°C. It is also apparent from these data that this transition is significantly affected by specimen surface preparation, which suggests that the apparent ductility is affected by the removal of surface stress concentrations, which

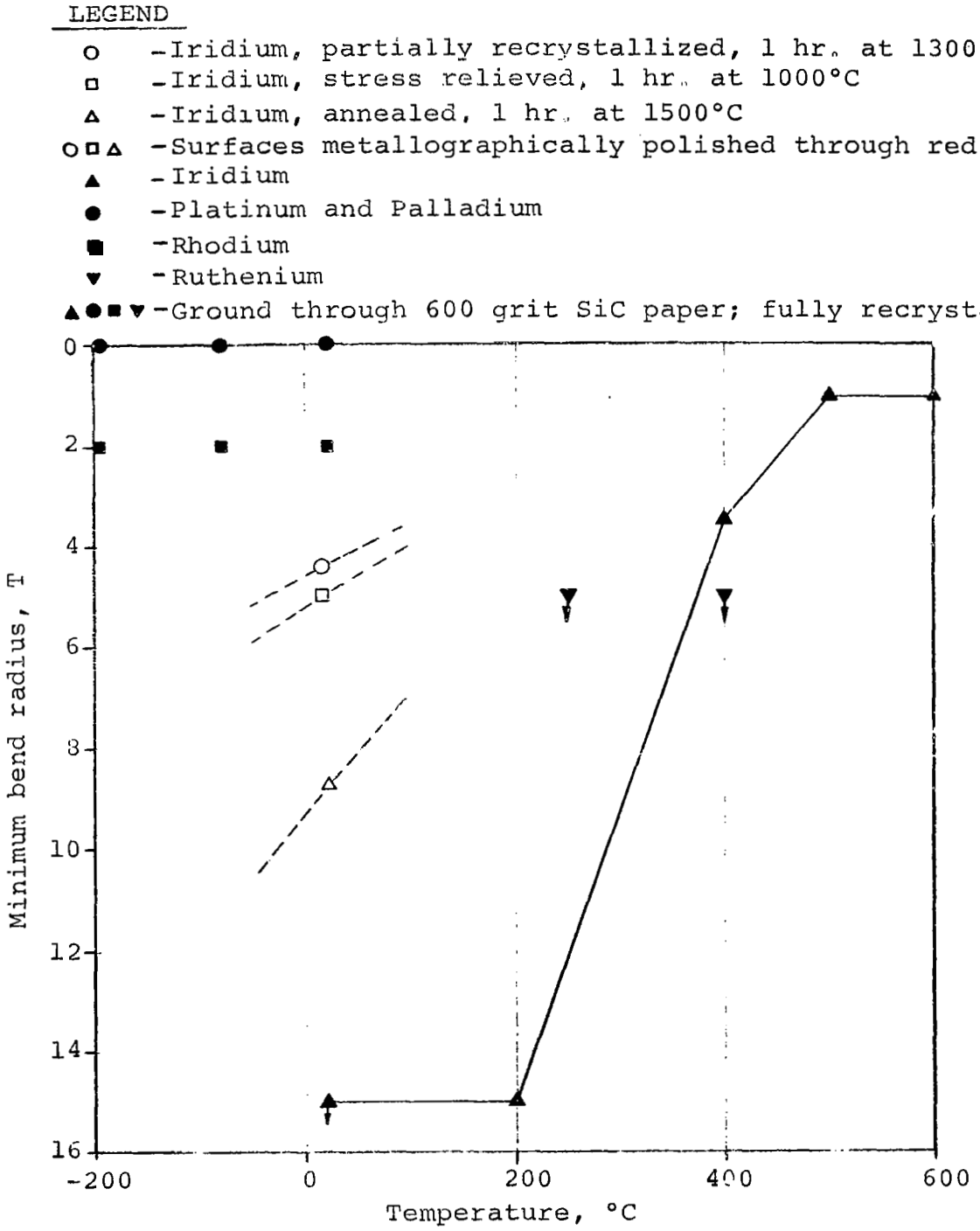

Fig. 15.- Effect of temperature on the bend ductility of annealed platinum-group metals. (ref. 1)

to some extent control the rate of fracture propagation. Additional indications of the relative ductility of the metals is also provided by examining the reduction of area and hardness of the materials. (See Figs. 1C, 2C, 3C, and 4C in Appendix C).

From an evaluation of these data, it was concluded that the necessary cold working required in the drawing operations for fabricating the tube bundle was not permissable with unalloyed rhodium or iridium.

3. Mechanical Properties.- The relative position of the components of the gas sampling system have a direct bearing on the beam intensity and hence the analysis of the atmosphere; therefore, the deformation of the components, especially the tube bundle and support webs, caused by applied dynamic stress at the operating temperature is a topic of great concern and one which is difficult to analytically predict, since the geometry and the operating conditions are quite complex. Hence, a more realistic method of evaluating the allowable deformation would be to experimentally simulate the entry conditions and observe the actual dimensional changes as a function of the sampler parameters and simulation conditions.

However; as a first approximation, the relative merits of the materials can be estimated on the basis of the conventional mechanical property data.

3.1 High temperature tensile strength.- In the evaluation of the strength of the platinum metals for this application, special attention was focused on the strength at temperature

since this was the property of prime concern. Presented in Figs. 16 and 17 are data for the tensile properties of the platinum metals as a function of temperature As can be seen, the tensile strength drops quite rapidly with temperature for each of the materials, the only one retaining any appreciable strength being iridium. Even though the apparent strength is only about 20% of its room temperature value, this rapid decrease with temperature is typical of most materials and the exact consequences are not evident from this type of data since the dynamic strength is affected by the rate at which the temperature is increased More will be said about this when discussing the short time creep characteristics.

3.2 High temperature modulus of elasticity - The eventual discussion and evaluation of the deformation of the components in the sampling system will depend upon the elastic modulus at temperature and for this reason a critical assessment of the materials was made on this basis Presented in Fig. 18 are data for the modulus of elasticity as a function of temperature for the platinum family metals as well as other refractory metals. Platinum and palladium compare favorably with commonly used construction materials, while rhodium and iridium rank among the higher strength materials; in fact they have a higher modulus than the nickel base alloys referred to as "super alloys" (these alloys having a modulus in the neighborhood of 30×10^6 psi).

Based on the combined properties of strength and modulus at temperature, iridium is the obvious choice as the superior material. However, both iridium and rhodium, because of their

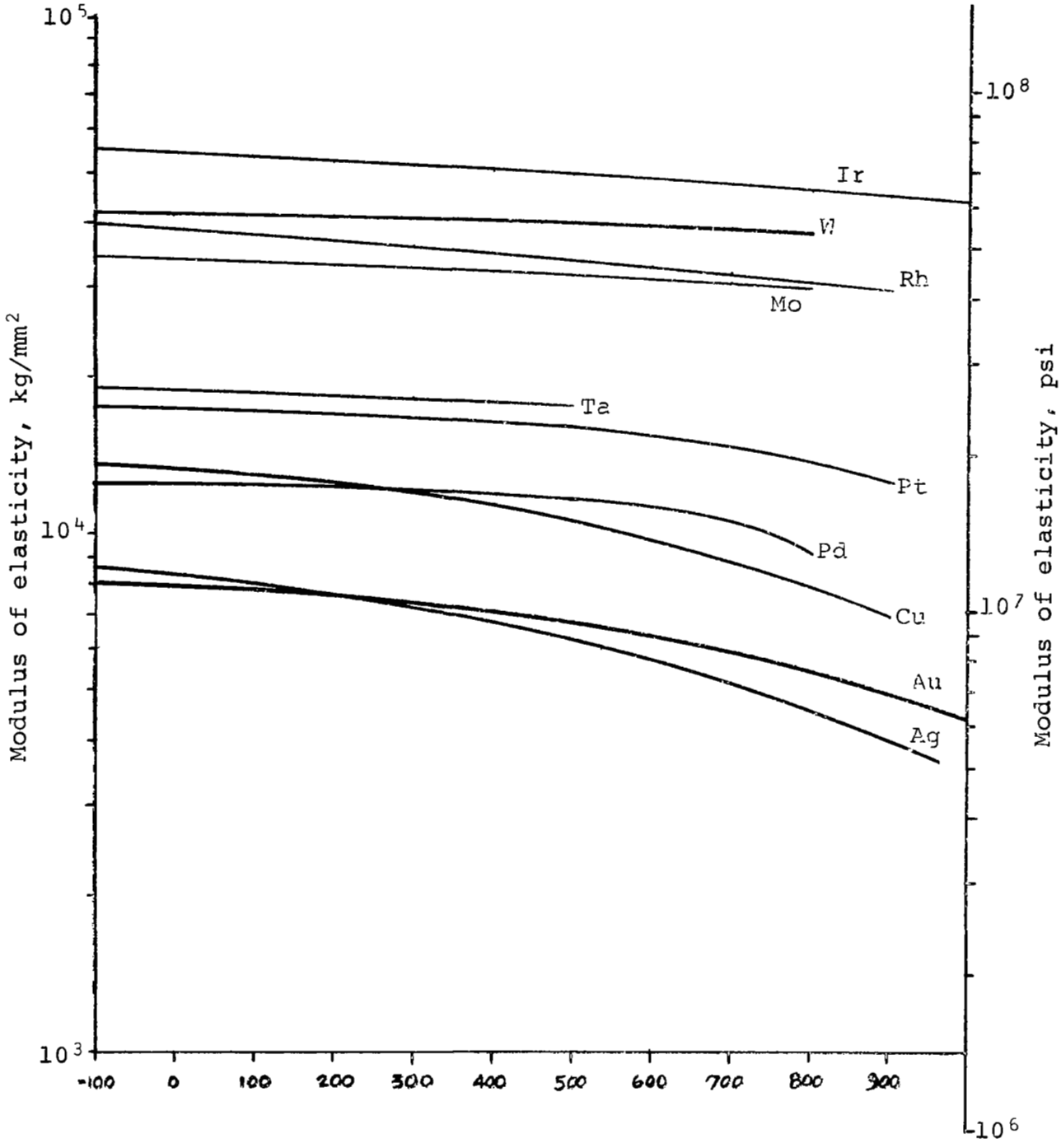

Fig. 18.- Modulus of elasticity vs temperature for the platinum family metals. (ref. 2)

low ductility at room temperature, are unacceptable for our application since the fabrication techniques to be used do not allow for hot working. These reasons, together with the fact that platinum and palladium possess hardly any strength at temperature, point to the necessity of choosing an alloy of platinum or palladium with iridium or rhodium. Since the properties of platinum and palladium are very similar, platinum was chosen over palladium because of the higher melting point, lower oxidation rate, and availability.

4. Properties Of The Alloys.- Presented in Fig. 19 are some of the physical and mechanical properties of the binary alloy systems platinum + rhodium and platinum + iridium These data are room temperature properties of the alloys in the annealed condition.

Examination of the available data concerning the properties which have been discussed led to the conclusion that the platinum-iridium alloys were superior based on the opinion that strength at the operating temperature was the most important criterion This conclusion together with consideration of all the fabrication processes involved, in the context of the program goals, was the basis for choosing the platinum -20% iridium alloy. In view of the uncertainties which existed even under these constraints, materials were also ordered to produce a pure platinum sampler.

5. High Temperature Short Time Creep.- Since the gas sampling system may be part of a high velocity, spin stabilized probe, the applied stresses are dynamic in nature and are composed of direct aerodynamic loading, inertial loading, and

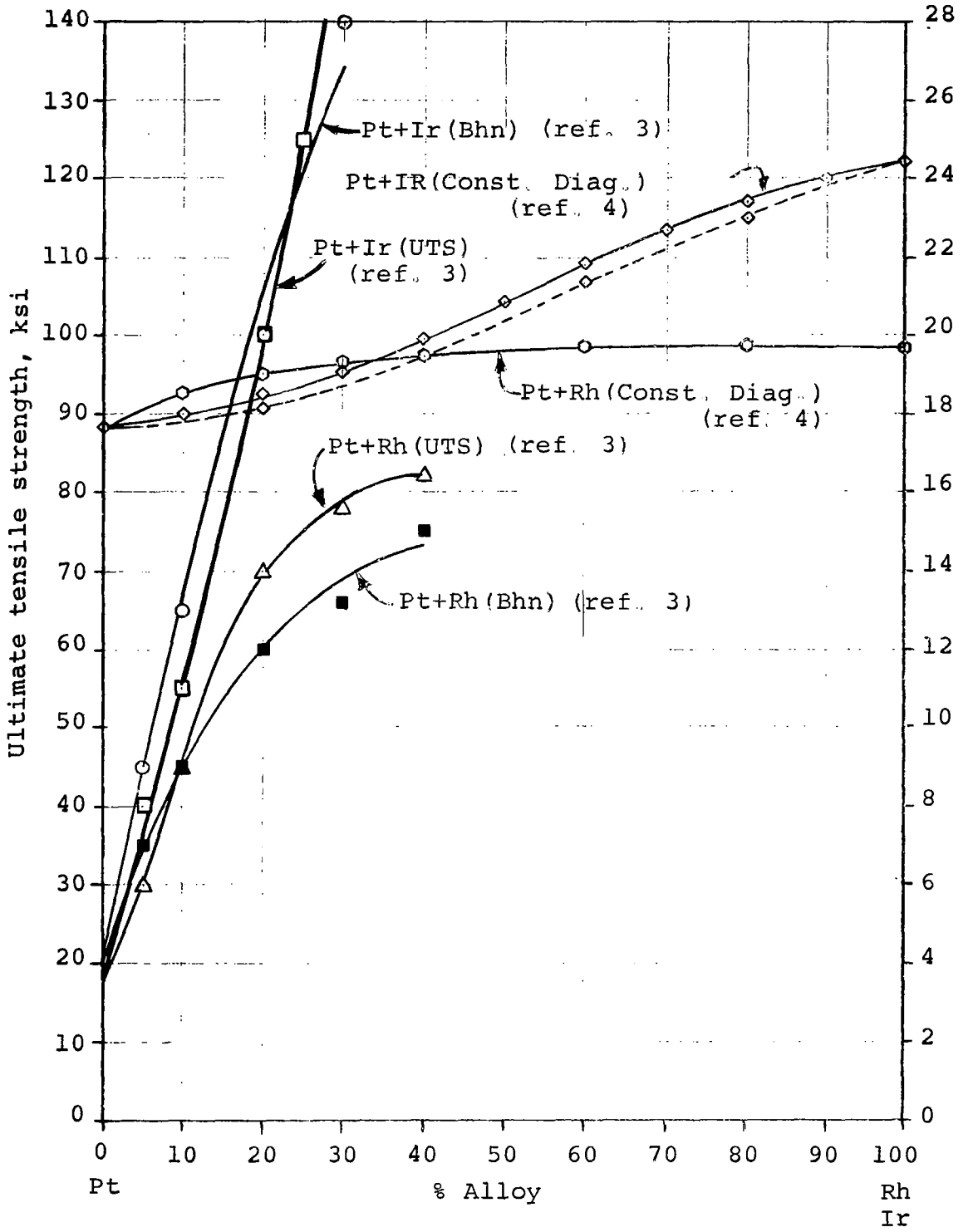

Fig. 19.- Properties of annealed platinum-rhodium and platinum-iridium alloys.

induced stresses caused by the presence of temperature gradients; the magnitude of each type of stress being dependent upon system variables such as the flux density of the incident particles, which is dependent upon the atmosphere density and the spacecraft velocity, and the nutation of the sampler, which is dependent upon the degree to which the axis of rotation of the sampler coincides with the axis of rotation of the sampler-probe combination or the sampler-probe-final stage booster combination. Because of the dynamic character of the probe the strain rates and the heating rates will both be high. Therefore, the application of available conventional data for the analysis of either the dynamic strain or the expected short-time creep is questionable.

Before presenting the actual available data on the creep and stress-rupture characteristics of the platinum metals, it is considered appropriate to indicate how the strain rate or loading rate and heating rate effect the measured material strength and deformation. Although data for the materials in question tested under appropriate conditions were not available, it can be inferred that these data are necessary before a meaningful stress analysis can be attempted.

As an indication of the effect of strain rate on the strength of materials, Fig. 20 is a plot of strength vs strain rate for 2024-T4 aluminum alloy at 600°F. Added to this effect of strength vs strain rate is the fact that higher heating rates produce higher yield temperatures*. A comparison between

---

*The definition of yield temperature is that temperature at which 0.2% offset plastic elongation occurs in a specimen under a given load and heating rate.

Tensile strength of bare 2024 T4 aluminum alloy sheet at 600°F. Specimens were heated to test temperature within 10 sec. and held 10 min. before testing

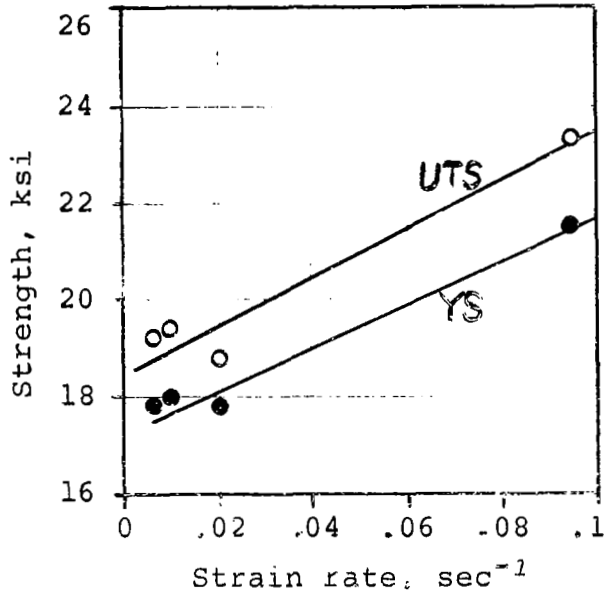

Fig. 20.- Strength vs strain rate for 2024-T4 aluminum (ref.5)

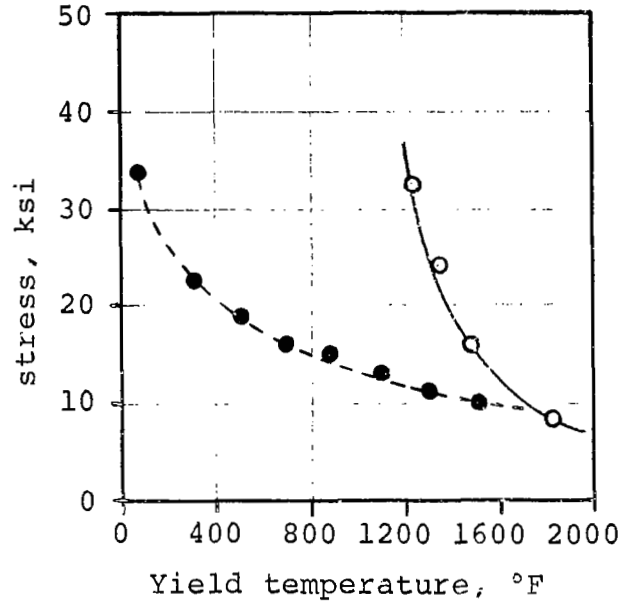

Fig. 21.- Comparison between short-time high-temperature and high-heating rate yield strength for annealed 18-8 stainless steel. Heating rate was 400°F per sec (ref.5)

● short-time high-temp tests

o high-heating rate tests

short time high temperature tests and high heating rate tests are shown in Fig. 21. From these data it is evident that the rate at which the stress and heating occur is of prime importance but at the present time these rates are undefined since they depend, to a large extent, on the method chosen for stabilization and the systems approach for establishing the entry of the probe into the planetary atmosphere.

The conventional creep and stress-rupture tests are concerned with determining the life characteristics of materials. In these conventional tests, the time-deformation characteristics are determined under constant load and temperature conditions, the load being applied after the specimen has been stabilized at the test temperature. These tests are of long duration (tens to the thousands of hours) and cannot be used for short-time rapid-heating analysis (typical creep and stress-rupture data for some of the platinum metals and alloys are presented in Figs. 5C and 6C). Since we are interested in the creep rates for short duration (of the order of 10 sec), it is doubtful that an extrapolation of conventional data is either valid or meaningful.

To illustrate the importance of the time interval over which the material is required to operate within the desired limits of creep and strain, the following data for the dynamic analysis of type 302 stainless steel is presented. The specimens were loaded at room temperature, heated to the test temperature at 125°F per sec and then maintained at the test temperature while time-deformation data was recorded. Presented

in Fig. 22 is a plot of total deformation vs time at 1800°F for various values of applied stress. This same data, after subtracting the elongation due to thermal expansion and elastic deformation, are presented in Fig. 23 and show the plastic deformation vs time for various values of applied stress. Another way of presenting this data is the isochronous stress-strain curve presented in Fig. 24. From these data it can be seen that relatively high values of stress can be tolerated if the time interval is short. In fact, for time intervals of the order of 10 sec, stress levels approaching the "static" room temperature yield strength can be tolerated even at elevated temperatures without producing excessive deformation (≈2%). For example, shown in Fig. 25 is a plot of stress vs temperature to produce a total deformation of 3% in a time interval of 0.5 min; the room temperature yield strength (.2% offset) is 43,400 psi.

For the Mars mission, the stress produced by aerodynamic loading is of minor importance because of the low density of the atmosphere; the most serious problems will be associated with dynamic inertial forces and temperature induced stress. However; by the proper design of balance of the probe to reduce the amplitude and frequency of the nutuation, the dynamic inertial stresses are minimized and by keeping the thermal mass of the critical components low the temperature gradients can be minimized. Therefore, the problems associated with creep and strength do not appear to be overwhelming.

6. Availability And Cost.- Most of the platinum metals and alloys are available in either bulk form or fabricated into wire, sheet, or tubing in a variety of sizes to fit most design

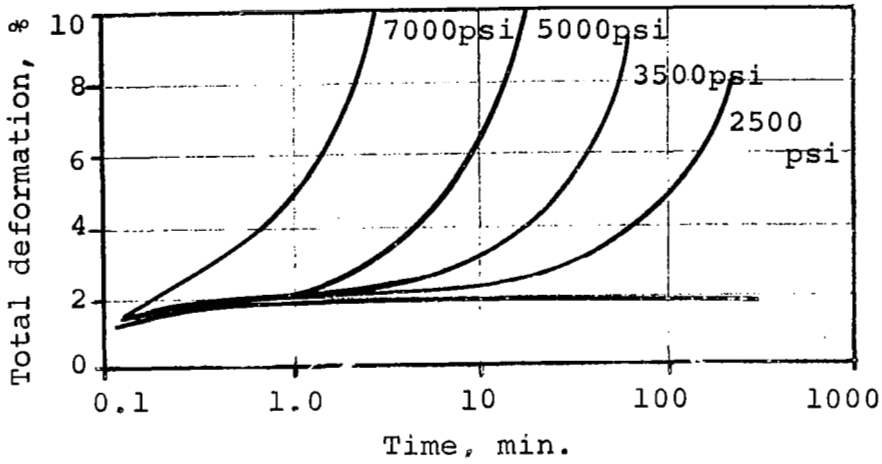

Fig. 22.- Time-deformation curves for type 302 stainless sheet tested at 1800°F with a heating rate of 125°F/sec. (ref. 5)

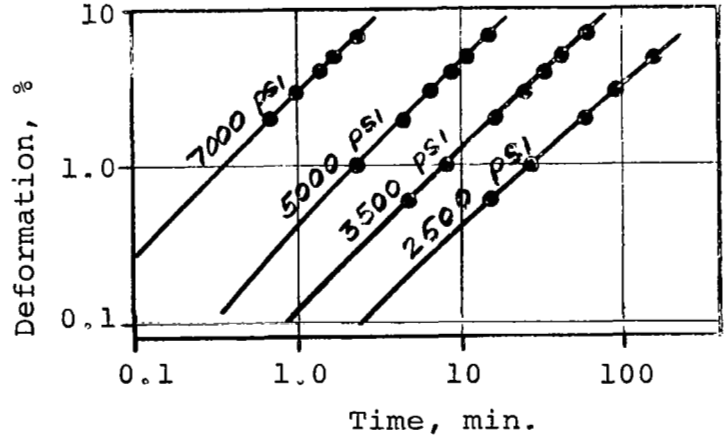

Fig. 23.- Time-deformation curves for type 302 stainless sheet tested at 1800°F. Data is the same as Fig.22 except that thermal expansion and elastic deformation have been subtracted. (ref. 5)

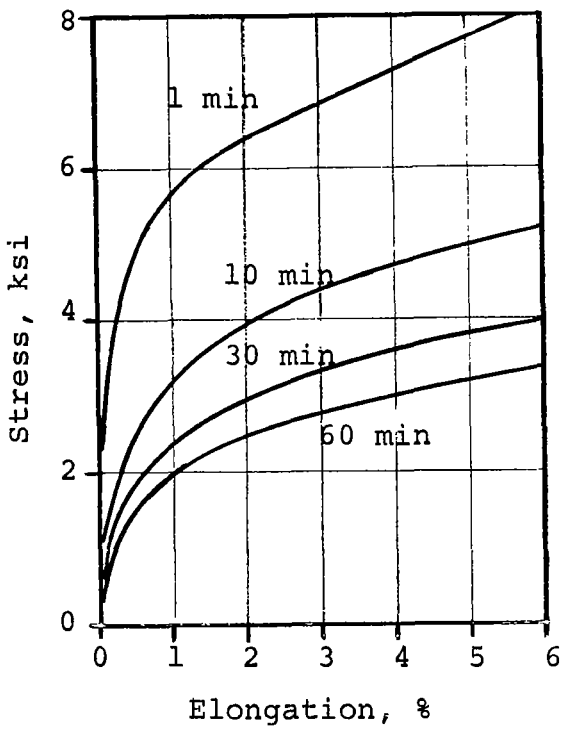

Fig. 24.- Constant-time stress-elongation curves for type 302 stainless tested at 1800°F. (ref. 5)

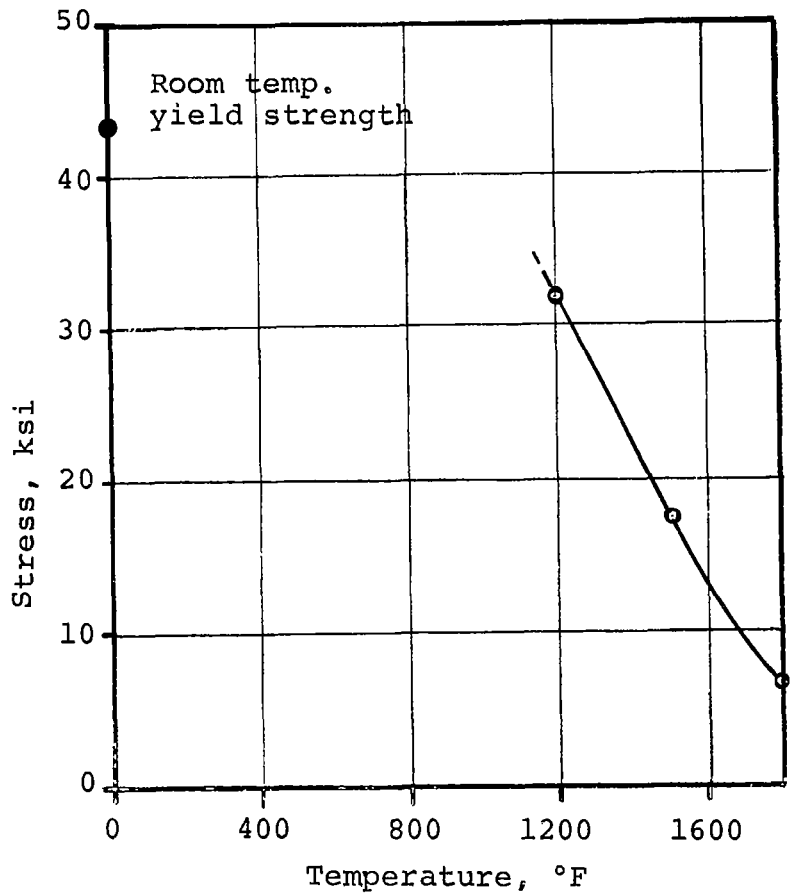

Fig. 25.- Stress vs temperature to produce a 3% total deformation in 0.5 min. (ref 5)

applications. The limits imposed on the alloy compositions of fabricated products other than bulk form are controlled by the ability to cold work the alloy.

The basic cost of the metals and alloys are approximately $3.50 per gram. However; as is generally the case for any material, when purchasing fabricated components in small quantities, the tooling and fabrication costs are so high that the basic material costs are insignificant compared to the total cost. Therefore, the unique advantages of the platinum metals are being exploited and their usage in industrial applications has become commonplace.

B. Tube Bundle Fabrication Techniques

Even before the exact geometrical dimensions of the sampler were defined, it was known that the final design would include a number of tubes arranged in a symmetrical, close-packed array such that the geometrical transparency was high. It was anticipated also that the cross-sectional area of the individual tubes would be required to be as small as practicable. To satisfy both of these conditions, one must select a small diameter, thin wall tube. The smallest bore tube made by most commercial suppliers is around .010 inches diameter, except for glass and ceramics; this size was roughly three times larger than what we had chosen as a desireable goal. Therefore, the method chosen would either have to start with this size and reduce it or provide some independent approach to fabricate the structure. The following methods were considered as possibilities:

1. Tube Swaging.- This method was patterned after the ideas of Ad'yasevich and Antonenko (ref. 8), who described the fabrication of a bundle of glass capillaries with bore diameters as small as 10-60μ with geometric transparencies up to 80%. Since glass was acceptable only as a last resort, it was considered whether this same technique might not also be feasible for the fabrication of a similar structure using some of the more ductile metals such as copper, gold, or platinum. Even though the technique seemed possible, the main drawback was the necessity of performing the drawing operation hot. This meant the development of specialized tools and techniques which hardly seemed warranted under this program.

2. Power Grid Technique.- In this approach, wires plated with the material of which the grid is to be made are inserted into a tube and the entire assembly swage-drawn to the desired size. The core wires are then etched out leaving an array of thin-walled tubes inside a thicker wall outer tube. Since this technique involves no hot working and produces the desired array, it was considered a prime candidate.

3. High Pressure Extrusion.- A similar technique to the power grid method produces the desired array by first machining a scaled up version of the finished product out of bulk stock. The core is then filled with a material of near identical mechanical properties; especially important are likeness in ductility and work hardening characteristics. The solid slug is then hydrostatically extruded through a die or set of dies to produce the desired size. The core material is then re-

moved leaving the desired structure. The main disadvantage of this technique is that the initial machining operations from bulk stock require a huge investiment in material alone even though a large percentage is retrievable. Since this process had never been tried with platinum, it would have required a few trial runs making the total investiment a large fraction of the available budget and since the scrap value could not be converted rapidly, the idea could not be used even though it had considerable merit.

4. Honeycomb Core.- Soon after starting the evaluation of tube bundle fabrication techniques it was discovered that the only close-packed structure which could properly produce the required nearly circular periphery was a hexagonal core. As a consequence, it was considered that an appropriate technique might be found among those used in the fabrication of honeycomb composites. However, the appropriate size was not even approached so this technique was dropped in favor of one of the others without completely exploring the possibilities.

The conclusion of this phase of the program was that the power grid technique had the greatest potential and was limited only because the materials we had chosen had not been tried. However, hexagonal structures had been fabricated from copper, stainless steel, and tantalum. In fact examples of copper structures were examined which had ideal geometries and also had geometrical transparencies greater than was expected possible. Shown in Fig. 26 is a photograph of a typical copper grid. Further discussions with the manufacturer revealed no apparent difficulties and there was no reluctance on their part to contract to produce the required product.

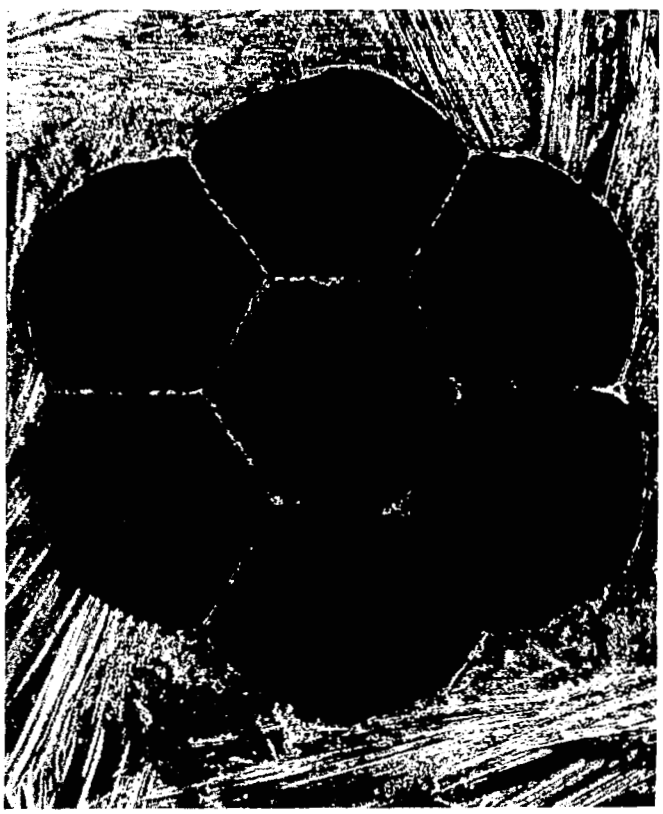

Fig. 26
Photomicrograph of typical
copper grid structure
(97X)

C. Sampler Design

Concurrent with the formulation of the materials and fabrication requirements, the evaluation of the theoretical performance characteristics of the sampling system had advanced to the point where prototype design drawings could be initiated. The optimum dimensions were established by balancing the theoretical performance with the fabrication capabilities of existing equipment consistent with the program objective of providing a sampler for the deepest penetration into the atmosphere of Mars. These considerations called for a length-to-diameter ratio of four with an individual tube diameter of 5×10^{-3} cm.

1. Tube Bundle.- The total number of tubes in the tube bundle control the amount of flux which is available to the ion source but do not effect the signal-to-noise ratio because the beams are non-interacting beyond the exit of sampler tube bundle in the region of interest. Since there was no data available on the size or the ionization and extraction efficiency for the ion source to be used, two tube bundle geometries were chosen for fabrication containing seven and nineteen tubes respectively. Deviations from these numbers of tubes greatly affect the cross-sectional geometry of the individual tubes.

It is desireable to keep the exterior conical angle of the tube bundle as small as possible since the high velocity atmospheric flux is incident on the surface and directly controls its temperature. However, the overall length of the tube bundle is fixed since it is controlled by the L/D of the in-

dividual tubes (chosen as 4) and if the exterior angle is made too small the thickness of the outer tube surrounding the tube bundle becomes impractically thin at the aft end. Since this dimension controls the width of the support webs, the minimum conical half angle considered practicable for these tube bundle desings was 30°.

2. Skimmer.- The skimmer provides a dual function in the gas sampler. 1) It serves as a collimator by limiting the solid angle between the exit of the sampler tubes and the entrance to the ion source; this solid angle is chosen to strip off as much of the scattered flux as possible without greatly reducing the amount of primary flux. This is possible because the angular distributions of the scattered and unscattered fluxes are somewhat inverse in character; near the tube axis, the unscattered flux is maximized and the scattered flux is minimized. As the solid angle is increased, the rate of change of the unscattered flux decreases and that of the scattered flux increases. 2) It provides an annular exhaust duct for the removal of that portion of the total flux which is stripped away. In performing this function, it also prevents exterior atmospheric gas from entering the region of the primary beam. The shape and size of the skimmer is controlled by a proper balance between these two functions which it serves.

3. Pumping Apertures.- That the annular, conical shaped ducts between either the tube bundle and the skimmer or adjacent skimmers actually serve as "pumping" apertures is because the entrycraft has a directed velocity which is much

greater than the mean molecular speed. The use of "pump" is meant to reduce the probability to nearly zero that a molecule once removed from the primary beam by a skimmer will again be found in the region of the primary beam. Consider the following sketch of one of the pumping apertures:

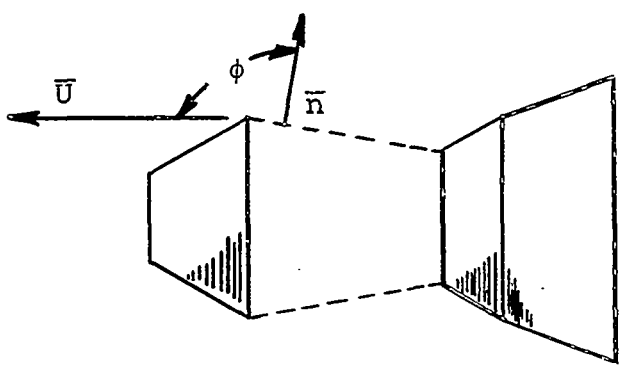

Only those molecules in the exterior atmosphere which collide with, and thus pass through, the right circular conical surface indicated by the dotted lines can enter the region of the primary beam; all others are scattered away. If an element of this surface represented by a unit vector $\bar{n}$ is inclined at an angle ϕ with respect to the entrycraft velocity $\bar{U}$, the relationship between the collision frequency with this element of surface and the angle ϕ is shown in Fig. 27. This data was generated for the Martian atmosphere near the maximum density to be encountered (10^{15} cm^{-3}) and with a typical entrycraft velocity (5×10^5 cm/sec). For angles of ϕ greater than 100°, the number of molecules entering the region of the primary beam from the outside atmosphere are neglegible compared with the number entering the front of the sampler (in this particular example the collision frequency with the front surface of

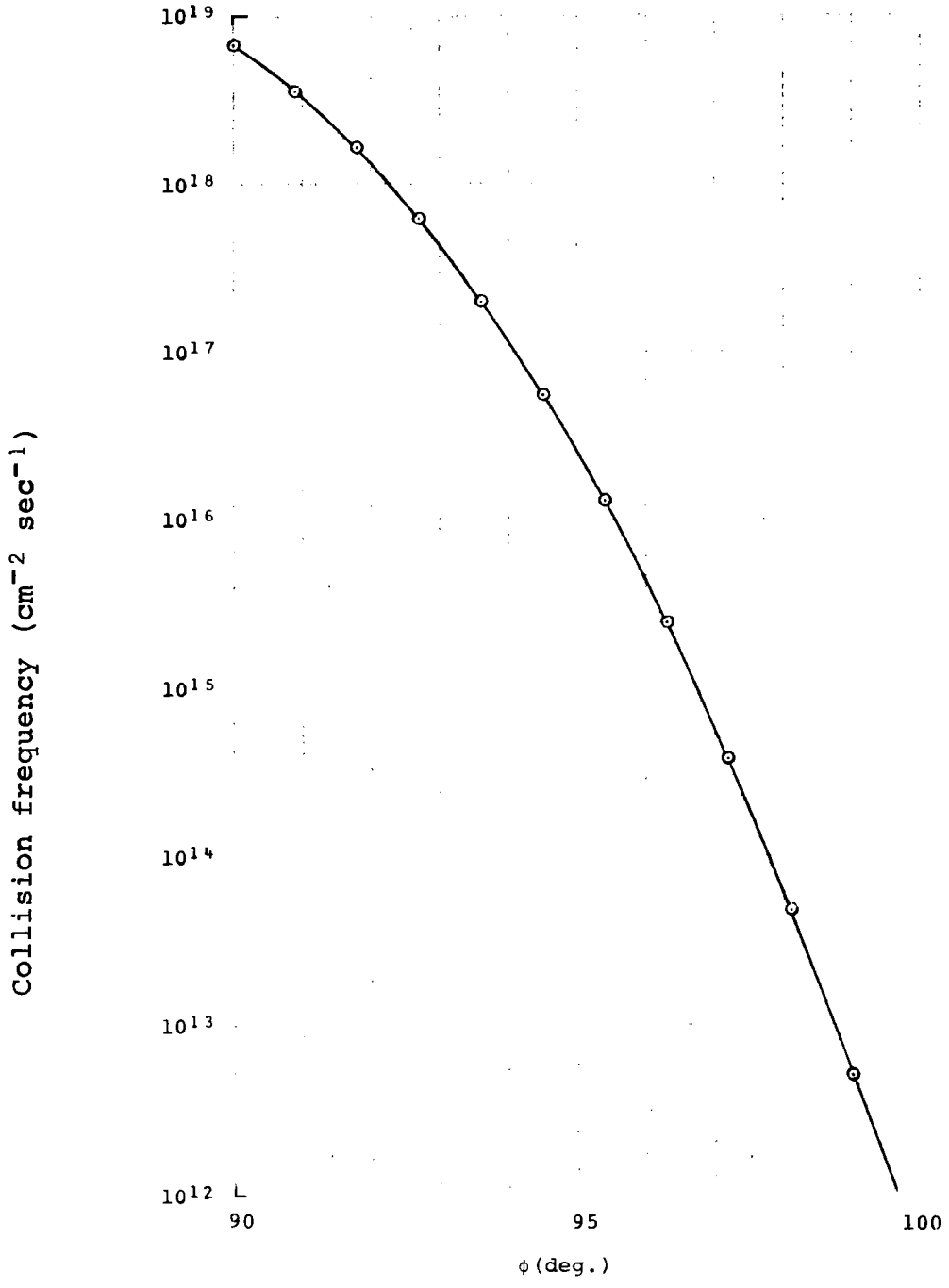

Fig. 27

Collision frequency vs angle (ϕ) between the velocity vector and the surface normal

sampler is 5 x 10^{20} cm^{-2} sec^{-1}). Thus the probability of the molecules crossing this surface from the inside being scattered back is also quite small so that in effect they are "pumped" since once they pass through this surface they are scattered away from the sampler by collision with the outside gas molecules or the front surface of the skimmer.

4. Support Structure.- The support structure was chosen to rigidly, and precisely position the components of the sampler. A simple but yet effective method was selected which produced as little obstruction as possible to the flow of gas through the pumping apertures; these webs are fabricated from iridium ribbon and are fastened to the individual components in slots machined in them.

Shown in Fig. 28 is a dimensioned sketch of the entire assembly.

D. Fabrication Of The Sampler

1. Surveys Of Available Facilities.- After establishing the program goals, it was possible to initiate surveys of commercially available facilities in an attempt to locate existing companies which were capable of performing the individual tasks requiring specialized techniques. The construction of the gas sampling system required assessing compentence in four areas: 1) fabrication of platinum and platinum-iridium alloy tubing and ribbon of appropriate dimensions 2) plating small diameter wires (≈.005 inches) with a uniform, non-porous film of platinum or platinum-iridium alloy 3) equipment capable of performing

Dimensions in inches

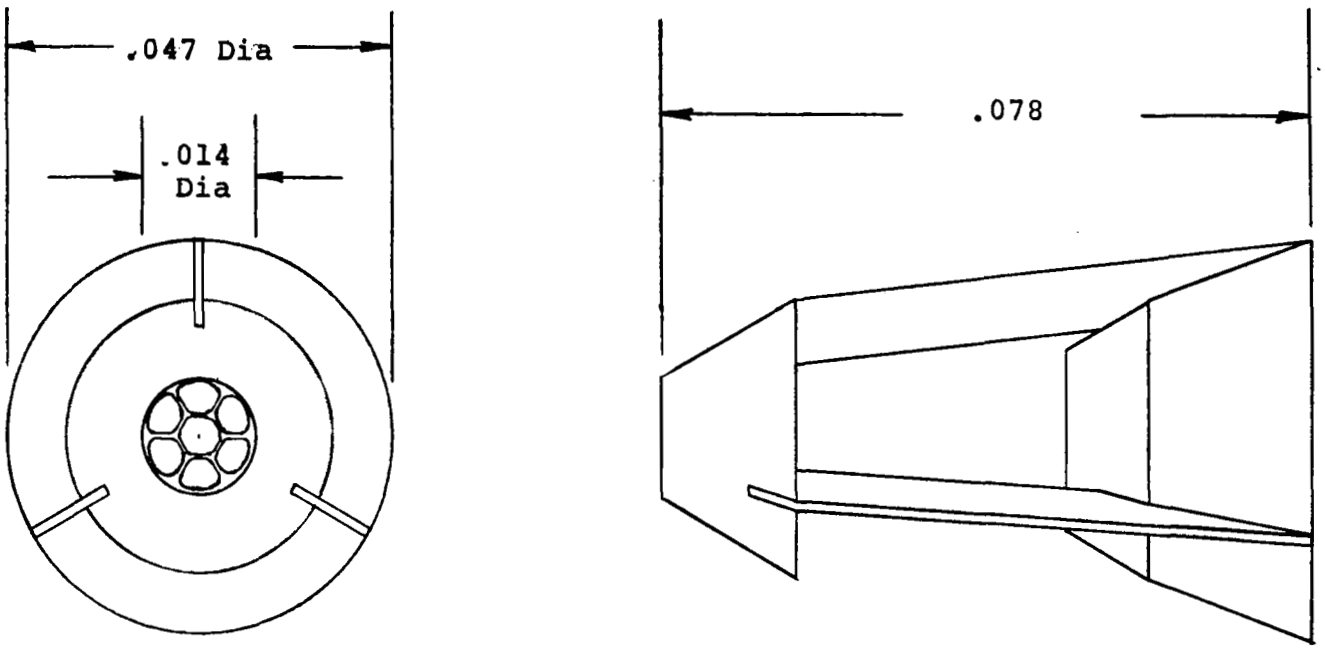

Fig. 28
Sketch of Martian gas sampling system
Scale: 50/1

the necessary machining operations on extremely small and fragile parts and 4) assembly of the individual components without introducing a prohibative amount of warpage or contamination.

1.1 Tube bundle fabricators.- Three suppliers were evaluated and Lancer Industries, Inc. was selected based on discussions with their technical staff and our own examination of the samples supplied to us. Some of the criteria used for the comparison of the products were 1) geometrical similarities such as core size, configuration and geometrical transparency between what had been produced and what we required 2) adhesion of the individual tubes within the core by examination of photomicrographs of the interface 3) delivery times and cost. Even though none of the companies had actual experience with the platinum metals, it was concluded that the similarities between the materials to be used and those which had been used successfully provided a high confidence level of success.

1.2 Plating facilities.-

1.2.1 Commercial facilities.- A limited number of companies maintain facilities for plating the platinum family metals with the exception of pure platinum and rhodium. No commercial facilities were found for plating platinum-iridium alloys. The only method available commercially was that of physical vapor deposition of a platinum-iridium composite formed by the codeposition of the two metals. The composition of the deposit is controlled by monitoring the

evaporation rate from the individual sources. This method was undesireable because of the inherent difficulties in accurately controlling the composition and thickness of the plated film and because of the high cost. However, the main objection to the process was that the film produced was not an alloy but simply a composite of platinum and iridium, the properties of which were unknown. Therefore, the alternative was to investigate the possibility of performing the plating operations in the laboratory. Two methods of depositing platinum-iridium alloys were found in the published literature; one used chemical vapor deposition techniques and the other electrodeposition of the alloy from chemical compounds in solution.

1.2.2 Chemical vapor deposition.- The description of the general techniques used in chemical vapor deposition as well as the specific requirements necessary for the preparation of the plating compounds for the platinum metals are covered by Powell (ref. 9). Thick, adherent deposits are possible employing the thermal decomposition of carbonyl chlorides at a pressure of 0.01 to 0.02 Torr, a carbonyl chloride temperature of 100 to 120°C, and a specimen temperature of 600°C. The possible formation of nonadherent, crystalline deposits caused by incomplete separation of halogen from the metal atom can be avoided by hydrogen reduction; using separate gas streams of hydrogen and metal compound in a CO carrier which are mixed at the sample. This hydrogen reduction produces a smooth, adherent deposit at sample temperatures as low as 125°C.

Although the preparation of platinum-iridium alloys are not specifically described, it is considered feasible since both platinum and iridium can be deposited from carbonyl chlorides at a surface whose temperature is relatively high (600°C) thereby increasing the probability of a diffused coating at the substrate.

1.2.3 Electrodeposition.- The electrodeposition of iridium has been reported by MacNamara (ref. 10), Tyrrell (ref. 11), and Withers and Ritt (ref. 12); the first two authors used aqueous solutions of chloriridic acid and bromoiridic acid respectively and the latter used a molten cyanide salt complex. In an additional paper by Tyrrell (ref. 13), he describes the electrodeposition of various compositions of platinum-iridium alloys using an aqueous solution containing both bromoiridic and bromoplatinic acids. X-ray diffraction analysis indicated that the codeposited films were single-phase alloys rather than mixtures of the metals.

Since this latter process provided a rather simple solution to our needs and required very little refinement as far as technique was concerned, it was decided to produce the required platinum-20% iridium alloy deposits on the copper core material in the laboratory.

However; during subsequent investigation of the authors' activities, it was discovered that a research group, General Technologies Corp., was willing to do the work for us. The specifications called for a uniform, adherent, and non-porous

electrodeposit of platinum-20% iridium alloy with a thickness of .00025 inches on 34 gauge OFHC copper wire. These plated wires formed the core of the tube bundles to be fabricated.

1.3 Material suppliers.- The platinum and platinum-20% iridium alloy tubes, which were to be used for the exterior of the tube bundles, with the appropriate dimensions for both the seven and nineteen tube array were available from a number of sources; the final selection of the vendor (Englehard Inc.) was made based on delivery times since the delivery schedules were quite long and ranged from 30-90 days. No difficulty was experienced in locating other materials required such as platinum alloy braze and ribbon for the support webs.

Therefore, all materials and fabrication processes required for completing the tube bundles were arranged and plans were made so that the materials would arrive in the proper sequence.

1.4 Machining facilities.- The selection of a local machine shop with the appropriate skills and machinery was based on an awareness of the problem and exhibited performance. The final selection was Clendenning Smith, Inc. The techniques to be used were a combination of electrical discharge machining and ultrasonic machining, whichever was more suitable for the particular part in question.

2. Assembly.- Since the cleanliness of the entire sampler and alignment of the individual components were of prime concern during the assembly operations, the method of attaching the components together would of necessity have to be completed either in a vacuum or inert gas atmosphere and utilize a method

which avoided localized heating of the components whereby warpage of the components would result and cause misalignment of the skimmers with respect to the axis of the tube bundle. The two selected methods which provided the necessary control of both of these parameters were electron beam welding and vacuum or inert gas brazing.

2.1 Electron beam welding.- The limiting requirements for the use of electron beam welding are the physical size of the components and their thermal mass. The weld area must be larger than the focused beam size and be visibly accessable from the exterior. The thermal mass must be sufficiently large to allow a pulsed beam welding operation without causing severe localized bulk heating. This is possible only if the thickness of the parts are greater than the depth of the thermal gradients, which are capable of producing thermal distortion, produced during the surface welding operation. This is not a severe restriction since the minimum weld penetration to produce attachment will be used; the expected stress levels at the weld joints being quite small. However, the physical size and accessability are such as to render a definite conclusion questionable. Therefore, the means for an alternate approach were prepared in case electron beam welding was not found to be feasible.

2.2 Vacuum brazing.- The necessary hardware for vacuum brazing the assembly had already been provided since an induction heated tubular furnace was to be used for annealing the tube bundle during swaging operations and for evaluating the temperature limit of geometrical stability. This method

of attachment has the advantage that the entire assembly is heated uniformly and the probability of thermal distorition is low since all the parts are constructed of identical material and have been stress relieved through repeated annealing cycles during the swaging and vacuum degassing operations. The braze alloy is applied as a slurry of fine powder suspended in an organic binder, which is completely evaporated before reaching the melting point of the braze alloy.

Both of these assembly methods produce a completed sampler which is devoid of contamination; a property which is considered essential since the surface impact of high velocity gas molecules would inject spurious surface desorbed species into the beam which would confuse the analyses of both the operational characteristics of the sampler as well as the mass spectrometric determination of the atmosphere constituents.

CHANGE OF PROGRAM SCOPE

The results of the computed performance of the sampling system provided sufficient confidence in the proposed method that experimental evaluation was desireable However laboratory experiments which provided the necessary parameters for simulation of the appropriate entry conditions were questionable since the analysis was desired in as short a time as possible. Therefore, the feasibility of evaluating the performance utilizing flight testing in the Earth atmosphere was established. This approach was consistent with the goal of having flight qualified the design for material performance as well as having established an experimental evaluation of the gas sampling method. Therefore, the program was re-directed from the goal of providing a sampler for the Martian atmosphere to one which would provide the greatest amount of information for sampler performance evaluation in the Earth atmosphere.

Since one of the unique predictions of this investigation was the attenuation of the primary molecular flux by the diffuse gas generated within the sampler tubes, the design of a flight experiment to verify this decrease of signal-to-noise ratio at some moderate density would substantiate the theoretical predictions without forcing the requirements on material performance to their limits. The geometry of this sampler was specified so that internal tube gas loading effects would occur at around 90 km in the Earth atmosphere. Detailed design considerations were based on the analyses which had been performed on the Martian sampler and the final configuration chosen was as shown

in Fig. 29. The skimmer and collimator geometry and dimensions were chosen so that a measurable amount of flux would be transmitted at angles of attack up to 5°; however predicted performance at non-zero angle of attack is not possible on a quantitative basis with the theoretical development at the present time. The zero angle-of-attack performance of this sampler (X_M = 4, U = 4 km/sec, and S = 6.75) was investigated over a range of atmospheric densities. The total primary flux transmitted through the sampler is presented in Fig. 30, the signal-to-noise ratio in Fig. 31, the dimensionless mean free path (inside the inlet tube) in Fig. 32, and the sampler tube temperature in Fig. 33. Each of these parameters are presented as functions of density and altitude in the Earth atmosphere.

Three gas samplers were fabricated for performance evaluation testing. The conical sections were fabricated from platinum and the support webs were fabricated from a platinum -20% iridium alloy. The assembly of the components was accomplished by electron beam welding. Shown in Fig. 34 are photographs of the completed gas sampler.

Dimensions in inches

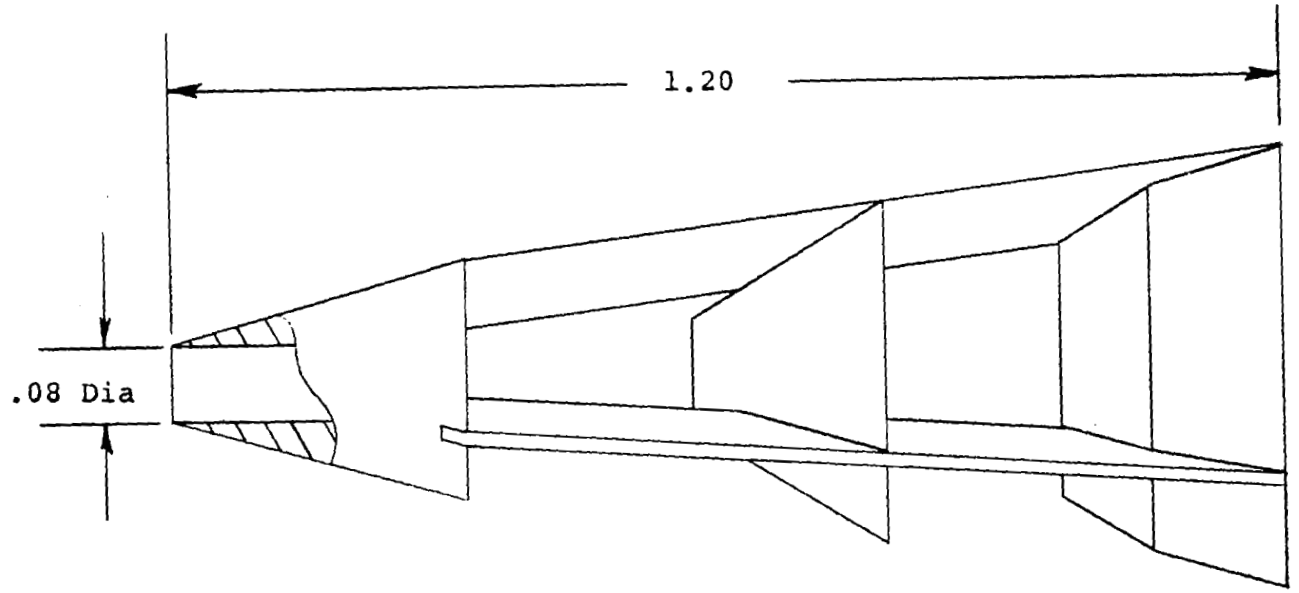

Fig. 29

Sketch of Earth gas sampling system

Scale: 5/1

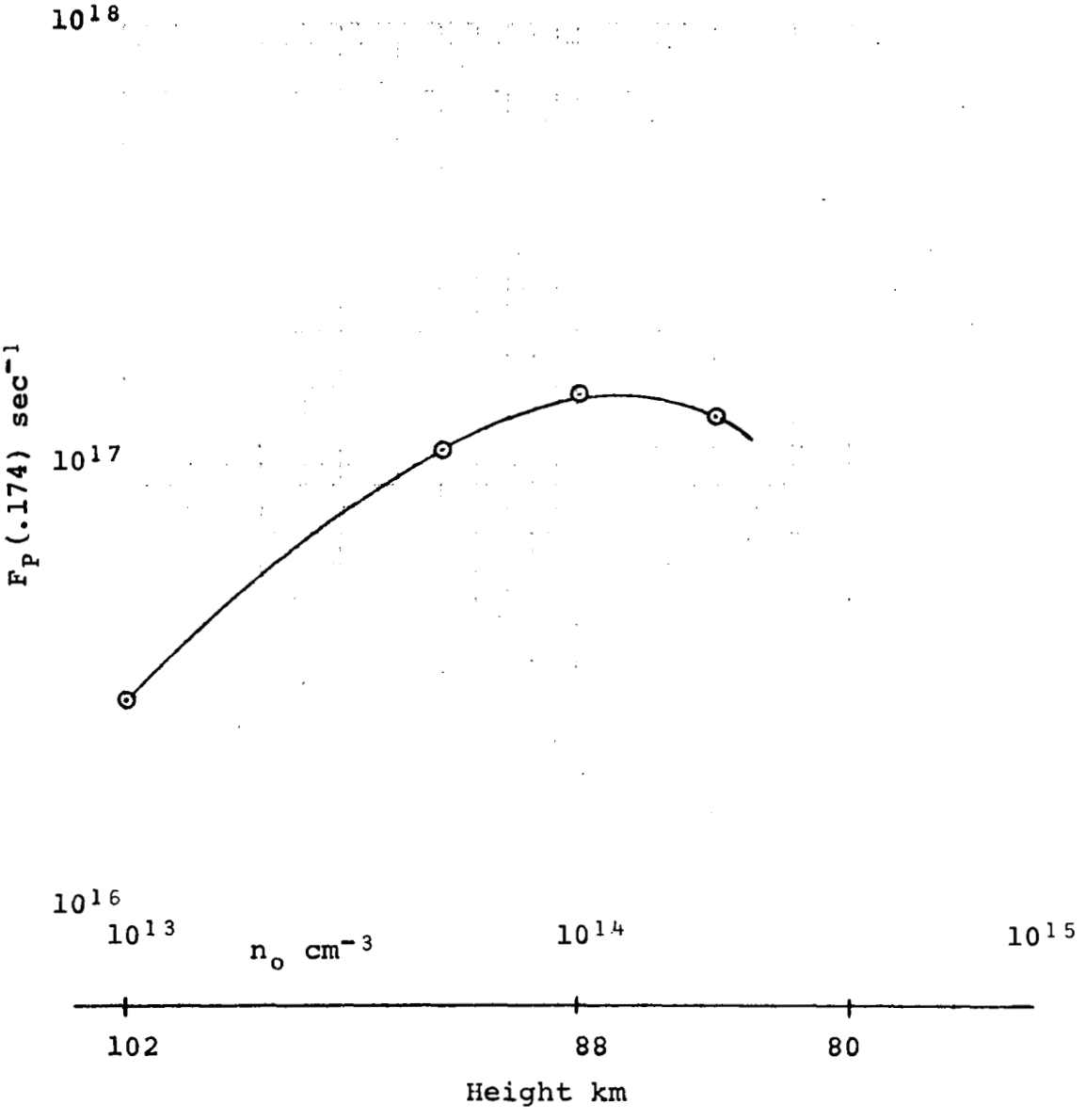

Fig. 30

Primary flux continued in a solid angle with a plane half angle of .174 rad. vs. number density and altitude.

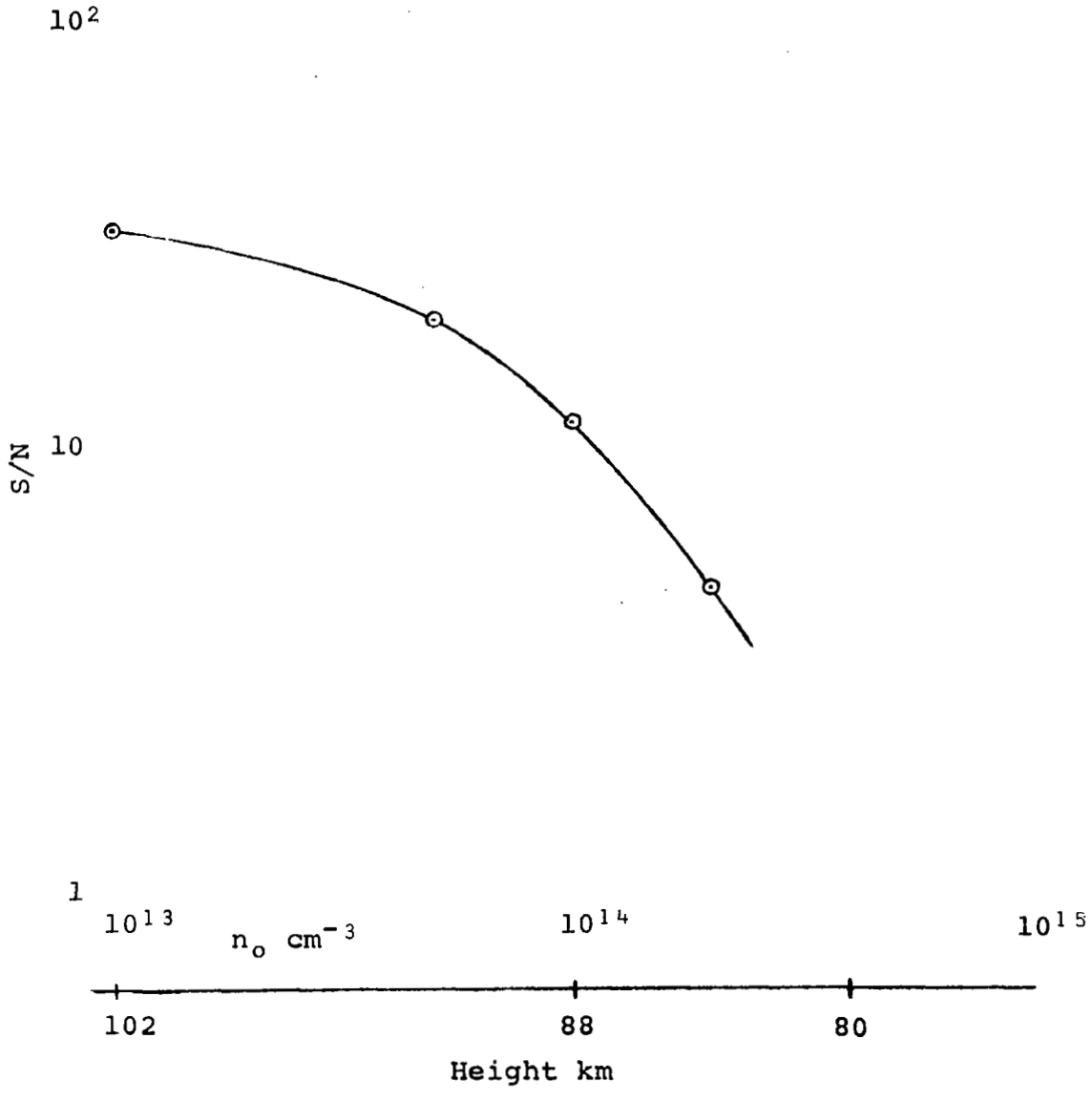

Fig. 31

Signal-to-noise ratio vs. number density and altitude.

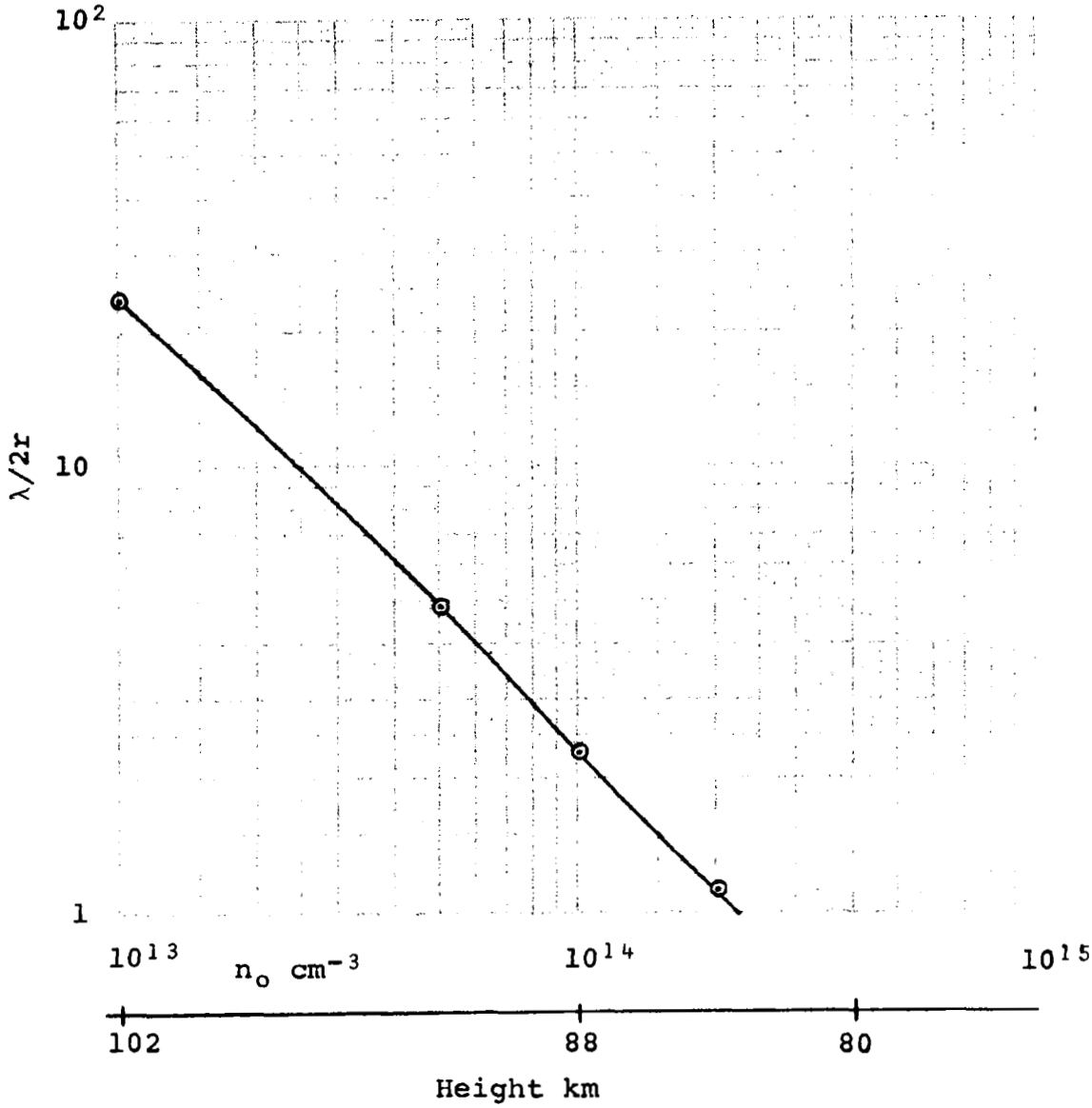

Fig. 32

Dimensionless mean free path vs. number density and altitude.

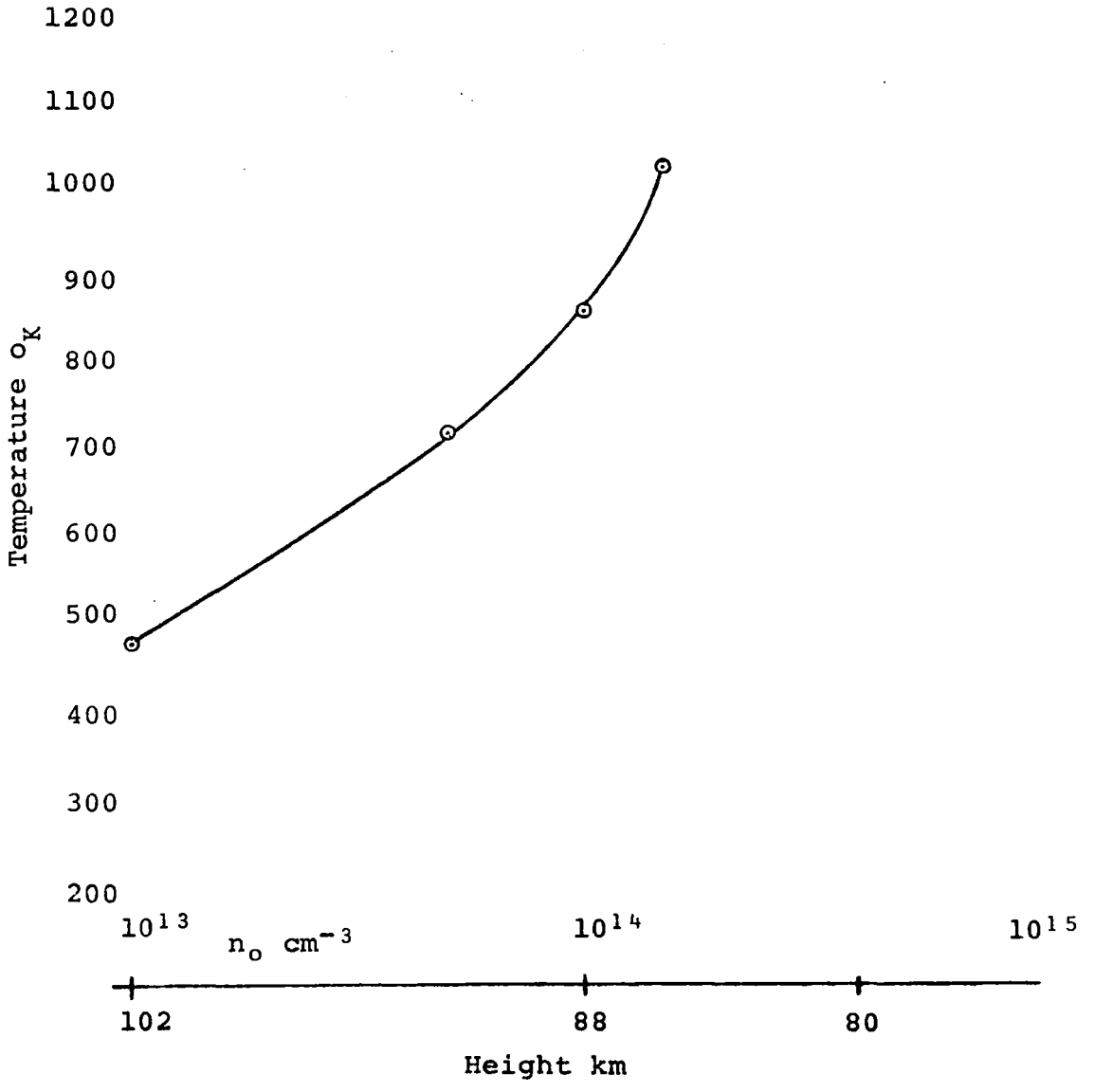

Fig. 33

Sampler tube temperature vs. number density and altitude.

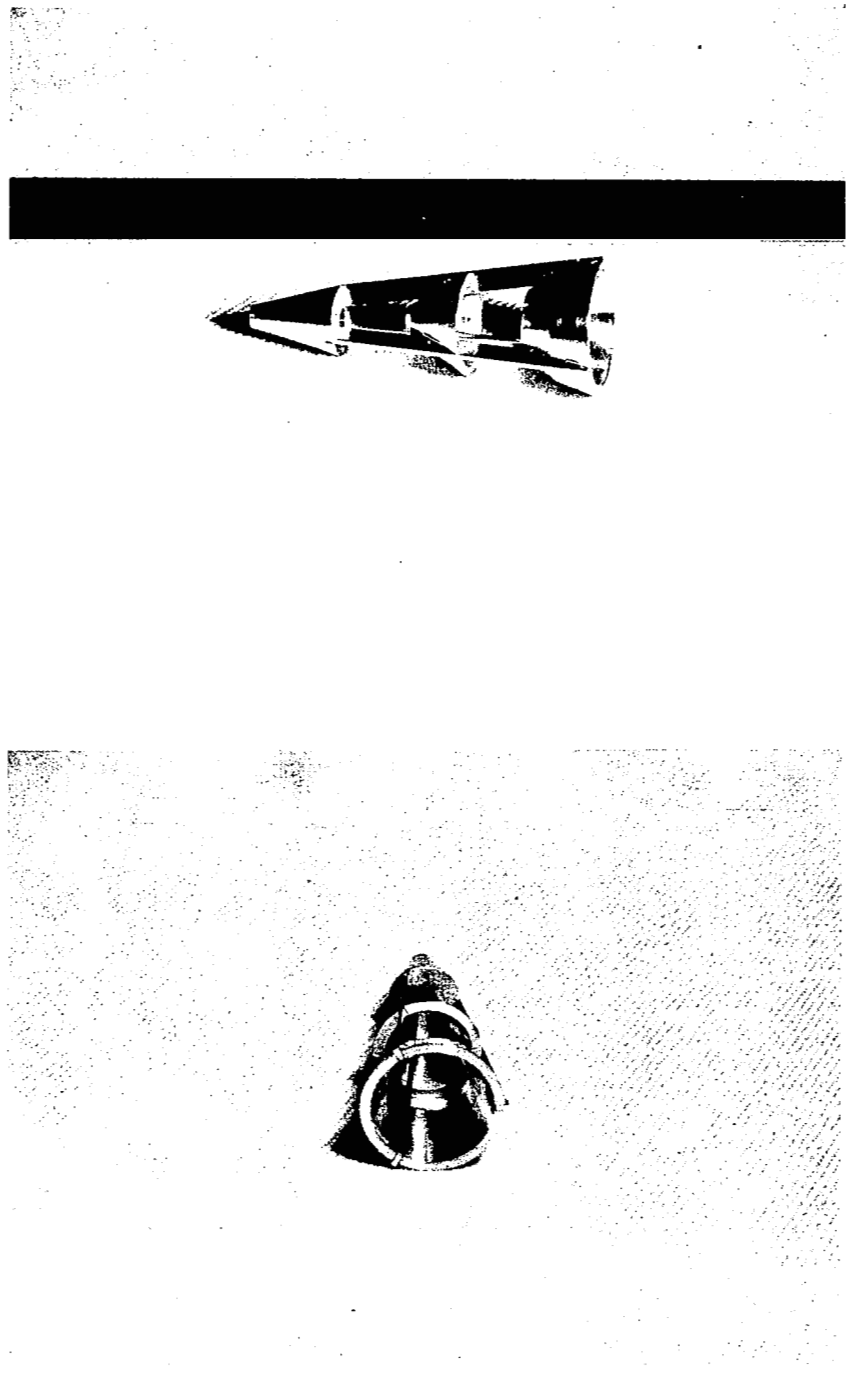

Fig. 34.- Photographs of completed gas sampler.

CONCLUSIONS

Based on the analytical model chosen to describe the gas-gas and gas-surface interactions, the theoretical treatment has been completed for the performance evaluation of a molecular beam gas sampling system of a high speed atmospheric entry probe. By establishing the free molecular flow properties through the sampler and the angular distributions of the unscattered and scattered exit flux, the limits of operation were defined in terms of the signal-to-noise ratio, gas-gas scattering attenuation coefficient, sampler temperature and internal tube mean free path. Data were presented for the functional dependence of these parameters with atmospheric density, entry velocity, and inlet tube geometry.

The computer program developed for this analysis is adaptable to different atmospheres and entry conditions as was shown by using it to define the geometries of gas samplers for both a Martian and an Earth experiment. Having established the desireable geometry; the design, material requirements, and fabrication techniques were established for a multiple tube gas sampling system for an analysis of the Martian atmosphere down to the highest density practicable. This limit was established by performing a trade-off analysis between the computed performance and the applicable material requirements and fabrication techniques. The utility of these techniques was demonstrated by fabricating a gas sampling system for the Earth experiment. The design was chosen so that the limiting parameter

would be gas-gas scattering attenuation of the signal rather than geometrical instability due to gas enthalpy heating. This approach permits the experimental evaluation of the gas sampling technique while providing useful scientific measurements and flight evaluation of the system. The operating parameters were chosen so that the sampler would operate down to approximately 90 km in the Earth atmosphere.

RECOMMENDATIONS

1. Since the theoretical analysis allows for the performance evaluation only at zero angle-of-attack, which for most atmospheric probes is a limitation, it is recommended that one of the extensions of the theoretical treatment be to include an evaluation at non-zero angle of attack. At the same time, it would be appropriate to investigate the feasibility of including other reflection models than the diffuse reflection model used presently. The choice of a single theoretical model which correctly describes the high velocity gas-surface interactions consistent with experimental data is not apparent at the present time.

2. It is recommended that the tube bundle fabrication techniques, which were described and considered most realistic, be established since this type a sampler inlet is necessary if high density analyses are to be performed. Special emphasis should be placed on producing the minimum cross sectional area while retaining and acceptable value for the geometrical transparency. The maximum iridium content consistent with this fabrication scheme should also be established.

3. It is considered that the experimental varification of the sampler performance can be more accurately controlled and evaluated under laboratory conditions than in actual flight although both phases of testing are necessary for complete evaluation. It is therefore recommended that 1) the feasibility of using a "hot" molecular beam for the evaluation of

the multiple tube gas sampler performance be considered and 2) additional analysis be carried out on the in-flight, Earth atmosphere evaluation of the performance using a sampler such as the single tube design which was fabricated under this contract.

REFERENCES

1. Douglass, R. W.; Krier, C. A.; and Jaffee, R. I.: High Temperature Properties and Alloying Behavior of the Refractory Platinum-Group Metals. Battelle Memorial Institute Summary Report (AD265624), Aug. 31, 1961.

2. Koster, W.: Die Temperaturabhängigkeit des Elastizitäts-moduls reiner Metalle, Z. Metallkunde, vol. 39, pp. 1-9, 1948.

3. Metals Handbook, 8th Edition, American Society for Metals, Novelty, Ohio, pp. 1189-1196, 1961.

4. Vines, R. F. and Wise, E. M.: The Platinum Metals and Their Alloys. The International Nickel Company, Inc. New York, New York, 1941.

5. Short-Time High-Temperature Testing, Proceedings of the Symposium "Short-Time Elevated-Temperature Testing of Metals" 10th Metal Congress and Exposition, Los Angeles, 1957, Published by ASM, Cleveland, Ohio, 1958.

6. Atkinson, R. H. and Furman, D. E.: Creep Characteristics of Some Platinum Metals at 1382°F. Trans. AIME, vol. 191, pp. 806-808, 1951.

7. Albert, H. A., Accinno, D. J. and Hill, J. S.: Stress-Rupture Properties of Some Platinum and Palladium Alloys, Part II, AIME Metallurgical Soc. Conferences, vol. 11, pp. 476-482, 1961.

8. Ad'yasevich, B. P. and Antonenko, V. G.: Preparation of Glass Collimators, Translated from Pribory i Tekhnika Eksperimenta, No. 2, pp. 126-128, March-April, 1963 (In Russian) Instrum. and Exper. Tech. (USA) No. 2, pp. 308-310, March-April, 1963.

9. Vapor Deposition, Edited by Powell, C. F.; Oxley, J. H. and Blocker, J. M., Sponsored by The Electrochemical Society, Inc., John Wiley & Sons, Inc. New York, 1966.

10. MacNamara, E. L.: The Electrodeposition of Iridium, Jour. Electrochem, Soc., vol. 109, No. 1, p. 61, Jan. 1962.

11. Tyrrell, C. J.: The Electrodeposition of Iridium, Trans. Inst. of Metal Finishing, vol. 43, p. 161, 1965.

12. Withers, J. C. and Ritt, P. E.: Iridium Plating and Its High Temperature Oxidation Resistance, Tech. Proc. Am. Electroplaters' Soc., vol. 44, p. 124, 1957.

13. Tyrrell, C. J.: The Electrodeposition of Platinum-Iridium Alloys, Trans. Inst. Metal Finishing, vol. 45, p. 53, 1967.

APPENDIX A

Calculation Of The Numerical Constant In Eq. (2.2)

In order to evaluate the constant is Eq. 2.2, $\nu_p(X) = - \frac{C}{\pi r^2} \frac{d}{dX} F_P(S,X)$, we get:

$$\nu_p(X) = - C \frac{d}{dX} \int_0^{\tan^{-1}X^{-1}} \psi_1(S,\phi)\ \psi_2(X,\phi)\ \psi_3(X,\phi)\ d\phi$$

$$\nu_p(X) = - C \int_0^{\tan^{-1}X^{-1}} \frac{d}{dX} \left\{\psi_2(X,\phi)\ \psi_3(X,\phi)\right\} \cdot \psi_1(S,\phi) d\phi$$

$$\nu_p(X) = - C \int_0^{\tan^{-1}X^{-1}} \psi_1(S,\phi) \left[\psi_2(X,\phi) \cdot \frac{d}{dX}\ \psi_3(X,\phi) + \psi_3(X,\phi) \frac{d}{dX}\ \psi_2(X,\phi)\right] d\phi$$

$$\nu_p(X) = - C\left\{\int_0^{\tan^{-1}X^{-1}} \psi_1(S,\phi)\ \psi_2(X,\phi)\ \psi_3(X,\phi)\left[-2\pi\sigma(1+\tan^2\phi)^{1/2}n(X)\right]d\phi\right.$$

$$\left. + \int_0^{\tan^{-1}X^{-1}} \psi_1(S,\phi)\ \psi_3(X,\phi)\left[-\frac{4}{\pi}\tan\phi(1-X^2\tan^2\phi)^{1/2}\right]d\phi\right\} .$$

This last equation, when inserting the boundary conditions that $\nu_p(o) = \frac{n_o\bar{v}}{4}$ and $n(o) = 0$, yields:

$$\frac{n_o\bar{v}}{4} = + C\,\frac{n_o v_m 4}{\pi^{3/2}}\int_0^{\pi/2} \sin^2\phi\left\{(1+S^2\cos^2\phi)\,e^{-S^2} + \sqrt{\pi}S\,\cos\phi\left[\frac{3}{2} + S^2\cos^2\phi\right]\right.$$

$$\left.\left[1+\mathrm{erf}(S\cos\phi)\right]e^{-S^2\sin^2\phi}\right\}d\phi .$$

Now letting

$$\bar{v} = \frac{2}{\sqrt{\pi}}\,v_m \qquad \text{and}$$

$$\psi_4(S,\phi) = \sin^2\phi\left\{\psi_1(S,\phi)\right\}$$

we get:

$$\frac{1}{4} = C \frac{2}{\pi} \int_0^{\pi/2} \psi_4(S,\phi)d\phi \ .$$

The integral $\int_0^{\pi/2} \psi_4(S,\phi)d\phi$ was evaluated numerically and was shown to be $\pi/2$. Therefore:

$$C = 1/4 \ .$$

APPENDIX B

Derivation Of The Scattered Gas Collision Frequency

Consider the following diagrams

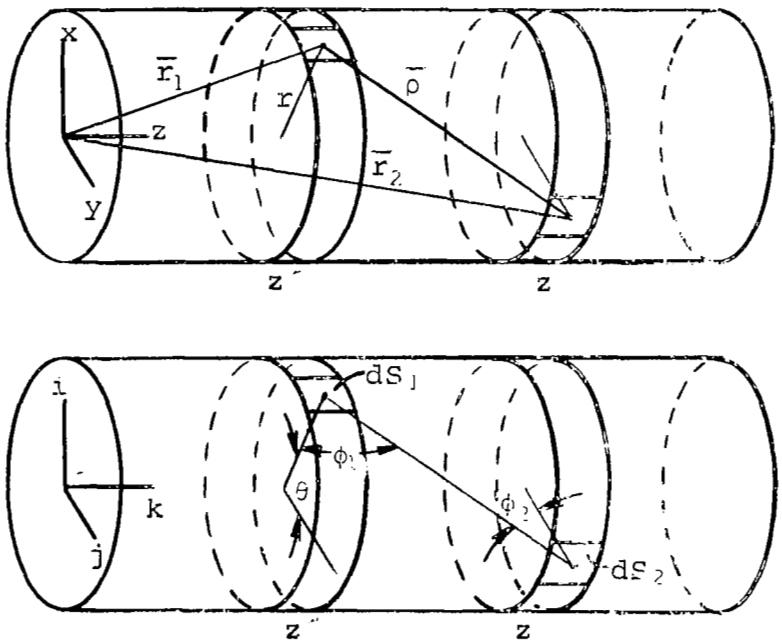

$$\bar{r}_1 = (r \sin\theta)\,\bar{I} + (r \cos\theta)\,\bar{j} + (z')\bar{k}$$

$$\bar{r}_2 = (r)\bar{j} + (z)\bar{k}$$

$$\bar{r}_2 - \bar{r}_1 = \bar{\rho} = (-r \sin\theta)\,\bar{i} + \left[r(1-\cos\theta)\right]\bar{j} + (z-z')\bar{k}$$

$$\bar{n}_1 = -\cos\theta\,\bar{j} - \sin\theta\,\bar{i}$$

$$\bar{n}_2 = -\bar{j}$$

$$\left|\bar{r}_2 - \bar{r}_1\right|^2 = \rho^2 = r^2\sin^2\theta + r^2\left[1 - 2\cos\theta + \cos^2\theta\right] + |z - z'|^2$$

$$\rho^2 = 2r^2(1-\cos\theta) + |z - z'|^2$$

$$\cos\phi_1 = \frac{\bar{n}_1 \cdot \bar{\rho}}{|\bar{n}_1||\bar{\rho}|} = \frac{r\sin^2\theta - r\cos\theta(1-\cos\theta)}{\left[2r^2(1-\cos\theta) + |z - z'|^2\right]^{1/2}}$$

$$\cos\phi_1 = \frac{r\,(1 - \cos\theta)}{\left[2r^2(1-\cos\theta) + |z - z'|^2\right]^{1/2}}$$

$$\cos\phi_2 = \frac{\bar{n}_2 \cdot -\bar{\rho}}{|\bar{n}_2||\rho|} = \frac{r\,(1 - \cos\theta)}{\left[2r^2(1 - \cos\theta) + |z - z'|^2\right]^{1/2}}$$

The number of molecules per unit area per unit time leaving dS_1 in any given direction are

$$\hat{\mu}(dS_1)\,\cos\phi_1\,d\omega$$

where $\hat{\mu}(dS_1)$ is the number of molecules per unit area per unit time per unit solid angle leaving dS_1. Using an arguement of particle conservation, this quantity, when integrated over all ω, will equal the number of particles per unit area per unit time arriving at dS_1. Therefore, we have:

$$\int_{\omega} \hat{\mu}(dS_1)\ \cos\phi_1\ d\omega = \nu(dS_1)$$

where $\nu(dS_1)$ is the number of particles per unit area per unit time colliding with dS_1.

$$\int_{0}^{\pi/2} \hat{\mu}(dS_1)\ \cos\phi_1\ (2\pi\sin\phi_1 d\phi_1) = \nu(dS_1)$$

$$\pi\hat{\mu}(dS_1) = \nu(dS_1)$$

The number of molecules per unit area per unit time arriving at dS_2 from dS_1 are:

$$\hat{\mu}(dS_1)\ \cos\phi_2\ \frac{dS_1\cos\phi_1}{\rho^2}$$

and since this represents only an incremental fraction of the total number of collisions from the whole tube surface we get:

$$\hat{\mu}(dS_1)\ \cos\phi_2\ \frac{dS_1\cos\phi_1}{\rho^2} = d\nu_s(dS_2) \quad \text{or}$$

$$\frac{\nu(dS_1)}{\pi}\ \cos\phi_2\ \frac{dS_1\cos\phi_1}{\rho^2} = d\nu_s(dS_2)$$

Now considering an element of area at z which is dz wide and a similar element at z´ and arguing that the scattered gas collision frequency at the elements is constant at any dS within the element we can say that:

$$\frac{\nu(z')}{\pi}\ \cos\phi_2\ \frac{dS_1\cos\phi_1}{\rho^2} = d\nu_s(z)$$

or since

$$dS_1 = r\,d\theta\,dz'$$

$$d\nu_s(z) = \frac{\nu(z')\ dz'}{\pi}\ r\ \frac{\cos\phi_1\ \cos\phi_2\ d\theta}{\rho^2}$$

$$d\nu_s(z) = \frac{\nu(z')dz'}{\pi} r \frac{r^2(1-\cos\theta)^2 d\theta}{\left[2r^2(1-\cos\theta) + |z-z'|^2\right]^2}$$

$$d\nu_s(z) = \frac{\nu(z')\,dz'}{4\pi r} \frac{(1-\cos\theta)^2\,d\theta}{\left[1-\cos\theta + 2\left(\frac{|z-z'|}{2r}\right)^2\right]^2}$$

Now letting $X = \frac{z}{2r}$ and $X' = \frac{z'}{2r}$ we get:

$$d\nu_s(X) = \frac{\nu(X')\,dX'}{2\pi} \frac{(1-\cos\theta)^2 d\theta}{\left[1-\cos\theta + 2|X-X'|^2\right]^2}$$

$$\nu_s(X) = \frac{1}{2\pi} \int_{X'=0}^{X_M} \int_{\theta=0}^{2\pi} \frac{\nu(X')(1-\cos\theta)^2}{\left[1+2|X-X'|^2-\cos\theta\right]^2} d\theta dX'$$

$$\nu_s(X) = \int_0^{X_M} \nu(X') \left\{1 - \frac{|X-X'|\left(|X-X'|^2 + 3/2\right)}{\left(|X-X'|^2 + 1\right)^{3/2}}\right\} dX'$$

$$\nu_s(X) = \int_0^{X_M} \nu(X')\ \psi_5(X,X')dX' \quad .$$

APPENDIX C

Properties Of The Platinum Family Metals

Additional mechanical properties of the platinum family metals influencing the choice of materials to be used in the fabrication of the gas sampling system are contained in this appendix.

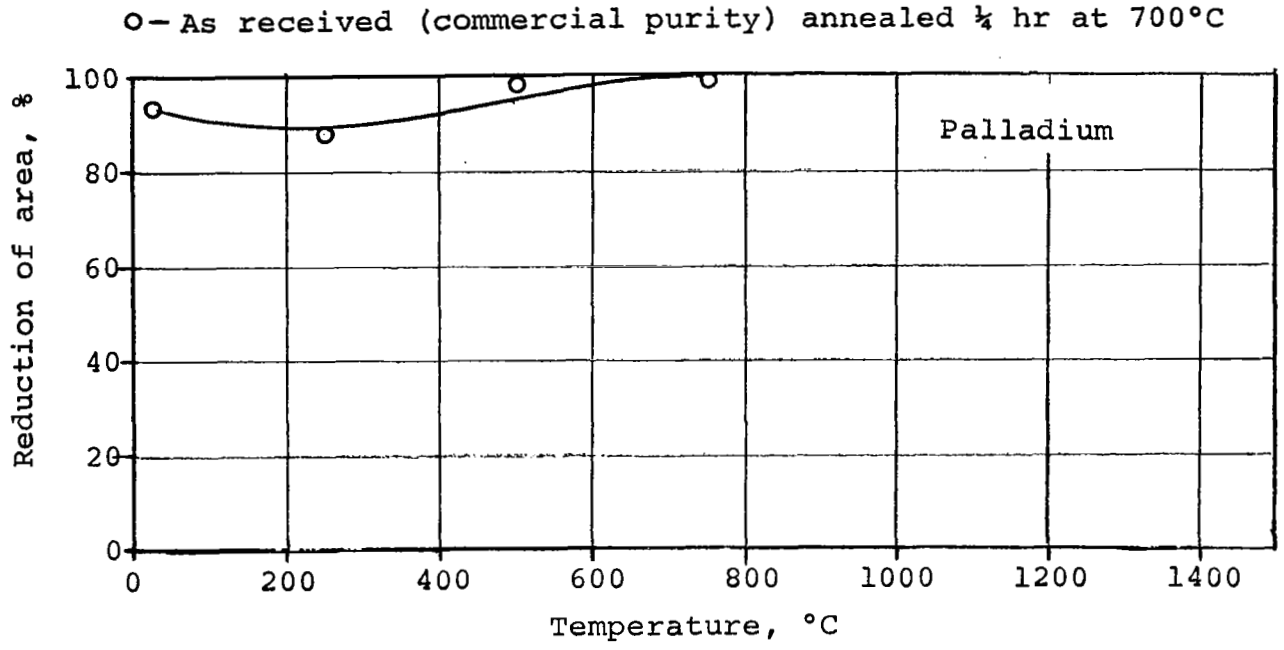

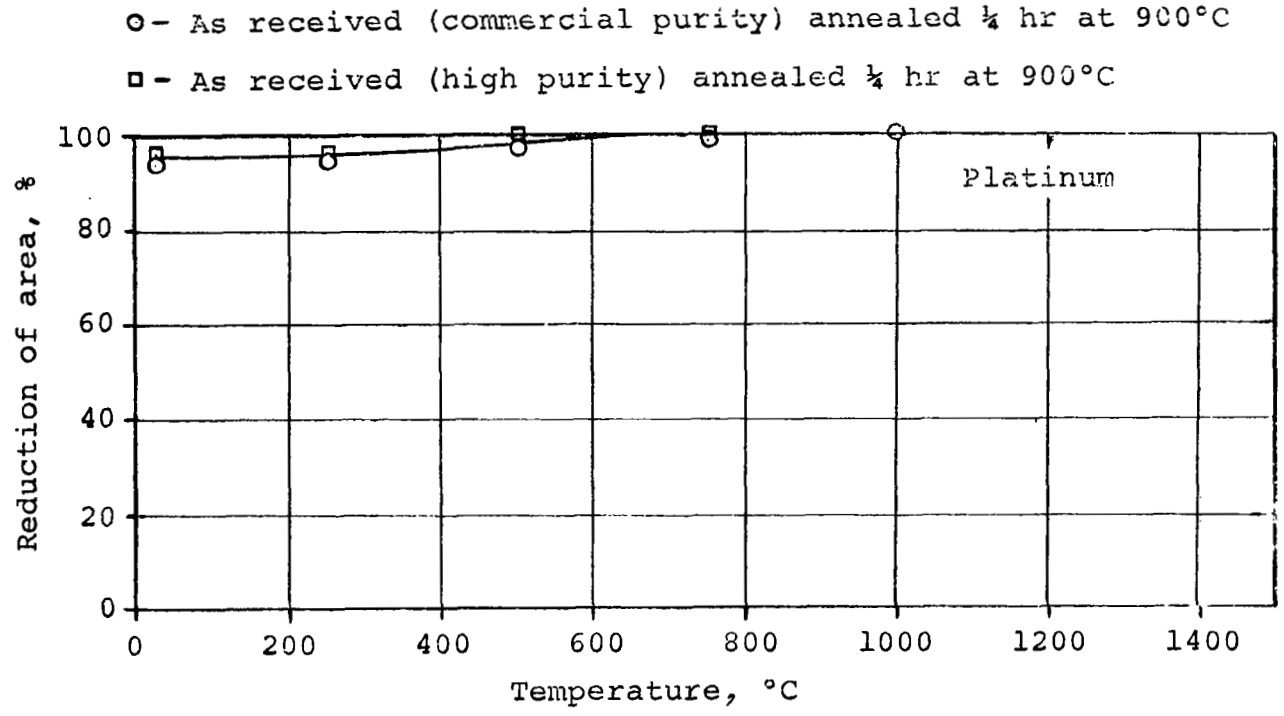

Fig. 1C.- Variation of the reduction of area with temperature. (ref. 1)

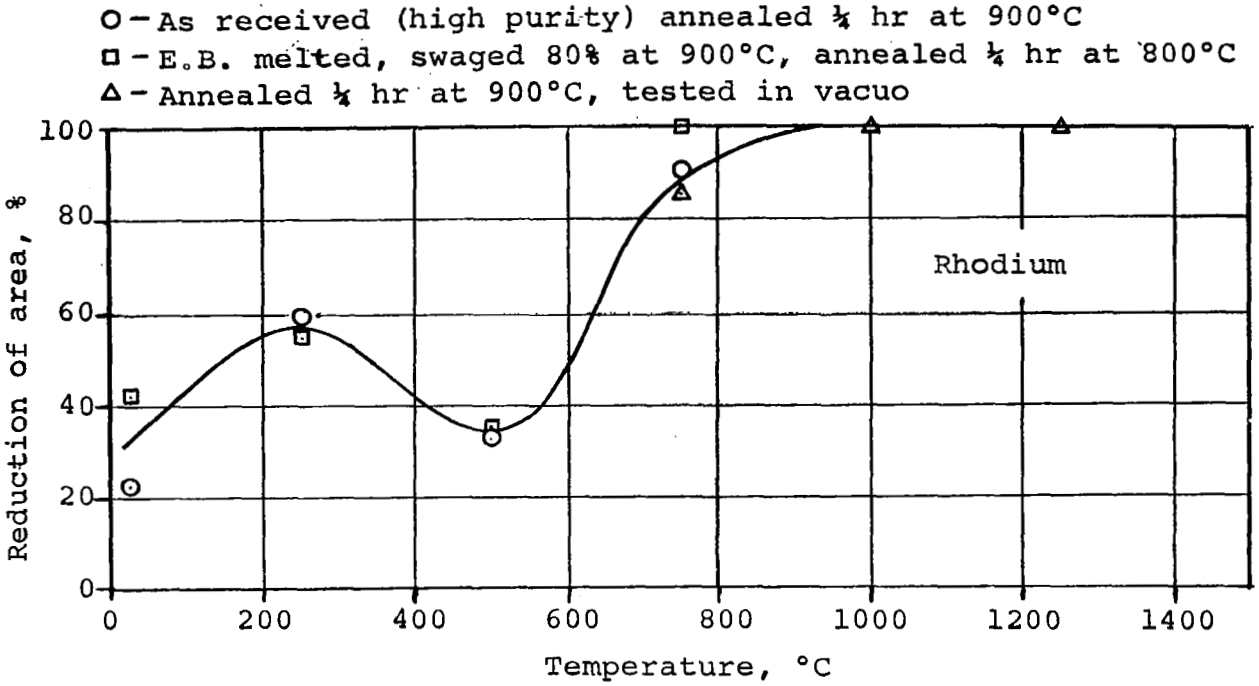

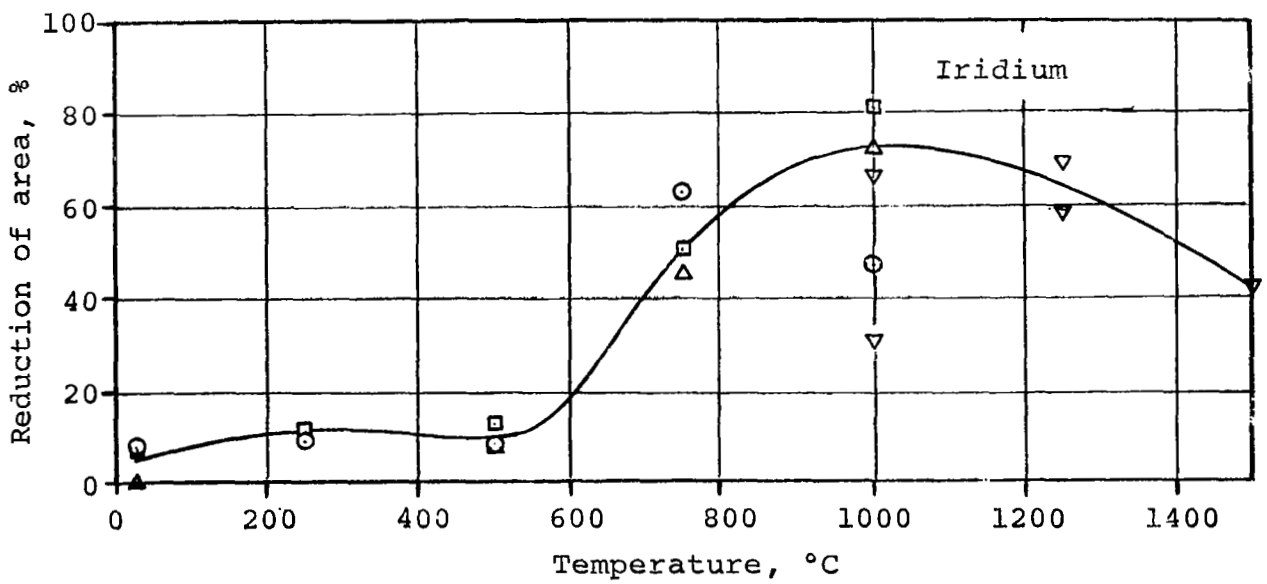

Fig. 2C.- Variation of the reduction of area with temperature. (ref. 1)

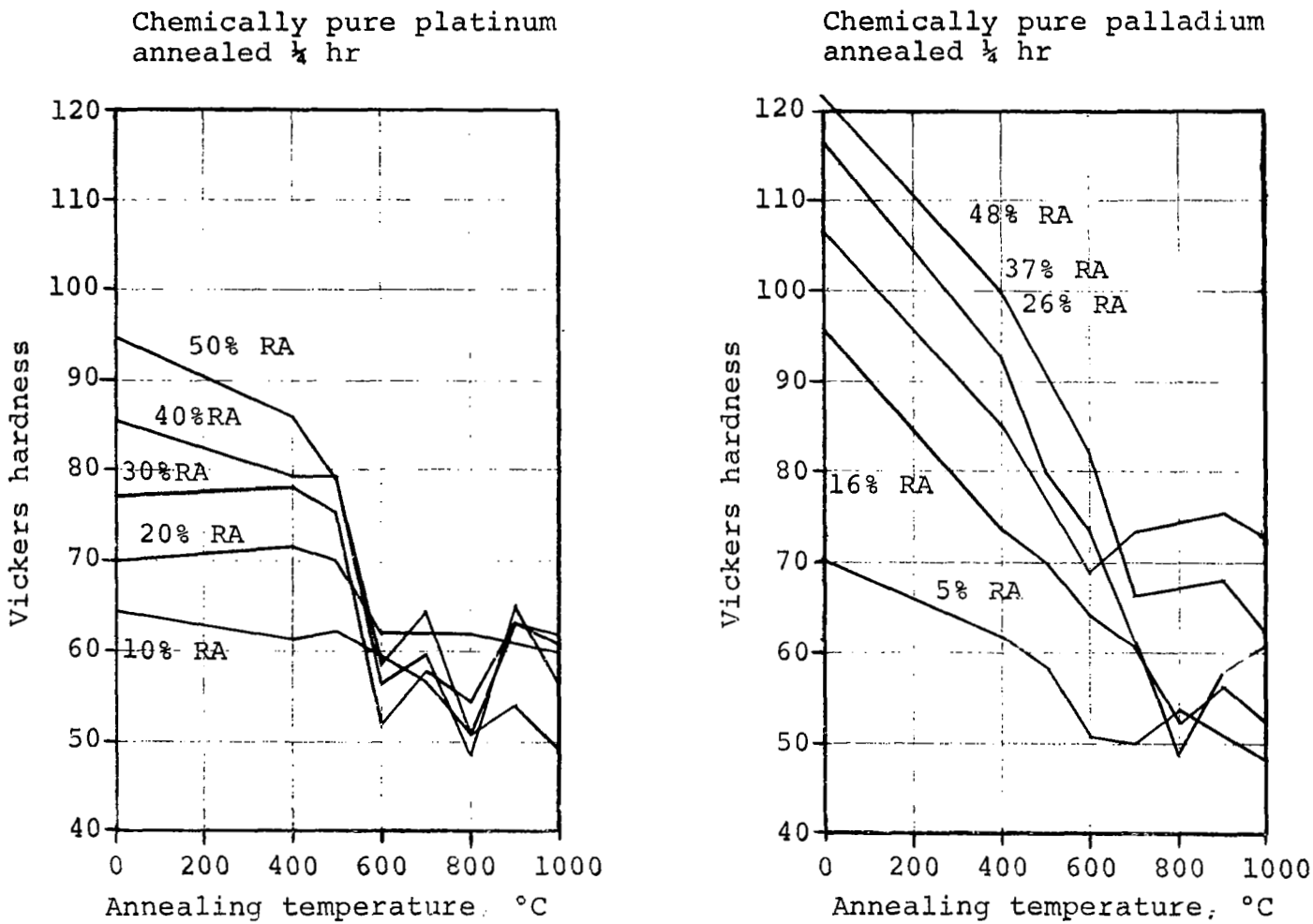

Fig. 3C.- Effect of annealing temperature on the hardness of cold-rolled platinum and palladium. (ref. 1)

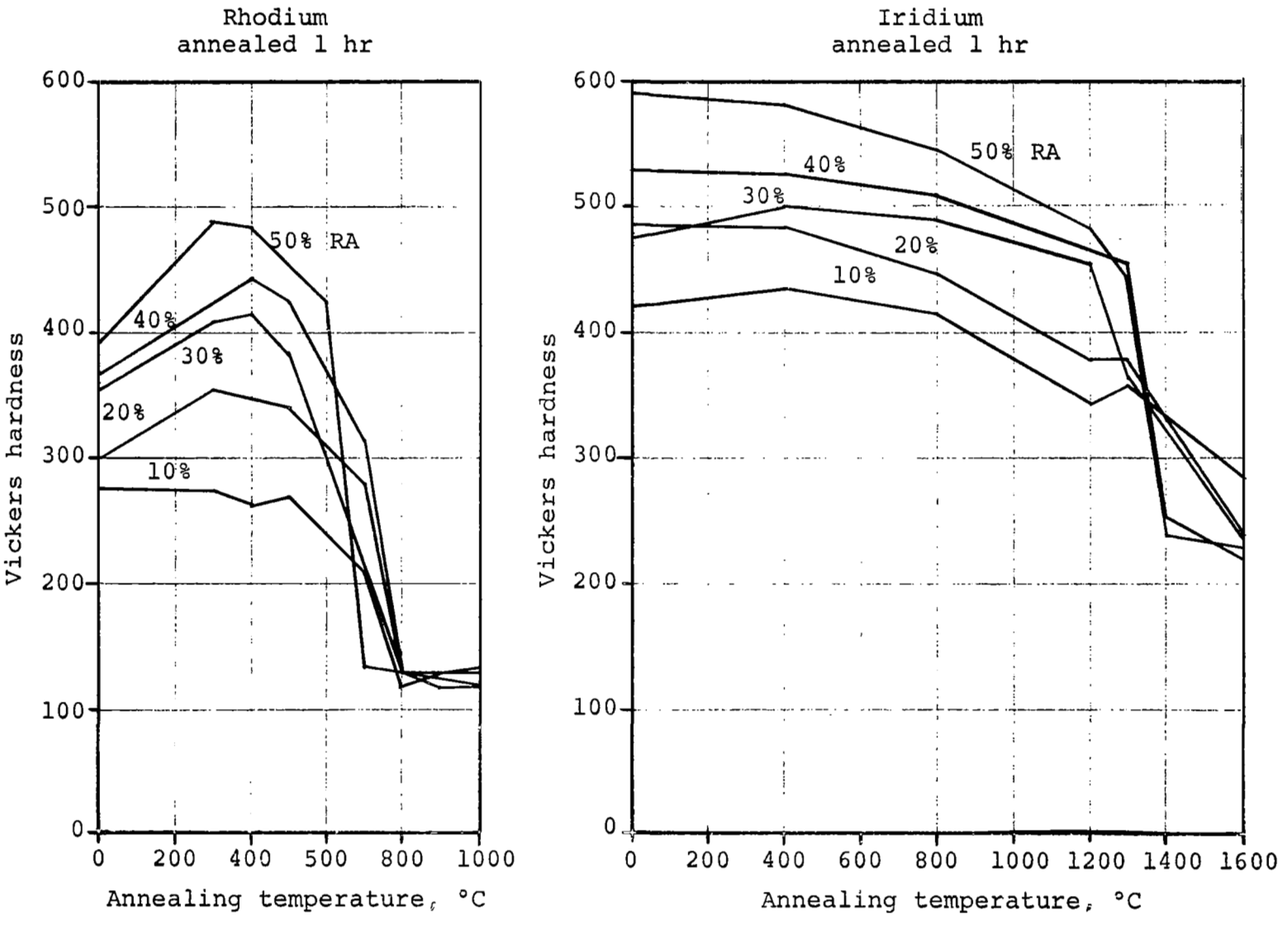

Fig. 4C.- Effect of annealing temperature on the hardness of cold-rolled rhodium and iridium. (ref. 1)

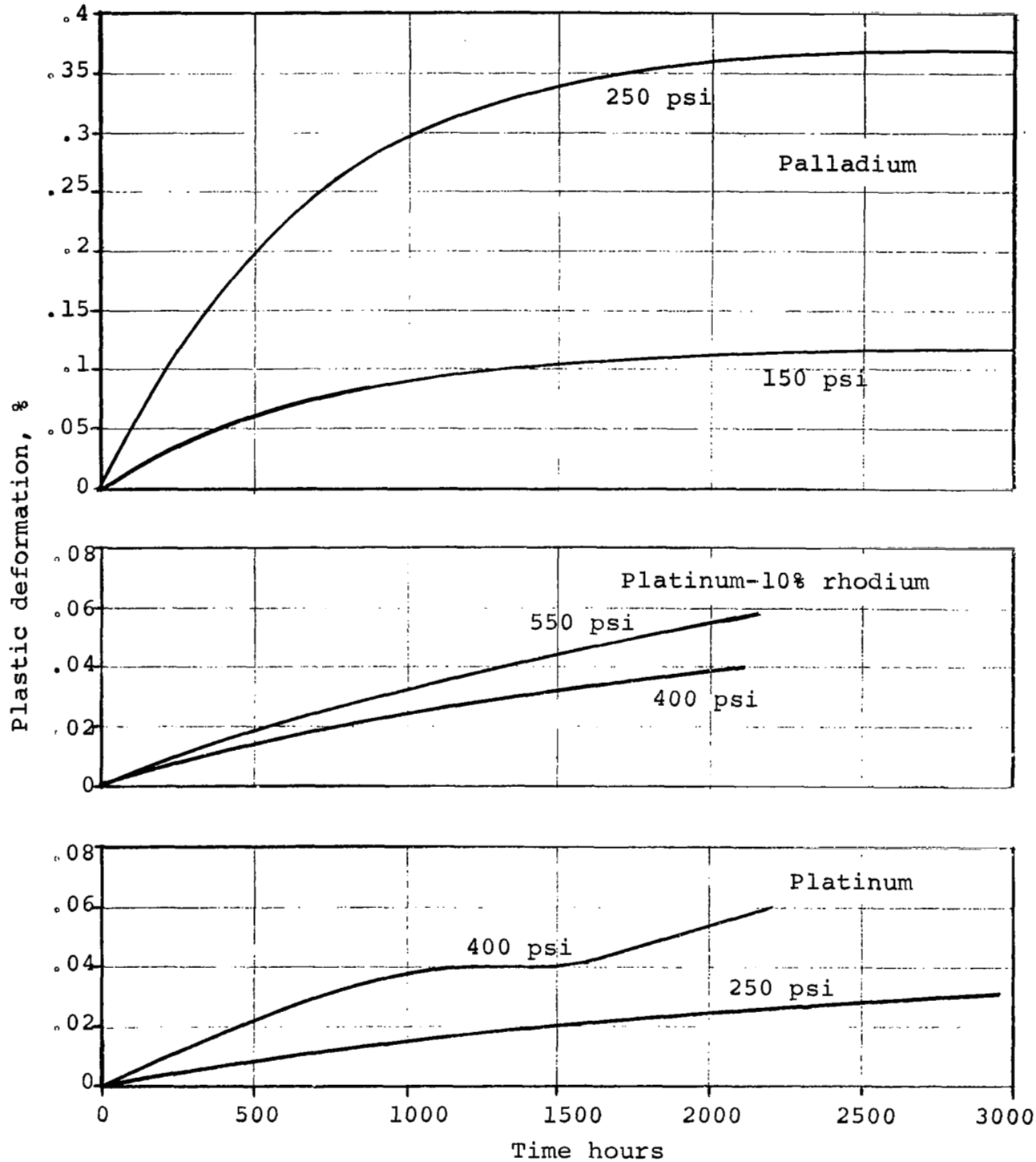

Fig. 5C.- Creep rates for platinum, platinum-10% rhodium and palladium at 1382°F (750°C). (ref. 6)

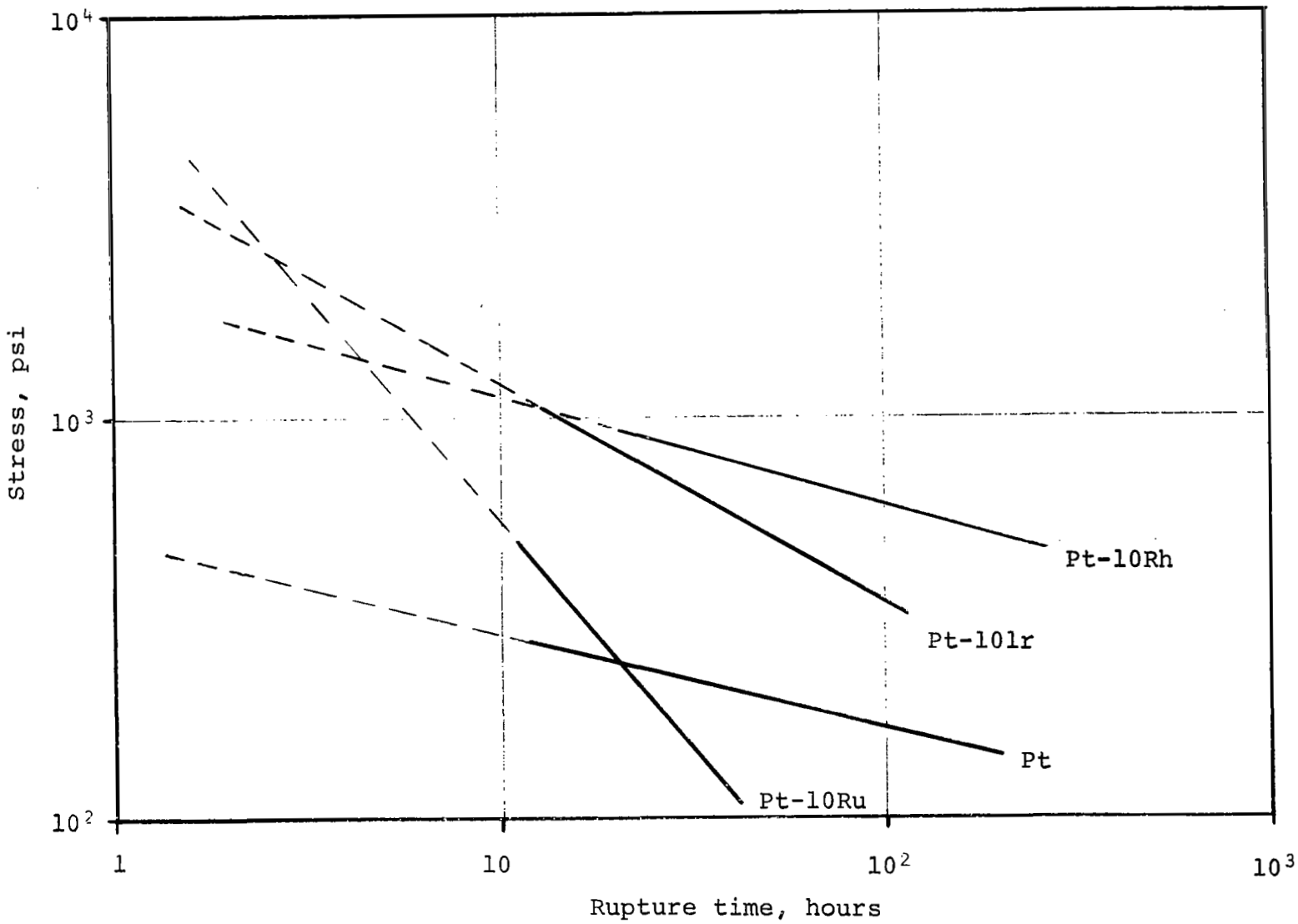

Fig. 6C.- Stress-rupture strength of platinum alloy wires at 1450°C (ref. 7)

APPENDIX D

List of Symbols

A	Inlet area of the tube, cm^2
A_1	Annular cross-sectional area of the tube, cm^2
$d\omega$	Elemental solid angle increment, sr
$F_p(S,O)$	Primary flux entering the tube, sec^{-1}
$F_p(S,X)$	Primary flux transmitted up to X, sec^{-1}
F_s	Scattered gas flux, sec^{-1}
L	Tube length, cm
m	Particle mass, gm
n_o	Undisturbed gas density, cm^{-3}
$n(X)$	Diffuse gas density distribution inside the tube, cm^{-3}
P_i	Total power dissipated at the tube surfaces, $erg\text{-}sec^{-1}$
P_r	Total power radiated by the tube, $erg\text{-}sec^{-1}$
R	Radial distance from tube exit to the point of observation, cm
r	Tube radius, cm
$S \equiv U/v_m$	Speed ratio
$S_1 \equiv U/\bar{v}$	Vehicle speed/average thermal molecular speed
$(S/N)_F$	Signal-to-noise ratio based on flux

$(S/N)_n$	Signal-to-noise ratio based on density
$T(S,X)$	Total transmission function
$T_g(S,X)$	Geometrical transmission function
T_T	Tube temperature, °K
X	Dimensionless length
X_E	Value of X at the point of observation
X_M	Length-to-diameter ratio
X_m	That value of X for which the scattered flux is just transmitted at an angle θ
U	Vehicle speed, $cm\text{-}sec^{-1}$
$\bar{v}$	Average thermal molecular speed, $cm\text{-}sec^{-1}$
v_m	Most probable thermal molecular speed, $cm\text{-}sec^{-}$
α_1	Energy accomodation coefficient for normal incidence
α_2	Energy accomodation coefficient for grazing incidence
$\gamma \equiv$ GGSA	Gas-gas scattering attenuation coefficient
ε	Effective emittance of the cylindrical cavity $erg\text{-}cm^{-2}\text{-}sec^{-1}\text{-}°K^{-4}$
ε_1	Total normal emittance of the solid
θ	Angle between scattered particle velocity vector and the tube axis, radians
θ_M	Maximum value of θ, radians

λ		Mean free path inside the tube, cm
$\hat{\mathfrak{J}}(dS)$		Molecular radiation intensity, sec^{-1}-cm^{-2}-sr^{-1}
$\nu(X)$		Total collision frequency density, sec^{-1}-cm^{-2}
$\nu_p(X)$		Primary gas collision frequency density, sec^{-1}-cm^{-2}
$\nu_s(X)$		Scattered gas collision frequency density, sec^{-1}-cm^{-2}
σ		Diffuse gas collision cross section, cm^2
σ_s		Stefan-Boltzmann constant, erg-cm^{-2}-sec^{-1}-$^oK^{-4}$
ϕ		Angle between particle velocity vector and the tube axis, radians
$\psi_1(S,\phi)$		Flux incident at an angle ϕ on the tube entrance, sec^{-1}
$\psi_2(X,\phi)$		Fraction of the incident flux which is transmitted a distance X in the direction ϕ
$\psi_3(x,\phi)$		Gas-gas scattering attenuation coefficient
$\psi_4(S,\phi)$	$\equiv$	$\sin^2\phi\,\lvert\psi_1(S,\phi)\rvert$, sec^{-1}
$\psi_5(X,X')$	$\equiv$	$\left\lvert 1 - \frac{\lvert X-X'\rvert\,(\lvert X-X'\rvert^2 + 3/2)}{(\lvert X-X'\rvert^2 + 1)^{3/2}}\right\rvert$